[36] S. Zhang, W.C. Huang, P. Li, H. Guo, S.B. Poh, S.W. Brady, Y. Xiong, L.M. Tseng, S.H. Li, Z. Ding, A.A. Sahin, F.J. Esteva, G.N. Hortobagyi, D. Yu, Combating trastuzumab resistance by targeting SRC, a common node downstream of multiple resistance pathways, Nat. Med. 17 (2011) 461–469.
[37] J.O. Moore, M.A. Lemmon, K.M. Ferguson, Tie2 receptor dimerization mediated by its extracellular FNIII domains, Biophysical Journal, 2013, p. 608a.
[38] M.A. Schumacher, N. Chinnam, T. Ohashi, R.S. Shah, H. Erickson, Structure of irisin reveals a novel intersubunit beta-sheet fibronectin (FNIII) dimer; implications for receptor activation, J. Biol. Chem. 288 (2013) 33738–33744.
[39] L. Zabeau, D. Defeau, H. Iserentant, J. Vandekerckhove, F. Peelman, J. Tavernier, Leptin receptor activation depends on critical cysteine residues in its fibronectin type III subdomains, J. Biol. Chem. 280 (2005) 22632–22640.
[40] G.M. Keating, Pertuzumab: in the first-line treatment of HER2-positive metastatic breast cancer, Drugs 72 (2012) 353–360.
[41] S.M. Swain, S.B. Kim, J. Cortes, J. Ro, V. Semiglazov, M. Campone, E. Ciruelos, J.M. Ferrero, A. Schneeweiss, A. Knott, E. Clark, G. Ross, M.C. Benyunes, J. Baselga, Pertuzumab, trastuzumab, and docetaxel for HER2-positive metastatic breast cancer (CLEOPATRA study): overall survival results from a randomised, double-blind, placebo-controlled, phase 3 study, Lancet Oncol. 14 (2013) 461–471.
[42] A. Freywald, N. Sharfe, C.M. Roifman, The kinase-null EphB6 receptor undergoes transphosphorylation in a complex with EphB1, J. Biol. Chem. 277 (2002) 3823–3828.
[43] K. Nagano, S. Kanasaki, T. Yamashita, Y. Maeda, M. Inoue, K. Higashisaka, Y. Yoshioka, Y. Abe, Y. Mukai, H. Kamada, Y. Tsutsumi, S. Tsunoda, Expression of Eph receptor A10 is correlated with lymph node metastasis and stage progression in breast cancer patients, Cancer Med. 2 (2013) 972–977.

Neuroscience Letters 534 (2013) 85–89

Contents lists available at SciVerse ScienceDirect

Neuroscience Letters

journal homepage: www.elsevier.com/locate/neulet

Proteomic analysis of the hippocampus in Alzheimer's disease model mice by using two-dimensional fluorescence difference in gel electrophoresis

Masaoki Takano[a], Takuya Yamashita[b,c], Kazuya Nagano[c], Mieko Otani[a], Kouji Maekura[a], Haruhiko Kamada[c], Shin-ichi Tsunoda[c], Yasuo Tsutsumi[b,c], Takami Tomiyama[e,f], Hiroshi Mori[e,f], Kenji Matsuura[d], Shogo Matsuyama[d,*]

[a] Laboratory of Molecular Cellular Biology, School of Pharmaceutical Sciences, Kobe Gakuin University, 1-1-3 Minatojima, Chuo-ku, Kobe 650-8586, Japan
[b] Laboratory of Toxicology and Safety Science, Graduate School of Pharmaceutical Sciences, Osaka University, 1-6 Yamadaoka, Suita, Osaka 565-0871, Japan
[c] Laboratory of Biopharmaceutical Research, National Institute of Biomedical Innovation, 7-6-8 Saito-Asagi, Ibaraki, Osaka 567-0085, Japan
[d] Faculty of Pharmaceutical Sciences, Himeji Dokkyo University, 7-2-1 Kamiohno, Himeji 670-8524, Japan
[e] Department of Neuroscience, Osaka City University Graduate School of Medicine, Osaka 545-8585, Japan
[f] Core Research for Evolutional Science and Technology, Japan Science and Technology Agency, Japan

HIGHLIGHTS

- We perform the proteome for $APP_{E693\Delta}$-transgenic mice. Methods are two-dimensional fluorescence difference in gel electrophoresis and mass spectrometry techniques. The expression of 14 proteins are changed in the brain. Aβ oligomers contribute to the expression of proteins.

ARTICLE INFO

Article history:
Received 4 August 2012
Received in revised form 13 October 2012
Accepted 6 November 2012

Keywords:
Proteome
Amyloid β oligomers
Alzheimer's disease
Hippocampus
2D-DIGE

ABSTRACT

We previously identified the E693Δ mutation in amyloid precursor protein (APP) in patients with Alzheimer's disease (AD) and then generated APP-transgenic mice expressing this mutation. As these mice possessed abundant Aβ oligomers from 8 months of age but no amyloid plaques even at 24 months of age, they are a good model to study pathological effects of amyloid β (Aβ) oligomers. The two-dimensional fluorescence difference in gel electrophoresis (2D-DIGE) technology, using a mixed-sample internal standard, is now recognized as an accurate method to determine and quantify proteins. In this study, we examined the proteins for which levels were altered in the hippocampus of 12-month-old $APP_{E693\Delta}$-transgenic mice using 2D-DIGE and liquid chromatography–tandem mass spectrometry (LC–MS/MS). Fourteen proteins were significantly changed in the hippocampus of $APP_{E693\Delta}$-transgenic mice. Actin cytoplasmic 1 (β-actin), heat shock cognate 71 kDa, γ-enolase, ATP synthase subunit β, tubulin β-2A chain, clathrin light chain B (clathrin) and dynamin-1 were increased. Heat shock-related 70 kDa protein 2, neurofilament light polypeptide (NFL), stress-induced-phosphoprotein 2, 60 kDa heat shock protein (HSP60), α-internexin, protein kinase C and casein kinase substrate in neurons protein 1 (Pacsin 1), α-enolase and β-actin were decreased. Western blotting also validated the changed levels of HSP60, NFL, clathrin and Pacsin 1 in $APP_{E693\Delta}$-transgenic mice. The identified proteins could be classified as cytoskeleton, chaperons, neurotransmission, energy supply and signal transduction. Thus, proteomics by 2D-DIGE and LC–MS/MS has provided knowledge of the levels of proteins in the early stages of AD brain.

1. Introduction

AD is neuropathologically characterized by abnormal accumulation of extracellular amyloid plaques and intracellular neurofibrillary tangles throughout cortical and limbic regions. Although the current amyloid cascade hypothesis [6] and tau hypothesis [15] provide frameworks for studying AD pathogenesis. Recently, diverse lines of evidence suggest that Aβ peptides play more important roles in AD pathogenesis [13,16,20]. Especially, soluble oligomers of Aβ could be a cause of synaptic and cognitive dysfunction in the early stages of AD. To address the relationship between Aβ oligomers and pathological features of AD, we generated APP transgenic mice expressing the E693Δ mutation, which enhanced Aβ oligomerization without fibrillization [25]. It might provide a clue for elucidating AD pathology caused by Aβ oligomers to analyze the $APP_{E693\Delta}$-transgenic mice.

* Corresponding author. Tel.: +81 79 223 6849; fax: +81 79 223 6857.
E-mail address: shogo@himeji-du.ac.jp (S. Matsuyama).

0304-3940/$ – see front matter © 2012 Elsevier Ireland Ltd. All rights reserved.
http://dx.doi.org/10.1016/j.neulet.2012.11.010

One of the most utilized approaches in proteomics to quantify and identify proteins is two dimensional gel electrophoresis (2DE) and mass spectrometry (MS) [5]. Proteomic approaches were most widely based on methods using differential expression on 2D-PAGE gels, or more recently 2D chromatography, followed by mass spectrometry protein identification. Compared to these conventional analyses, 2D-DIGE has higher reproducibility and sensitivity because of its internal standard design which minimizes gel-to-gel variation, improves spot matching, reduces number of gels needed, and permits quantitative analysis of small sample amounts.

In this study, we studied the altered expression of proteins in the hippocampus of $APP_{E693\Delta}$-transgenic mice using 2D-DIGE and LC–MS/MS approach. This approach revealed that the levels of at least 14 proteins were altered in the hippocampus of 12-month-old $APP_{E693\Delta}$-transgenic mice. These findings suggest that Aβ oligomers might cause synaptic and cognitive dysfunction by affecting the expression of these proteins in the hippocampus.

2. Experimental procedures

2.1. Materials

Sodium dodecyl sulfate, urea, thiourea, CHAPS, dithiothreitol, iodoacetamide, bromophenol blue, and RNase A and DNase I for SDS-PAGE or 2DE were all obtained from Wako Pure Chemical Industries (Osaka, Japan). Source information for all other assay reagents and materials are incorporated into their respective assay methods described below.

2.2. Animal subjects

Transgenic mice expressing human APP_{695} with the APP E693Δ mutation under the mouse prion promoter were used [25]. Heterozygous human $APP_{E693\Delta}$-transgenic mice and age-matched non-transgenic littermates were sacrificed at 12 months of age, and their hippocampi were isolated on an ice-cold plate. Animal care and handling were performed strictly in accordance with the Guidelines for Animal Experimentation at Kobe Gakuin University and Himeji Dokkyo University. Every effort was made to minimize the number of animals used and their suffering.

2.3. Protein labeling with CyDyes

Equal amounts of total protein from 4 hippocampi of $APP_{E693\Delta}$-transgenic mice or age-matched non-transgenic littermates were separately pooled. Protein samples were labeled with CyDyes (GE Healthcare, Piscataway, NJ), as per manufacturer's instructions. In brief, 50 μg of total protein from each sample was mixed in a tube and labeled with Cy2 minimal dye, and 50 μg protein taken from the mix was used as an internal standard on each gel for the three subsequent 2DE and image analysis. In parallel, 50 μg protein from each sample was labeled with either Cy3 or Cy5, and the dyes scrambled within each group to avoid possible dye bias. As a result, one replicate was Cy3 labeled proteins and another replicate was Cy5 labeled proteins. Two replicates (Cy3 and Cy5 labeled samples) were mixed, divided and applied each three independent gels. The sample volumes were adjusted to 18 μL with labeling buffer (7M urea, 2 M thiourea, 4% CHAPS, 30 mM Tris), followed by addition of 1 μL dye (working solution) to each individual sample. The samples were left on ice for 30 min in the dark, followed by adding 1 μL of 10 mmol/L lysine to stop the reaction.

2.4. 2D electrophoresis and image analysis

One sample from each of the CyDye groups was mixed together and adjusted to final concentrations of 1% DTT, 1% IPG buffer at a total volume of 350 μL with lysis buffer (7 M urea, 2 M thiourea, 4% CHAPS) and was used to 24 cm pH 4–7 IPG strips (non-linear; GE Healthcare, Piscataway, NJ) overnight. First dimension isoelectric focusing (IEF) was carried out with IPGphor II (GE Healthcare, Piscataway, NJ). Second dimension SDS-PAGE was performed by mounting the IPG strips onto 20 × 26 cm 12.5% DIGE gels (GE Healthcare, Piscataway, NJ) using Ettan DALT six Large Electrophoresis System (GE Healthcare, Piscataway, NJ) and running the gels at 16 mA/gel for the initial hour and 25 mA/gel at 25 °C constantly until bromophenol blue reached the bottom of the gel. The lysates were labeled at the ratio of 50 μg proteins: 400 pmol Cy3 or Cy5 protein-labeling dye (GE HealthcareBiosciences) in dimethylformamide according to the manufacturer's protocol.

In summary, three analytical gels were completed in total, running 25 μg of pooled reference sample labeled with Cy2, along with two samples (25 μg each), one labeled with Cy3 and the other labeled with Cy5. Gels selected for picking were stained with Deep purple (GE Healthcare, Piscataway, NJ). Approximately 1100 spots were matched across all three analytical gels. The analytical gel was picked using an automated robotic system, Ettan Spot picker (GE Healthcare, Piscataway, NJ). The pick list was created based on the Deep purple image. 2 mm gel plugs were picked, washed, reduced and alkylated, and then digested with trypsin, and the resulting peptides were extracted. Gel trypsinization was performed as previously described [24].

2.5. LC/MS/MS identification

Trypsinized peptides were analyzed by nano LC/MS/MS on a ThermoFisher LTQ Orbitrap XL. In brief, 30 mL of hydrolysate was loaded onto a 5 mm 675 mm ID C12 (Jupiter Proteo, Phenomenex) vented column at a flow-rate of 10 mL/min. Gradient elution was conducted on a 15 cm by 75 mm ID C12 column at 300 nL/min. A 30 min gradient was employed. The mass spectrometer was operated in a data-dependent mode, and the six most abundant ions were selected for MS/MS. Mass spectrometry results were searched using Mascot (www.matrixscience.com). Samples were processed in the Scaffold algorithm using DAT files generated by Mascot. Parameters for LTQ Orbitrap XL data require a minimum of two peptide matches per protein with minimum probabilities of 90% at the protein level.

2.6. Western blotting

Approximately 25 μg of protein from mouse hippocampus was applied to a 12.5% acrylamide gel and SDS-polyacrylamide gel electrophoresis was performed at 17.5 mA/gel for 2 h in second dimension. The gels were transferred onto PVDF membranes (Pall Corporation, Pensacola, FL, USA), in a trans-blot electrophoresis transfer cell (Nihon Eido, Tokyo, Japan). Western blotting was performed by using monoclonal antibodies against β-actin (diluted 1:1000, Cell Signaling, USA) and clathrin (diluted 1:250, Abcam, USA), polyclonal antibodies HSP60, NFL, voltage-dependent anion-selective channel protein 1 (VDAC) (diluted 1:1000, Cell Signaling, USA) and Pacsin 1 (diluted 1:500, Millipore, USA). Peroxidase-conjugated antibody (diluted 1:5000, Abcam, USA) was used as secondary antibody. The reaction was detected by chemiluminescence with ECL reagents (Pierce Biotechnology, USA). A semi quantitative analysis based on optical density was performed by ImageJ software (available at http://www.rsbweb.nih.gov/ij).

3. Results and discussion

The 2D-DIGE gels of the hippocampi from wild type and $APP_{E693\Delta}$-transgenic mice pools were shown as Fig. 1. Two replicates of each pooled sample were run, labeling one replicate with Cy3 (Fig. 1A) and one replicate with Cy5 (Fig. 1B), resulting in three analytical gels. The 2D-DIGE comparative analysis of the wild type and $APP_{E693\Delta}$-transgenic mice revealed significant 74 spots (Fig. 1C). These spots were investigated by LC–MS/MS (Fig. 1D). Finally, fourteen proteins were identified as shown in Table 1. These proteins are classified into several groups that are involved in cytoskeletal, chaperone, energy metabolic, vesicle transport and signaling proteins (Table 2).

Spot nos. 1, 3 and 4 were identified as heat shock-related 70 kDa protein 2, stress-induced-phosphoprotein 1 and HSP60, respectively. The stress-induced-phosphoprotein 1 is the co-chaperone and thought of the function in regulation of interaction with Hsp70 and Hsp90 [10]. HSP60 is the chaperonin which is implicated in mitochondrial protein import and macromolecular assembly and may facilitate the correct folding of imported proteins [9]. The amounts of heat shock-related 70 kDa protein 2, stress-induced-phosphoprotein 1, and HSP60 were significantly decreased. On the contrary, spot no. 9 which was identified as heat shock cognate 71 kDa protein was significantly increased. This protein is also the chaperone and acts as a repressor of transcriptional activation [8]. Thus, Aβ oligomers might contribute to changing the expression of the chaperons.

Spot nos. 8, 10–12 and 16 were identified as actin, and spot nos. 15 and 17 were identified as tubulin β-2A chain. Actin is one of the major cytoskeletal proteins in neurons, and the dynamics of its assembly are involved in many aspects of cell motility, vesicle transport, and membrane turnover [14]. Actin itself is known to link with Aβ, which enhances the neurotoxicity induced by tau-mediated actin filament formation [4]. The four spots of actin but not no. 12 and those of tubulin were significantly increased. Thus, Aβ oligomers might lead to increasing the amounts of actin and tubulin.

Spot nos. 5 and 2 were identified as α-internexin and NFL, respectively, which are known as neuronal intermediate proteins [2,18]. The amounts of α-internexin and NFL were significantly decreased. Thus, the decreased amounts of NFL and internexin might raise neural dysfunction in the hippocampus of AD.

Spot nos. 7 and 13 were identified as α-enolase. Spot nos. 14 and 19 were identified as γ-enolase and ATP synthase subunit β, respectively. Enolase is a multifunctional protein as glycolytic enzyme, belonging to a novel class of surface proteins [11]. ATP synthase is a key role enzyme that provides energy for the cell to use through the synthesis of ATP [1]. The amount of α-enolase was significantly decreased, but the amounts of γ-enolase and ATP synthase subunit β were significantly increased. Interestingly, the levels of α-enolase and ATP synthase subunit α mitochondrial proteins significantly increased in the hippocampus of J20 Tg mice with amyloid deposition [19]. The amyloid deposit enhanced the expression of energy metabolic proteins [22]. Combined with our findings, both Aβ oligomers and amyloid deposition might play an important role in the change of energy metabolic proteins as α-enolase, γ-enolase and ATP synthase subunit β.

Spot no. 20 was identified as dynamin. Dynamin, a well studied neuron-specific mechanochemical GTPase, pinches off synaptic vesicles, freeing them from the membrane and allowing them to re-enter the synaptic vesicle pool to be refilled for future release

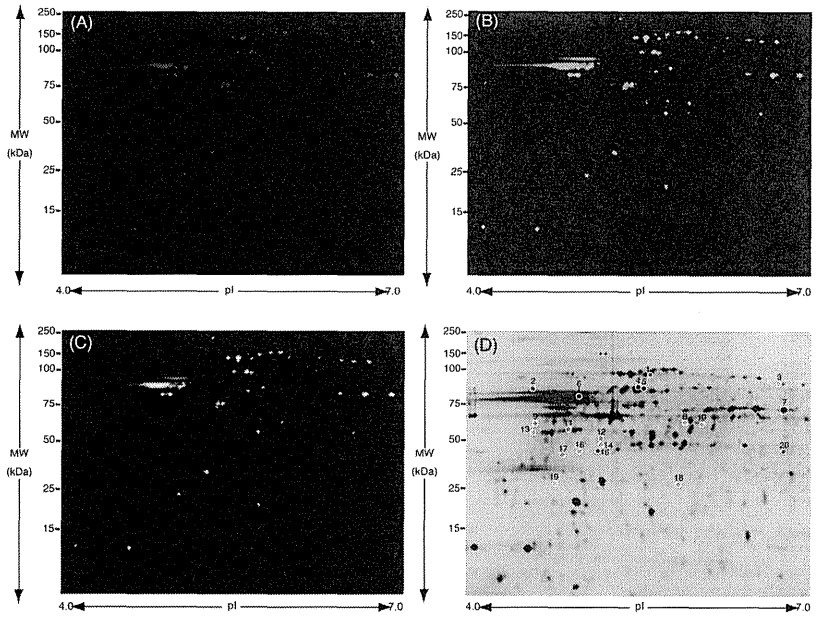

Fig. 1. 2D-DIGE gel image of fluorescence-labeled hippocampal proteins of non-transgenic and $APP_{E693\Delta}$-transgenic mice. (A) Analysis of the proteome of non-transgenic mice hippocampi with Cy3 Dye. (B) $APP_{E693\Delta}$-transgenic mice hippocampi with Cy5 Dye. (C) Merged. (D) Fourteen protein spots identified from non-transgenic and $APP_{E693\Delta}$-transgenic mice hippocampi by LC/MS/MS. Black numbers with white circles indicate proteins that are listed in Table 1.

Table 1
Identified proteins from differentially expressed in the hippocampus of$APP_{E693\Delta}$-transgenic mice when compared to non-transgenic littermates.

Spot no.	Protein ID	Fold (APP/WT)	*t*-Test	Accession	Coverage	#Peptides	Predicted MW (kDa)	Calc. pI	Score
1	Heat shock-related 70 kDa protein 2	−1.32	0.040	P14659	26.22	23	69.6	5.67	625.70
2	Neurofilament light polypeptide	−1.48	0.002	P08551	39.96	43	61.5	4.64	1004.84
3	Stress-induced-phosphoprotein 1	−1.44	0.002	Q60864	16.21	9	62.5	6.80	157.49
4	60 kDa heat shock protein	−1.36	0.013	P63038	52.71	71	60.9	6.18	1916.39
5	Alpha-internexin	−1.34	0.023	P46660	42.66	39	55.7	5.27	1119.47
6	Protein kinase C and cascin kinase substrate in neurons protein 1	−1.48	0.023	Q61644	28.34	15	50.5	5.24	356.92
7	Alpha-enolase	−1.32	0.000	P17182	34.33	24	47.1	6.80	474.21
8	Actin, cytoplasmic 1	1.51	0.003	P60709	25.87	14	41.7	5.48	231.79
9	Heat shock cognate 71 kDa protein	1.35	0.015	P63017	12.54	16	70.8	5.52	319.85
10	Actin, cytoplasmic	1.34	0.004	P60709	24.27	13	41.7	5.48	279.37
11	Actin, cytoplasmic 1	1.38	0.022	P60709	15.47	7	41.7	5.48	243.14
12	Actin, cytoplasmic 1	−1.56	0.013	P60709	22.67	12	41.7	5.48	131.57
13	Gamma-enolase	1.33	0.005	P17183	20.05	13	47.3	5.11	237.25
14	ATP synthase subunit beta	1.40	0.047	P56480	23.60	18	56.3	5.34	356.19
15	Tubulin beta-2A chain	1.31	0.021	Q13885	14.83	13	49.9	4.89	313.07
16	Actin, cytoplasmic 1	1.47	0.002	P60709	6.93	3	41.7	5.48	97.01
17	Tubulin beta-2S chain	1.44	0.009	Q13885	11.46	5	49.9	4.89	118.50
18	Clathrin light chain B	1.68	0.005	P09497	8.30	3	25.2	4.64	95.06
19	ATP synthase subunit beta	1.46	0.013	P06576	16.64	16	56.5	5.40	283.06
20	Dynamin-1	1.40	0.006	Q05193	9.61	13	97.3	7.17	242.16

Mass spectrometry protein identification of 2D-DIGE spots of interest and statistical analysis using *t*-test between wild type mice and $APP_{E693\Delta}$-transgenic mice gels ($P < 0.05$). The proteins of mouse hippocampus were separated by 2DE and identified by LC MS/MS, following in-gel digestion with trypsin. The spots representing identified proteins are indicated in Fig. 1D and are designated with their ID accession numbers of Swiss Prot database. Score relates to the probability assignment. Score and sequence coverage were calculated by MASCOT search engine (http://www.matrixscience.com).

Table 2
Functions regulated by proteins that showed an altered expression in $APPE_{693\Delta}$-transgenic mouse hippocampus.

Function	Identified protein	Up/down
Cytoskeletal and their interacting proteins	Neurofilament light polypeptide	Down
	Alpha-internexin	Down
	Actin, cytoplasmic 1	Up/down
	Tubulin β-2A Chain	Up
Chaperone and their interacting proteins	Stress-induced-phosphoprotein 1	Down
	60 kDa heat shock protein	Down
	Heat shock cognate 71 kDa protein	Down
Energy metabolic proteins	Alpha-enolase	Down
	Gamma-enolase	Up
	ATP synthase subunit beta	Up
Vesicle transport and recycling	Dynamin-1	Up
	Clathrin light chain B	Up
Signaling proteins	Protein kinase C and casein kinase substrate in neurons protein 1	Down

The analysis of proteins function was done by using MOTIF (http://www.genome.jp/tools/motif/).

[12]. The amount of dynamin was significantly increased. Our findings in $APP_{E693\Delta}$-transgenic mice without plaque deposition are consistent with previous findings that protein levels of dynamin were increased in Tg2576 mice with plaque deposition [21], suggesting that the release of neurotransmitter is affected by dynamin increased irrespective of AD stage. Also, spot no. 6 was identified as Pacsin 1. The Pacsin 1 is colocalized, oligomerized and bound with dynamin, and both proteins participate in synaptic vesicle endocytosis [17]. The amount of Pacsin 1 was significantly increased. Taken together, Pacsin 1 and dynamin enhanced by Aβ oligomers

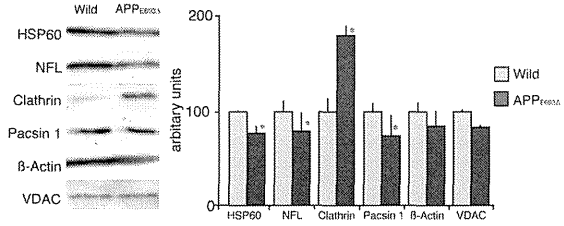

Fig. 2. Differentially expressed proteins validated by Western blotting for the hippocampus of non-transgenic and $APP_{E693\Delta}$-transgenic mice. (A) The levels of HSP60, NFL, clathrin, Pacsin 1, β-actin and VDAC in individual samples of each group were detected. (B) Graphical representation of the semi quantitative analysis (mean ± SEM of O.D. of bands). Data are presented as mean ± SEM ($n = 4$) *t*-test; $^*P < 0.05$ vs. $APP_{E693\Delta}$-transgenic mice.

might change the function of synaptic vesicle in the hippocampus of AD.

Spot no. 18 was identified as clathrin, which is known as the major protein of the polyhedral coat of coated pits and vesicles [7]. The amount of spot no. 18 was significantly decreased. APP was associated clusters of clathrin-coated vesicles and endosomes [3]. Thus, Aβ oligomers might inhibit the vesicle formation by clathrin.

In addition, we performed a validation experiment for HSP60, NFL, clathrin, Pacsin 1 and β-actin as the altered proteins, and VDAC as the unchanged protein (as control) [23]. The increased levels of clathrin, the decreased levels of HSP60, NFL, and Pacsin 1 and the unchanged level of β-actin and VDAC in $APP_{E693\Delta}$-transgenic mice hippocampus were validated by Western blotting (Fig. 2).

In summary, we identified the altered levels of 14 proteins in $APP_{E693\Delta}$-transgenic mice hippocampus using 2D-DIGE and LC–MS/MS approach. This approach elucidated the pathological effects of Aβ oligomers on hippocampus. Our findings might provide a clue for investigation of the hippocampus of AD early stage.

Acknowledgements

This work was supported by grants from Kobe Gakuin University for Collaborative Research C and the Smoking Research Foundation. The authors thank Dr. Tadanori Mayumi for his encouragement during the early days of the study.

References

[1] U. Andersson, H. Antonicka, J. Houstek, B. Cannon, A novel principle for conferring selectivity to poly(A)-binding proteins: interdependence of two ATP synthase beta-subunit mRNA-binding proteins, Biochemical Journal 346 (Pt 1) (2000) 33–39.
[2] C.L. Chien, R.K. Liem, Characterization of the mouse gene encoding the neuronal intermediate filament protein alpha-internexin, Gene 149 (1994) 289–292.
[3] A. Ferreira, A. Caceres, K.S. Kosik, Intraneuronal compartments of the amyloid precursor protein, Journal of Neuroscience 13 (1993) 3112–3123.
[4] T.A. Fulga, I. Elson-Schwab, V. Khurana, M.L. Steinhilb, T.L. Spires, B.T. Hyman, M.B. Feany, Abnormal bundling and accumulation of F-actin mediates tau-induced neuronal degeneration in vivo, Nature Cell Biology 9 (2007) 139–148.
[5] A. Gorg, C. Obermaier, G. Boguth, A. Harder, B. Scheibe, R. Wildgruber, W. Weiss, The current state of two-dimensional electrophoresis with immobilized pH gradients, Electrophoresis 21 (2000) 1037–1053.
[6] J. Hardy, D.J. Selkoe, The amyloid hypothesis of Alzheimer's disease: progress and problems on the road to therapeutics, Science 297 (2002) 353–356.
[7] J. Hirst, M.S. Robinson, Clathrin and adaptors, Biochimica et Biophysica Acta 1404 (1998) 173–193.
[8] C.R. Hunt, A.J. Parsian, P.C. Goswami, C.A. Kozak, Characterization and expression of the mouse Hsc70 gene, Biochimica et Biophysica Acta 1444 (1999) 315–325.
[9] S. Ikawa, R.A. Weinberg, An interaction between p21ras and heat shock protein hsp60, a chaperonin, Proceedings of the National Academy of Sciences 89 (1992) 2012–2016.
[10] J.L. Johnson, A. Halas, G. Flom, Nucleotide-dependent interaction of Saccharomyces cerevisiae Hsp90 with the cochaperone proteins Sti1, Cpr6, and Sba1, Molecular and Cellular Biology 27 (2007) 768–776.
[11] M. Kaghad, X. Dumont, P. Chalon, J.M. Lelias, N. Lamande, M. Lucas, M. Lazar, D. Caput, Nucleotide sequences of cDNAs alpha and gamma enolase mRNAs from mouse brain, Nucleic Acids Research 18 (1990) 3638.
[12] B.L. Kelly, R. Vassar, A. Ferreira, Beta-amyloid-induced dynamin 1 depletion in hippocampal neurons. A potential mechanism for early cognitive decline in Alzheimer disease, Journal of Biological Chemistry 280 (2005) 31746–31753.
[13] W.L. Klein, G.A. Krafft, C.E. Finch, Targeting small Abeta oligomers: the solution to an Alzheimer's disease conundrum? Trends in Neurosciences 24 (2001) 219–224.
[14] T.B. Kuhn, P.J. Meberg, M.D. Brown, B.W. Bernstein, L.S. Minamide, J.R. Jensen, K. Okada, E.A. Soda, J.R. Bamburg, Regulating actin dynamics in neuronal growth cones by ADF/cofilin and rho family GTPases, Journal of Neurobiology 44 (2000) 126–144.
[15] V.M. Lee, M. Goedert, J.Q. Trojanowski, Neurodegenerative tauopathies, Annual Review of Neuroscience 24 (2001) 1121–1159.
[16] S. Li, S. Hong, N.E. Shepardson, D.M. Walsh, G.M. Shankar, D. Selkoe, Soluble oligomers of amyloid Beta protein facilitate hippocampal long-term depression by disrupting neuronal glutamate uptake, Neuron 62 (2009) 788–801.
[17] J. Modregger, B. Ritter, B. Witter, M. Paulsson, M. Plomann, All three PACSIN isoforms bind to endocytic proteins and inhibit endocytosis, Journal of Cell Science 113 (Pt 24) (2000) 4511–4521.
[18] R.A. Nixon, R.K. Sihag, Neurofilament phosphorylation: a new look at regulation and function, Trends in Neurosciences 14 (1991) 501–506.
[19] R.A. Robinson, M.B. Lange, R. Sultana, V. Galvan, J. Fombonne, O. Gorostiza, J. Zhang, G. Warrier, J. Cai, W.M. Pierce, D.E. Bredesen, D.A. Butterfield, Differential expression and redox proteomics analyses of an Alzheimer disease transgenic mouse model: effects of the amyloid-beta peptide of amyloid precursor protein, Neuroscience 177 (2011) 207–222.
[20] D.J. Selkoe, Alzheimer's disease is a synaptic failure, Science 298 (2002) 789–791.
[21] S.J. Shin, S.E. Lee, J.H. Boo, M. Kim, Y.D. Yoon, S.I. Kim, I. Mook-Jung, Profiling proteins related to amyloid deposited brain of Tg2576 mice, Proteomics 4 (2004) 3359–3368.
[22] R. Sultana, D. Boyd-Kimball, J. Cai, W.M. Pierce, J.B. Klein, M. Merchant, D.A. Butterfield, Proteomics analysis of the Alzheimer's disease hippocampal proteome, Journal of Alzheimer's Disease 11 (2007) 153–164.
[23] M. Takano, K. Maekura, M. Otani, K. Sano, T. Nakamura-Hirota, S. Tokuyama, K.S. Min, T. Tomiyama, H. Mori, S. Matsuyama, Proteomic analysis of the brain tissues from a transgenic mouse model of amyloid beta oligomers, Neurochemistry International 61 (2012) 347–355.
[24] M. Takano, M. Otani, A. Sakai, K. Kadoyama, S. Matsuyama, A. Matsumoto, M. Takenokuchi, M. Sumida, T. Taniguchi, Use of a phosphosensor dye in proteomic analysis of human mutant tau transgenic mice, Neuroreport 20 (2009) 1648–1653.
[25] T. Tomiyama, S. Matsuyama, H. Iso, T. Umeda, H. Takuma, K. Ohnishi, K. Ishibashi, R. Teraoka, N. Sakama, T. Yamashita, K. Nishitsuji, K. Ito, H. Shimada, M.P. Lambert, W.L. Klein, H. Mori, A mouse model of amyloid beta oligomers: their contribution to synaptic alteration, abnormal tau phosphorylation, glial activation, and neuronal loss in vivo, Journal of Neuroscience 30 (2010) 4845–4856.

blood

2013 121: 2804-2813
Prepublished online January 30, 2013;
doi:10.1182/blood-2012-12-468363

Robo4 is an effective tumor endothelial marker for antibody-drug conjugates based on the rapid isolation of the anti-Robo4 cell-internalizing antibody

Mai Yoshikawa, Yohei Mukai, Yoshiaki Okada, Yuki Tsumori, Shin-ichi Tsunoda, Yasuo Tsutsumi, William C. Aird, Yasuo Yoshioka, Naoki Okada, Takefumi Doi and Shinsaku Nakagawa

Blood (print ISSN 0006-4971, online ISSN 1528-0020), is published weekly by the American Society of Hematology, 2021 L St, NW, Suite 900, Washington DC 20036.

VASCULAR BIOLOGY

Robo4 is an effective tumor endothelial marker for antibody-drug conjugates based on the rapid isolation of the anti-Robo4 cell-internalizing antibody

Mai Yoshikawa,[1] Yohei Mukai,[1,2] Yoshiaki Okada,[1] Yuki Tsumori,[1] Shin-ichi Tsunoda,[2] Yasuo Tsutsumi,[1,2] William C. Aird,[3] Yasuo Yoshioka,[1] Naoki Okada,[1] Takefumi Doi,[1] and Shinsaku Nakagawa[1]

[1]Graduate School of Pharmaceutical Sciences, Osaka University, Osaka, Japan, [2]Laboratory of Biopharmaceutical Research, National Institute of Biomedical Innovation (NiBio), Osaka, Japan, [3]Center for Vascular Biology Research and Division of Molecular and Vascular Medicine, Beth Israel Deaconess Medical Center, Boston, MA

Key Points

- First therapeutic application that targets Robo4 on the tumor blood vasculature
- High-throughput screening system to isolate cell-internalizing monoclonal antibodies useful to develop effective antibody-drug conjugates

Monoclonal antibodies (mAbs) that are internalized into cells are a current focus in the development of antibody-drug conjugates (ADCs). We describe a phage display–based high-throughput screening system to rapidly isolate cell-internalizing mAbs. We simultaneously examined the cell-internalizing activities of several hundred independent mAbs and successfully isolated cell-internalizing mAbs against the tumor endothelial markers Roundabout homolog 4 (Robo4) and vascular endothelial growth factor receptor 2 (VEGFR2). Tumor accumulation of mAbs with high cell-internalizing activity was significantly higher than that of mAbs with low cell-internalizing activity. Furthermore, the antitumor effects of ADCs of mAbs with high cell-internalizing activity were significantly stronger than those of mAbs with low cell-internalizing activity. Although anti-VEGFR2 therapy caused a significant loss of body weight, anti-Robo4 therapy did not. These findings indicate that cell-internalizing activity plays an important role in the biodistribution and therapeutic effects of ADCs. Further, Robo4 can be an effective marker for tumor vascular targeting. (*Blood.* 2013;121 (14):2804-2813)

Introduction

Antibody drug conjugates (ADCs), ie, monoclonal antibodies (mAbs) labeled with certain anticancer agents, are currently the focus of antibody-based drug discovery. ADCs have mAb-derived specificity and allow for targeted delivery of cytotoxic drugs to a tumor, which is expected to significantly enhance the antitumor activity of mAbs.[1] Trastuzumab ematansine (T-DM1)[2] for human epidermal growth factor receptor 2 (Her-2)–positive breast cancer and brentuximab vedotin (SGN-35)[3] for relapsed or refractory CD30-positive lymphoproliferative disorders are now in phase 3 clinical trials as effective ADCs.[4] ADCs will have an important role in overcoming some types of refractory cancers and will contribute to the field of tumor vascular targeting.[5]

An essential property of ADCs is that the mAb should be efficiently internalized into the cell where the cytotoxic effects of anticancer drugs occur.[1] The isolation of mAbs with high cell-internalizing activity (cell-internalizing mAbs) is a limiting factor in the development of ADCs. The discovery of potent cell-internalizing mAbs, however, requires labor-intensive screening of a massive number of candidates, and therefore the development of phage display–based methods to identify these candidates is highly desirable.[6,7] In the phage display–based method, a phage antibody library is added to the desired cells and then phages bound to the cell surface are removed. Only internalized phages are rescued from the intracellular compartment. Even with this method, however, the internalizing activities of individual antibody candidates must be assessed, because the concentrated phage pool comprises a "polyclonal" population. To address this issue, we used high-throughput screening methods to estimate "monoclonal" cell-internalization activities using a protein synthesis inhibitory factor (PSIF),[8] which provided a breakthrough in reducing the time-consuming screening of the cell-internalizing activity.

PSIF is a fragment of a bacterial exotoxin derived from *Pseudomonas aeruginosa*.[9] PSIF lacks its cell binding domain, and its cytotoxic portion is used in a recombinant immunotoxin.[10] Upon entry into the cell, PSIF has strong cytotoxicity by inducing ADP-ribosylation of elongation factor-2, which is essential for protein synthesis.[11] Our group previously accelerated the identification of cell-internalizing novel protein transduction domains (PTDs) by expressing PTD-PSIF fusion proteins in the supernatant of *Escherichia coli*.[8] Using this system, we successfully discovered superior HIV-Tat PTD mutants by simultaneously estimating

Submitted December 3, 2012; accepted January 22, 2013. Prepublished online as *Blood* First Edition paper, January 30, 2013; DOI 10.1182/blood-2012-12-468363.

M.Y. and Y.M. contributed equally to this study.

The online version of this article contains a data supplement.

The publication costs of this article were defrayed in part by page charge payment. Therefore, and solely to indicate this fact, this article is hereby marked "advertisement" in accordance with 18 USC section 1734.

the cell-internalizing activities of several hundred monoclonal PTD-PSIF fusions.[8] Therefore, we expect this method to contribute to the identification of mAbs with high cell-internalizing activity (cell-internalizing mAbs) by expressing single-chain antibody Fv (scFv)-PSIF fusion proteins to estimate the cell-internalizing activities of a very large number of antibodies.

Roundabout homolog 4 (Robo4) is a potential tumor angiogenesis marker.[12] Robo4 expression is restricted to areas of in vivo angiogenesis[13,14] and the subpopulation of hematopoietic stem cells localized in the bone marrow.[15] At angiogenic sites, Robo4 is present in the endothelial lining of blood vessels in the developing embryo,[16] placenta,[14] and tumors.[17] We previously confirmed the endothelial cell–specific expression of Robo4 using transgenic mouse lines.[18,19] Robo4 acts as a receptor that modulates vascular endothelial growth factor A (VEGF)–VEGF receptor (VEGFR) signaling.[20-23] Therefore, Robo4 is a potential marker for tumor vascular targeting because angiogenesis is only activated in tumors in the adult,[24] with the exception of some pathological states.[25,26] Another potential tumor angiogenesis marker is VEGFR2, a well-established tumor endothelial marker.[27] The VEGF-VEGFR2 signaling pathway plays a crucial role in angiogenesis, and anti-VEGF mAbs and small molecule inhibitors against VEGFR are approved for various types of cancers.[28] Anti-VEGFR2 mAbs are also used for tumor vascular targeting.[29] Although VEGFR2 is strongly expressed in active angiogenic sites, its expression is also observed in normal tissues.[30] Hypertension and proteinuria are common side effects of anti-VEGF therapy because VEGF-VEGFR signaling is also inhibited in normal tissue, including the kidney, heart, and resistance vessels.[31-33]

Here we applied the PSIF system to search for novel cell-internalizing mAbs from an immune phage antibody library. Application of this method to Robo4 and VEGFR2 led to the successful discovery of anti-Robo4 and anti-VEGFR2 cell-internalizing mAbs, as well as mAbs with low cell-internalizing activity (low-internalizing mAbs) to be used as controls. Comparing mAbs with different cell-internalizing activities revealed that higher cell-internalizing activity enhanced the tumor targeting potency of mAbs. Furthermore, comparative studies with anti-Robo4 and anti-VEGFR2 cell-internalizing mAbs in vivo indicated that Robo4 was superior to VEGFR2 in terms of the therapeutic window. This is the first report demonstrating the benefits of cell-internalizing mAbs in tumor vascular targeting. Further, these findings demonstrate the potential of Robo4 as a target for further development of novel ADCs against tumor blood vasculature.

Materials and methods

Cell culture

MS1 immortalized murine endothelial cells were cultured in Dulbecco's Modified Eagle Medium containing 5% fetal bovine serum 1% antibiotic-antimycotic mixed solution. B16BL6 murine melanoma cells were cultured in minimum essential medium containing 10% fetal bovine serum and 1% antibiotic-antimycotic mixed solution at 37°C. These cells were maintained at 37°C under a humidified 5% CO_2 atmosphere.

B16BL6 tumor-bearing mice

B16BL6 cells (1×10^6 cells/100 μL) were inoculated intracutaneously into 6-week-old female C57BL6 mice (Japan SLC Inc., Shizuoka, Japan) (day 0). Biodistribution was analyzed on the day that the tumor width reached 10 mm. The therapy experiment was started on day 3. As a validation of the model, we confirmed the expressions of VEGFR2 and Robo4 on the tumor endothelium, based on the immunofluorescence against B16BL6 tumor sections.

Antigens

Human VEGFR2 (hVEGFR2) and mouse VEGFR2 (mVEGFR2) were commercial recombinant proteins (Merck Chemicals, Inc., Darmstadt, Germany, or R&D Systems, Inc., Minneapolis, MN). Human Robo4 (hRobo4) and mouse Robo4 (mRobo4) were produced as described previously.[34]

Immune phage antibody libraries

Phage antibody libraries were constructed from the spleen and bone marrow cells of immunized mice as previously described.[35,36] Our phage antibody library comprised single-chain Fv fragment (scFv) fused with pIII phage coat protein. Four rounds of affinity panning were performed against hVEGFR2 and mVEGFR2 for the anti-VEGFR2 immune library, and against hRobo4 and mRobo4 for the anti-Robo4 immune library. Anti-FLAG panning was followed by each panning to concentrate the scFv-displaying phages, as described previously.[36]

ELISA and cytotoxicity assay using TG1 supernatant

Plasmids were extracted from TG1 cells after the fourth panning against mVEGFR2 or mRobo4. These "enriched" scFv gene libraries were cloned into a PSIF-fusion expression vector derived from pCANTAB5E.[8] Monoclonal scFv-PSIF protein was induced in the TG1 supernatant, as previously described.[8] mVEGFR2 or mRobo4 was immobilized on an immunoassay plate and blocked with 4% skim milk in phosphate-buffered saline (PBS) (4% MPBS) at 37°C for 2 hours. TG1 supernatant containing 2% MPBS was reacted with antigens at room temperature for 1 hour. Bound scFv-PSIFs were detected by anti–FLAG-horseradish peroxidase (M2, Sigma-Aldrich Corporation, St. Louis, MO). For the cytotoxicity assay, MS1 cells were seeded on a 96-well plate at 1.0×10^4 cells/well. After incubation at 37°C for 24 hours, TG1 supernatant was diluted in MS1 culture medium, and then added to the MS1 cells. After incubation at 37°C for 24 hours, cell viability was assessed using a WST-8 assay (Dojindo Molecular Technologies, Inc., Kumamoto, Japan). The viability of nontreated MS1 and completely killed MS1 with 1 mM cycloheximide were defined as 100% and 0%, respectively.

Expression and purification of scFv, dscFv, and scFv-PSIF recombinant protein

The isolated scFv gene with 15 amino acids linker (VL-GGGGSGGG GSGGGGS-VH) was cloned into modified pET15b vector, resulting in the scFv fused by FLAG-tag and His×6 tag at the C-terminus. A scFv gene with a 5–amino acid linker (VL-GGGGS-VH) was also cloned into modified pET15b, resulting in a noncovalent scFv dimer (dscFv) fused by FLAG-tag and His×6 tag at the C-terminus. An anti-His scFv gene was also cloned but only a FLAG-tag was fused at the C-terminus. A scFv gene with a 15–amino acid linker was cloned into pYas-PSIF vectors.[37] ScFvs, dscFvs, and scFv-PSIFs were purified from inclusion bodies in *E coli* according to the previously described methods.[37] The binding affinity of each recombinant protein was assessed by surface plasmon resonance using BIAcore3000 (GE Healthcare UK Ltd., Chalfont, United Kingdom).

Expression and purification of IgG recombinant protein

IgG recombinant proteins were expressed using an OptiCHO antibody expression kit (Invitrogen Corporation, Carlsbad, CA) according to the manufacturer's instructions. IgGs were purified from cell culture supernatant with protein G column (GE Healthcare). Eluted fractions were further purified with Superdex 200 column (GE Healthcare). Anti-FLAG[IgG] (anti-FLAG M2 antibody) was purchased from Sigma-Aldrich.

Preparation of IgG-NCS

NCS was kindly provided by Kayaku Co, Ltd., Tokyo, Japan. NCS was thiolated by incubating it with 10 molar excess 2-iminothiolane (Thermo Fisher Scientific Inc., Waltham, MA) for 1 hour at room temperature. IgG recombinant proteins were reacted with 10 molar excess of SPDP

crosslinker (*N*-succinimidyl 3-[2-pyridyldithio]-propionate; Thermo Fisher) for 30 minutes on ice. SPDP-modified IgGs and thiolated NCS were separately purified using NICK columns (GE Healthcare). They were then mixed for 8 hours at room temperature. IgG-NCS were purified with a Superdex 200 column. Modification efficiency was quantified after sodium-dodecyl sulfate-polyacrylamide gel electrophoresis using a Gel DOC EZ system and Image laboratory software (Bio-Rad Laboratories, Inc., Hercules, CA).

Labeling of purified mAbs

For fluorescent labeling, mAbs were labeled using Cy5.5-NHS (GE Healthcare). For ^{125}I labeling, 100 μg mAbs in 0.4 M phosphate buffer were labeled with 0.2 mCi $Na^{125}I$ (PerkinElmer, Inc., Waltham, MA) based on the chloramine-T method.[38] For biotin labeling, mAbs were biotinylated using EZ-Link Sulfo-NHS-Biotin (Thermo Fisher). Each mAb was purified using a NICK desalting column (GE Healthcare).

Flow cytometry

Cy5.5-labeled mAb ($mAb^{Cy5.5}$; 4 μM) was incubated with 5.0×10^5 cells of MS1 cells in 6-well plates for 2 hours at 4°C. After washing three times, the cells were incubated for an additional 0.5 to 8 hours at 37°C. At each time point, cells were collected in 2-mM ethylenediaminetetraacedtic acid/PBS. Bound mAbs were digested using 0.1% trypsin/PBS at 37°C for 20 minutes (trypsinized group) or PBS (nontrypsinized group). Cellular fluorescence was measured by Gallios flow cytometer (Beckman Coulter, Inc., Miami, FL). The ratio of internalization was calculated using the following formula: internalization (%) = {internalized $mAb^{Cy5.5}$}/{total bound $mAb^{Cy5.5}$} × 100 (%) = {(MFI of $mAb)_T$ − (MFI of anti-His [mAb])$_T$}/{(MFI of $mAb)_N$ − (MFI of anti-His[mAb])$_N$} × 100 (%). MFI indicates mean fluorescence intensity. T and N indicate trypsinized and nontrypsinized groups, respectively.

In vivo biodistribution

$dscFvs^{125I}$ (0.2 nmol) was intravenously injected into B16BL6 tumor–bearing mice. At 2 hours and 24 hours after injection, the radioactivity of each organ was counted using the Wizard 2480 γ-ray counter (PerkinElmer). %ID/g tissue was calculated using following formula: %ID/g tissue = (count/g tissue)/(total injected count) × 100 (%). Two individual experiments were combined for the final data (total 11 mice/group).

Immunofluorescence of the tissue sections

B16BL6 tumor–bearing mice were administered 2 nmol of $dscFvs^{Bio}$. At 2 hours after the injection, the tumors, kidneys, and hearts were embedded in optimal cutting temperature compound (Sakura Finetek, Inc., Torrance, CA) and frozen in liquid nitrogen. Thin sections (7 μm) were prepared using a Cryostat CM1850 (Leica Microsystems GmbH, Wetzlar, Germany) and fixed in 4% paraformaldehyde. $dscFvs^{Bio}$ in the sections were stained with streptavidin phycoerythrin conjugate (eBioscience Inc., San Diego, CA) in Dako REAL Antibody Diluent (DAKO Corporation, Carpinteria, CA). CD31+ vascular endothelial cells were stained with rat anti-CD31 antibody (MEC13.3; Becton Dickinson and Company, Franklin Lakes, NJ) in Dako REAL Antibody Diluent and Alexa488 conjugated anti-rat IgG (A11006; Invitrogen). The samples were embedded with Prolong Gold antifade reagent with 4′,6-diamidino-2-phenylindole (Invitrogen) and observed with a fluorescence microscope FSX100 (Olympus Corporation, Tokyo, Japan).

In vivo therapy experiments

Activities of scFv-PSIFs and IgG-NCSes were confirmed by WST-8 assay as described before. B16BL6 cells were inoculated intracutaneously into C57BL6 mice (Japan SLC) on day 0. Mice were intravenously injected with 15 pmol scFv-PSIFs and 10 pmol IgG-NCSs on days 3, 5, 7, 9, and 11 (7 mice/group). The volume of the tumor was calculated according to the following formula: tumor volume (mm^3) = {major axis of tumor (mm)} × {minor axis of tumor (mm)}^{2} × 0.4.

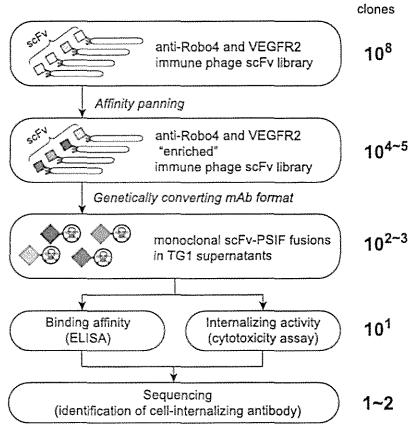

Figure 1. Phage display-based method to search for cell-internalizing mAbs. The phage antibody library was "enriched" by affinity panning against the desired antigens. Plasmids encoding scFvs were collected from TG1 *E coli* strains infected by "enriched" phage libraries. Genes of scFvs were digested out and ligated into a PSIF fusion protein expression vector. These plasmids were then transformed to TG1, and then single colonies were picked up. From these individual colonies, monoclonal scFv-PSIF fusions were induced in TG1 supernatants. Using these fusion proteins, binding affinities and internalizing activities of several hundreds of scFv-PSIFs were easily estimated by ELISA and cytotoxicity assays, respectively. Finally, genes of positive scFvs were collected from TG1, and cell-internalizing scFvs were identified by sequencing. In this report, we used anti-Robo4 and anti-VEGFR2 immune phage scFv libraries as the phage antibody libraries, and mRobo4 and mVEGFR2 as the desired antigens.

Results

High-throughput screening for cell-internalizing mAbs

To identify cell-internalizing mAbs, we applied the phage immune scFv library to high-throughput screening of cell-internalizing molecules based on the PSIF system[8] (Figure 1). Our anti-Robo4 or anti-VEGFR2 phage library comprised approximately 3.0×10^8 or 5.0×10^8 independent scFvs, which was validated by sequence analysis. To assess the qualities of the libraries, affinity panning was performed against each antigen. During the panning, output phages were increased, suggesting that the desired scFvs were enriched in the library (supplemental Figure 1A-B,E-F). After the fourth panning, >40% of monoclonal scFvs showed specific binding in enzyme-linked immunosorbent assay (ELISA) (supplemental Figure 1C-D,G-H).

To validate the efficacy of cell-internalizing mAbs in a mouse model, we selected libraries enriched against murine antigens (mRobo4 and mVEGFR2) and chose MS1 murine endothelial cells for the screening of cell-internalizing mAbs because we confirmed the expressions of both mRobo4 and mVEGFR2 in MS1 cells using reverse transcriptase–polymerase chain reactioin. For the screening, scFv genes obtained after the fourth round of panning were cloned into the PSIF expression vector. Monoclonal scFv-PSIFs were expressed in TG1 supernatants (315 clones per library). For anti-Robo4s, 178 of 315 clones bound to mRobo4 in ELISA and 20 of these 178 binders were cytotoxic against MS1 cells

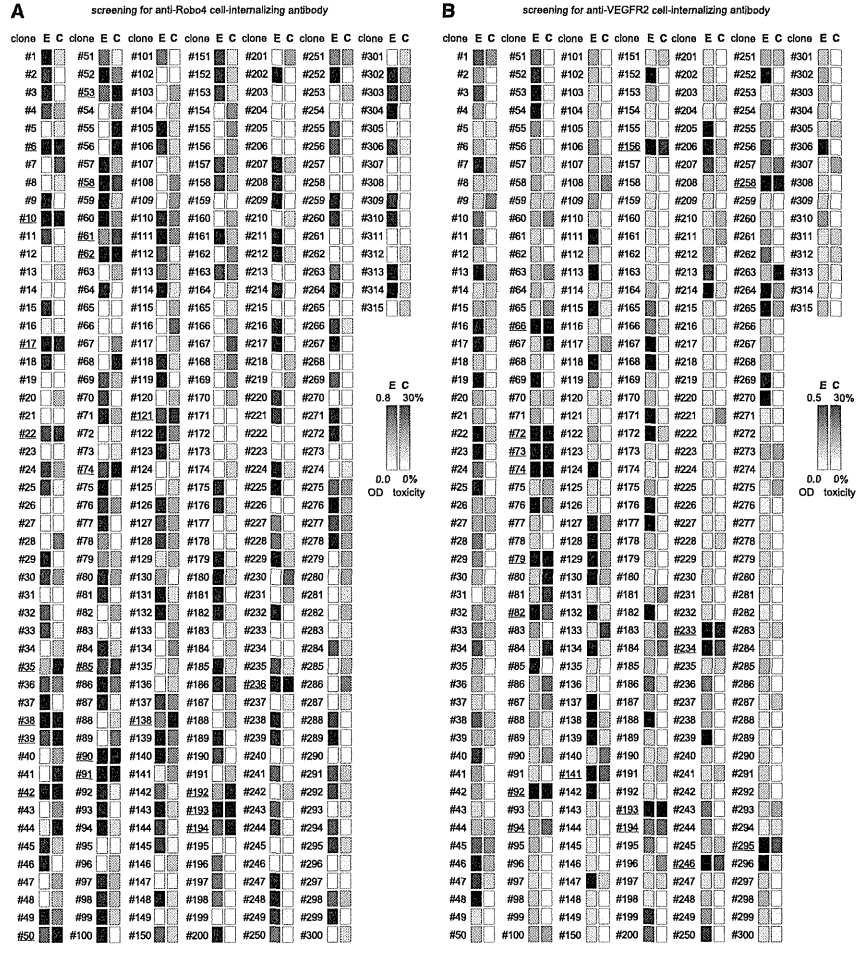

Figure 2. Screening of cell-internalizing mAbs (ELISA and cytotoxicity assay). To screen for cell-internalizing mAbs, 315 clones per antigen were analyzed by ELISA and cytotoxicity assay. (A) Result for Robo4, (B) Result for VEGFR2. Monoclonal scfv-PSIFs were induced in TG1 supernatant. The binding properties and cytotoxicities to MS1 cells were then assessed by an ELISA and WST-8 assay, respectively. E, ELISA results; C, WST-8 assay results. Individual results from ELISA (OD = 0.8 or 0.5~0.0) and WST-8 assay (cytotoxicity = 30%~0%) were mapped in grayscale densities. The 24 candidates against Robo4 and 17 candidates against VEGFR2 are indicated by the underline (ELISA OD ≥0.2 and cytotoxicity ≥20%). After omitting redundant clones by sequencing, 1 cell-internalizing mAb and 2 low-internalizing mAbs against mRobo4, and 2 cell-internalizing mAbs and 14 low-internalizing mAbs against mVEGFR2 were identified.

(Figure 2A). In a similar manner, for anti-VEGFR2s, 156 of 315 clones bound to VEGFR2 and 17 of the 156 binders were positive in the ELISA and cytotoxicity assays (Figure 2B). Sequence analysis to omit redundant clones revealed that these clones comprised 1 anti-Robo4 cell-internalizing mAb, 2 anti-Robo4 low-internalizing mAbs, 2 anti-VEGFR2 cell-internalizing mAbs, and 14 anti-VEGFR2 low-internalizing mAbs. For anti-Robo4s, only one anti-Robo4 cell-internalizing mAb was named "R4-13i" and a low-internalizing mAb with high affinity and low cytotoxicity was named "R4-16." In a similar manner, "V2-05i" and "V2-02" were selected as an anti-VEGFR2 cell-internalizing mAb and a low-internalizing mAb, respectively. After purification of the recombinant proteins, both anti-Robo4 scFvs bound to hRobo4, similar to mRobo4. Conversely, anti-VEGFR2 scFvs bound to

Table 1. Binding kinetics of antibodies in surface plasmon resonance analysis

Antibody	Target	Format	k_a ($M^{-1}s^{-1}$)	k_d (s^{-1})	K_D (M)
R4-13i	mRobo4	scFv	$1.25 \pm 0.36 \times 10^5$	$5.82 \pm 0.95 \times 10^{-4}$	$5.03 \pm 1.95 \times 10^{-9}$
(internalizing)		dscFv	$1.15 \pm 0.34 \times 10^6$	$5.98 \pm 0.61 \times 10^{-4}$	$5.64 \pm 2.21 \times 10^{-10}$
		IgG	$1.14 \pm 0.55 \times 10^6$	$4.19 \pm 1.70 \times 10^{-4}$	$2.22 \pm 0.51 \times 10^{-10}$
		scFv-PSIF	$7.22 \pm 4.31 \times 10^4$	$4.28 \pm 1.60 \times 10^{-3}$	$6.47 \pm 1.61 \times 10^{-8}$
		IgG-NCS	$1.02 \pm 0.15 \times 10^6$	$4.66 \pm 0.86 \times 10^{-4}$	$4.59 \pm 0.74 \times 10^{-10}$
R4-16	mRobo4	scFv	$1.30 \pm 0.33 \times 10^5$	$5.82 \pm 1.50 \times 10^{-4}$	$4.77 \pm 1.96 \times 10^{-9}$
(low-internalizing)		dscFv	$1.12 \pm 0.03 \times 10^6$	$5.91 \pm 1.50 \times 10^{-4}$	$5.31 \pm 1.96 \times 10^{-10}$
		IgG	$1.06 \pm 0.24 \times 10^6$	$3.60 \pm 0.85 \times 10^{-4}$	$2.76 \pm 0.16 \times 10^{-10}$
		scFv-PSIF	$8.90 \pm 1.42 \times 10^4$	$6.10 \pm 2.45 \times 10^{-3}$	$7.24 \pm 3.74 \times 10^{-8}$
		IgG-NCS	$1.07 \pm 0.12 \times 10^6$	$3.93 \pm 0.54 \times 10^{-4}$	$3.72 \pm 0.89 \times 10^{-10}$
V2-05i	mVEGFR2	scFv	$9.66 \pm 3.57 \times 10^4$	$4.40 \pm 0.95 \times 10^{-4}$	$5.13 \pm 2.61 \times 10^{-9}$
(internalizing)		dscFv	$8.75 \pm 2.03 \times 10^5$	$5.59 \pm 2.57 \times 10^{-4}$	$6.16 \pm 1.47 \times 10^{-10}$
		IgG	$1.14 \pm 0.09 \times 10^6$	$3.21 \pm 0.35 \times 10^{-4}$	$2.84 \pm 0.52 \times 10^{-10}$
		scFv-PSIF	$9.57 \pm 0.84 \times 10^4$	$6.51 \pm 1.87 \times 10^{-3}$	$6.94 \pm 2.63 \times 10^{-8}$
		IgG-NCS	$0.96 \pm 0.06 \times 10^6$	$4.37 \pm 0.90 \times 10^{-4}$	$4.52 \pm 0.79 \times 10^{-10}$
V2-02	mVEGFR2	scFv	$7.94 \pm 1.24 \times 10^4$	$4.28 \pm 3.23 \times 10^{-4}$	$5.07 \pm 3.05 \times 10^{-9}$
(low-internalizing)		dscFv	$8.94 \pm 2.55 \times 10^5$	$5.57 \pm 1.25 \times 10^{-4}$	$6.60 \pm 2.39 \times 10^{-10}$
		IgG	$1.13 \pm 0.22 \times 10^6$	$3.25 \pm 1.10 \times 10^{-4}$	$2.90 \pm 0.98 \times 10^{-10}$
		scFv-PSIF	$9.84 \pm 1.52 \times 10^4$	$5.75 \pm 2.05 \times 10^{-3}$	$5.81 \pm 1.93 \times 10^{-8}$
		IgG-NCS	$1.08 \pm 0.08 \times 10^6$	$5.25 \pm 1.58 \times 10^{-4}$	$4.85 \pm 1.30 \times 10^{-10}$

Binding kinetics were analyzed against mRobo4 (R4-13i and R4-16) or mVEGFR2 (V2-05i and V2-02). Values are shown as means ± SD from three different preparations.

k_a, association rate constant ($M^{-1}s^{-1}$); k_d, dissociation rate constant (s^{-1}); K_D, equilibrium dissociation constant (k_d/k_a) (M).

mVEGFR2, but not to hVEGFR2. We also confirmed using competitive ELISA that the mAbs did not share their antigen-binding epitopes (supplemental Figure 2).

Characterization of mAbs

We purified scFvs, dimerized scFvs (dscFvs), IgGs, and scFv-PSIF as recombinant proteins. IgGs conjugated with neocarzinostatin (IgG-NCSes) were also prepared for in vivo experiments. NCSes were confirmed to be conjugated to IgG molecules in the purified IgG-NCS fraction, and the efficiencies of the NCS modifications were similar in all IgG-NCSes (1.6~1.8 NCSes per single IgG). Surface plasmon resonance analysis revealed that cell-internalizing mAbs and low-internalizing mAbs had similar affinities against antigens in all antibody forms (Table 1).

To quantify the internalization, flow cytometry analysis was performed with Cy5.5-labeled mAbs ($scFv^{Cy5.5}$, $dscFv^{Cy5.5}$, and $IgG^{Cy5.5}$; Figure 3A,C). After $mAbs^{Cy5.5}$ bound to the cell surface, internalization was induced by incubation at 37°C for 2 hours. By removing cell-surface $mAbs^{Cy5.5}$ with trypsinization, the internalized $mAbs^{Cy5.5}$ were quantified by flow cytometry. At 2 hours, approximately 30% of cell-internalizing mAbs remained after trypsinization, whereas most of the low-internalizing mAbs were degraded (Figure 3A,C). This result clearly suggested that the internalization efficiencies differed between cell-internalizing mAbs and low-internalizing mAbs, even among the three different mAb forms. In a similar manner, a time-shift analysis revealed that >40% of cell-internalizing mAbs were internalized after 8 hours of incubation (Figure 3B,D). These findings indicate that only cell-internalizing mAbs were efficiently internalized into the cells, although low-internalizing mAbs had affinities similar to those of cell-internalizing mAbs (Table 1).

Intracellular localization

The intracellular behaviors of cell-internalizing mAbs were analyzed with a confocal laser-scanning microscope. In MS1 cells, intracellular fluorescence derived from $scFv^{Cy5.5}$ was observed with cell-internalizing scFvs, but not with low-internalizing scFvs (supplemental Figure 3A,D,E,H). Fluorescence was suppressed, however, under the inhibition of energy-dependent endocytosis (supplemental Figure 3B-C,F-G). These results suggested that cell-internalizing scFvs entered into the cells via energy-dependent endocytosis.

For in-depth analysis of the intracellular behavior, confocal laser-scanning microscope analysis was performed with immunostaining of endosome markers (supplemental Figure 3Iab). After $scFvs^{Cy5.5}$ were bound to the cell-surface, the cells were incubated for an additional 1 to 8 hours at 37°C. The early endosome marker, early endosome antigen 1 (EEA1), and the late endosome marker, lysosomal-associated membrane protein 1 (LAMP1), were visualized using Alexa488-conjugated antibodies. Colocalization with EEA1+ early endosomes decreased over time (supplemental Figure 3I-M,S-W), whereas colocalization with LAMP1+ late endosomes increased (supplemental Figure 3N-R,Xab). These findings suggested that cell-internalizing scFvs were encapsulated in EEA1+ early endosomes at an early stage and eventually accumulated in LAMP1+ late endosomes. This is thought to be a typical endocytotic molecular sorting pathway.[39]

Influence of cell-internalizing activity on biodistribution

To assess the biodistribution of cell-internalizing mAbs, ^{125}I-labeled dscFvs ($dscFv^{125I}$) were intravenously injected into B16BL6 tumor-bearing mice. In this experiment, we selected the dscFv form because dscFv has superior in vivo tumor-targeting potency compared with scFv.[40] At 2 hours, the tumor distribution of anti-Robo4 and anti-VEGFR2 $dscFvs^{125I}$ was similar to but significantly higher than that of a negative control $dscFv^{125I}$ (anti-His[$dscFv$]^{125I}; Figure 4A-B). This finding suggested that the anti-Robo4 and anti-VEGFR2 dscFvs had tumor-targeting properties. Anti-Robo4 $dscFvs^{125I}$ also accumulated in the kidney, indicating a nonspecific distribution of dscFvs for their elimination,[41,42] because no significant difference was observed between anti-Robo4 $dscFvs^{125I}$

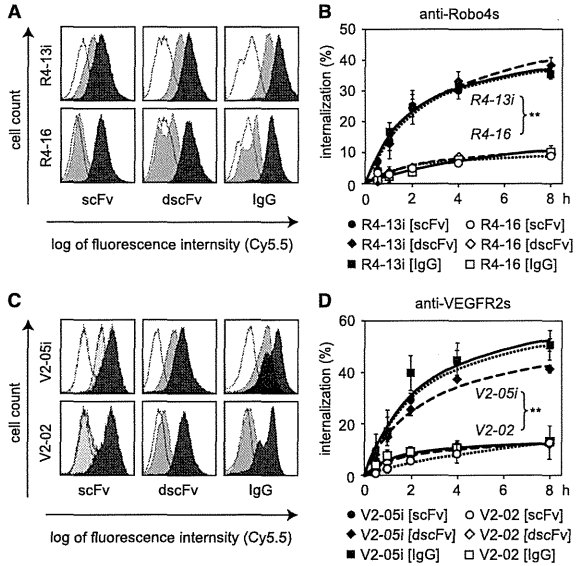

Figure 3. Cell internalization analyzed by flow cytometry. (A,C) Trypsinization to quantify internalized mAbs. Different forms of $mAbs^{Cy5.5}$ bound to the MS1 cells at 4°C. After washing out the unbound mAbs, internalization was induced for 2 hours at 37°C. To detect only internalized mAbs, cell surface proteins were trypsinized. The remaining cellular fluorescence was then analyzed by flow cytometry. (A) Anti-Robo4 $mAbs^{Cy5.5}$. (C) Anti-VEGFR2 $mAbs^{Cy5.5}$. Black, nontrypsinized group; gray, trypsinized group; white, negative control (*anti-His*[scFv]$^{Cy5.5}$, *anti-His*[dscFv]$^{Cy5.5}$, or *anti-FLAG* [IgG]$^{Cy5.5}$). (B,D) Time course of the internalization. After binding at 4°C, internalization was induced for 0.5, 1, 2, 4, or 8 hours at 37°C. The ratio of internalization was calculated using the following formula: internalization (%) = (internalized mAb)/(total bound mAb) × 100 (%) = ((MFI of mAb)$_T$ − (MFI of negative control)$_T$)/((MFI of mAb)$_N$ − (MFI of negative control)$_N$) × 100 (%). T, trypsinized group; N, nontrypsinized group; MFI, mean fluorescence intensity. (B) Closed and open markers indicate R4-13i and R4-16, respectively. (D) Closed and open markers indicate V2-05i and V2-02, respectively. (B,D) Circles, diamonds, and squares indicate scFv, dscFv, and IgG, respectively. Each experiment was performed in triplicate. Values are shown as means ± SD. $^{**}P < .01$; internalizing mAb versus low-internalizing mAb in each form by 2-way ANOVA (n = 3).

and anti-His[dscFv]^{125I} (Figure 4A). Importantly, the accumulation of anti-VEGFR2 dscFvs^{125I} in the kidney was significantly greater than that of anti-His[dscFv]^{125I} (Figure 4B). A similar accumulation of anti-VEGFR2 dscFvs^{125I}, but not anti-Robo4 dscFvs^{125I} (Figure 4A), was observed in the heart (Figure 4B).

To confirm this phenomenon, the localization of dscFvs in the tissues was analyzed by immunofluorescence studies (Figure 4E-S). Biotin-labeled dscFvs (dscFvs^{Bio}) were intravenously administered to B16BL6 tumor–bearing mice and the tumors, kidneys, and hearts were extracted 2 hours after injection. The dscFv^{Bio} and vascular endothelial cells were stained by streptavidin-AP and anti-CD31 antibody, respectively. In the tumor sections, all of the anti-Robo4 and anti-VEGFR2 dscFvs^{Bio} were clearly detected with CD31+ tumor blood vasculature, whereas anti-His[dscFv]^{Bio} was not detectable (Figure 4E,H,K,N,Q). This finding suggested that both anti-Robo4 and anti-VEGFR2 dscFvs recognized tumor endothelial cells in vivo, which contributed to their accumulation in the tumor. Interestingly, in the kidney and heart sections, signals around CD31+ blood vasculature were detectable only with the anti-VEGFR2 dscFvs^{Bio}, and not with anti-Robo4 dscFvs^{Bio} or anti-His[dscFv]^{Bio} (Figure 4F-G,I-J,L-M,O-P,R-S). This finding was compatible with the biodistribution results (Figure 4A-B), which suggested that anti-VEGFR2 dscFvs recognized VEGFR2 on normal blood vessels because VEGFR2 plays an important role in normal tissues, including the kidney and heart.[31-33] No specific accumulation of anti-Robo4 dscFvs was observed in normal tissues, suggesting that the anti-Robo4 mAbs were useful for specific tumor vascular targeting.

Comparison of the cell-internalizing mAbs and low-internalizing mAbs revealed a significantly greater accumulation of cell-internalizing dscFvs^{125I} in the tumors compared with low-internalizing dscFvs^{125I} at 24 hours (Figure 4C-D), whereas no differences were observed at 2 hours (Figure 4A-B). This finding suggested that cell-internalizing mAbs were retained in the tumor for a longer time than the low-internalizing mAbs. This phenomenon was also observed in the kidney and heart with the anti-VEGFR2 dscFvs (Figure 4D). This retention might be caused by the mAb internalization, which allowed the mAb to escape from the bloodstream and accumulate in the tumor blood endothelial cells. Taken together, these results suggest that mAb internalization into the tumor endothelium improves mAb-based drug-delivery in vivo.

Enhanced antitumor effect depends on the cell-internalizing activity

To assess the antitumor potencies of the cell-internalizing mAbs, we selected the scFv-PSIF and IgG-NCS forms. Both forms were suitable models of ADCs because both drugs are used clinically as successful anticancer medicines.[10,43] First, the in vitro cell-killing activities of scFv-PSIFs and IgG-NCSes were estimated by a cytotoxicity assay with MS1 cells (Figure 5A-D). Both forms of cell-internalizing mAbs showed an approximately 10-fold higher cytotoxicity than the low-internalizing mAbs. These findings clearly suggest that internalization enhanced the delivery of conjugated drugs into the cells because our cell-internalizing mAbs and low-internalizing mAbs had similar affinities against antigens (Table 1).

As the therapy experiment in vivo, scFv-PSIFs and IgG-NCSes were intravenously injected into B16BL6 tumor–bearing mice once every 2 days for a total of 5 injections (Figure 5E-H). All cell-internalizing mAbs significantly suppressed tumor growth, whereas the antitumor effects of the low-internalizing antibodies were

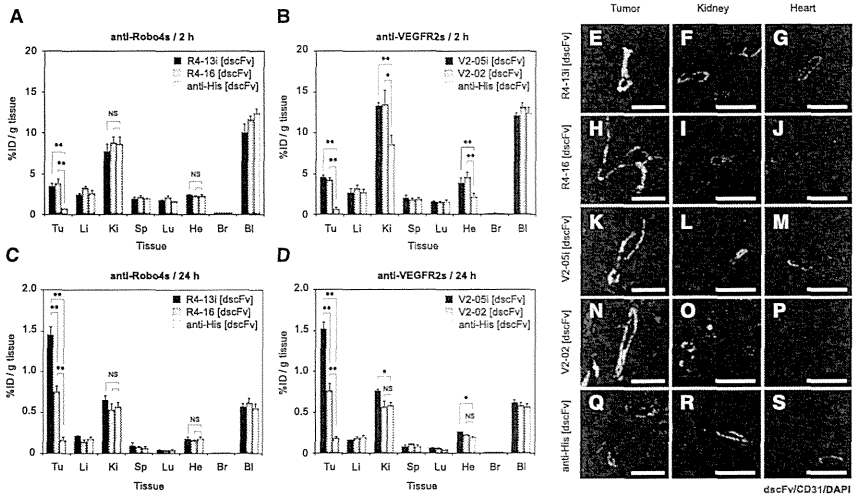

Figure 4. In vivo tumor-targeting activity of cell-internalizing mAbs. (A-D) Biodistribution of dscFvs in B16BL6 tumor–bearing mice. B16BL6 tumor–bearing mice were intravenously administered with anti-Robo4 dscFvs^{125I} (A,C) or anti-VEGFR2 dscFvs^{125I} (B,D). Each organ was extracted after 2 hours (A,B) or 24 hours (C,D), and the radioactivity was measured using a γ counter. %ID/g tissue was calculated using the following formula: %ID/g tissue = (count/g tissue)/(total injected count) × 100 (%). Tu, tumor; Li, liver; Ki, kidney; Sp, spleen; Lu, lung; He, heart; Br, brain; Bl, blood. (A,C) black; R4-13i[dscFv]^{125I}; gray, R4-16[dscFv]^{125I}; white, anti-His[dscFv]^{125I}. (B,D) black, V2-05i[dscFv]^{125I}; gray, V2-02[dscFv]^{125I}; white, anti-His[dscFv]^{125I}. Values are shown as means ± SEM. $^{*}P < .05$; $^{**}P < 0.01$; NS, not significant in Student's *t* test (n = 11). (E-S) Co-immunostaining of dscFvs with CD31^{+} blood endothelial cells on the tissue section. B16BL6 tumor–bearing mice were intravenously administered dscFvs^{Bio}. The tumor, kidney, and heart were extracted after 2 hours. Tissue sections of tumor, kidney, and heart were stained with streptavidin-PE conjugate. The blood vasculature was also stained with anti-CD31 antibody. Images were digitally merged. Red, dscFv^{Bio}; green, CD31; blue, DAPI (nucleus); yellow, colocalized region of red and green. Scale bar represents 100 μm. (E-G) R4-13i[dscFv]; (H-J) R4-16[dscFv]; (K-M) V2-05i[dscFv]; (N-P) V2-02[dscFv]; (Q-S) anti-His[dscFv]. (E,H,K,N,Q) Tumor section. (F,I,L,O,R) kidney section, and (G,J,M,P,S) heart section.

similar to those of the negative controls (anti-His[scFv]-PSIF and anti-FLAG[IgG]-NCS). The antitumor effects of R4-13i and V2-05i were similar in both ADC forms. These findings strongly suggest that the cell-internalizing activity of the mAbs was essential to maximize the delivery of the conjugated drug into the target cells, which significantly enhanced the antitumor effect of the ADCs.

Interestingly, the group of mice administered V2-05i[scFv]-PSIF had a significant loss of body weight, whereas the other groups did not (Figure 5I-L). As a preliminary result, 6 of 7 mice died in the V2-05i[scFv]-PSIF group with a similar protocol but with a fourfold higher dosage (60 pmol/mouse), perhaps because of the disruption of VEGFR2-positive cells in normal tissues by V2-05i[scFv]-PSIF, as shown in Figure 4. This side effect was not observed in the V2-05i [IgG]-NCS group. Therefore, we also hypothesized that the toxicity of NCS in normal cells was weak because NCS inhibits DNA synthesis in growing cells, such as tumor cells.[44] At a higher dosage, however, V2-05i[IgG]-NCS carries the risk of side effects. With regard to this point, none of the anti-Robo4 ADCs induced a loss of body weight; therefore, we concluded that Robo4 is a potential target for tumor vascular targeting with ADC.

Discussion

This study led to three novel findings. First, we demonstrated a rapid screening system for cell-internalizing mAbs in combination with the phage antibody library, which accelerated the identification of desired cell-internalizing mAbs. Second, comparative in vivo studies using cell-internalizing mAbs and low-internalizing mAbs with the same affinity values revealed that mAb internalization contributed to tumor targeting and enhanced the antitumor effects of the ADCs. Third, the first in vivo therapeutic application with anti-Robo4 mAb revealed that Robo4 is a therapeutic target on the tumor endothelial cells. The first and second findings will greatly contribute to the development of antibody therapies based on cell-internalizing antibodies such as ADCs, targeted liposomal drugs, or imaging. The third finding provides a new focus regarding the role of Robo4 biology in the body, such as the decreased side effects associated with depleting Robo4-positive endothelial cells in vivo.

This method allowed us to successfully isolate anti-Robo4 and anti-VEGFR2 cell-internalizing mAbs in combination with a phage antibody library and a PSIF-based screening system. This method provided one-step screening of cell-internalization of hundreds of "monoclonal" candidates. This is the main advantage of the present system over the old screening system, which required handling a "polyclonal" pool of mAbs.[6,7] The innovative feature of our method is the use of PSIF as a fusion partner for antibodies in scFv format, thus facilitating the identification of antibody fragments capable of efficient internalization. The scFv fusion is much easier than the chemical conjugation of the antibody to a cytotoxic drug. In principle, this method can be applied to other phage libraries, such as nonimmune phage antibody libraries[35,45] or synthetic

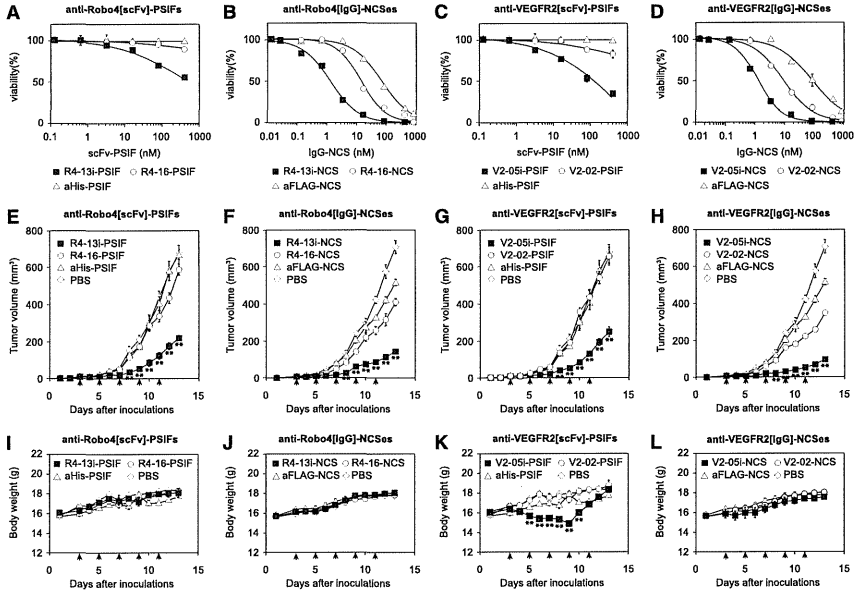

Figure 5. Enhanced anti-tumor effect of cell-internalizing mAbs. (A-D) Cytotoxicity of scFv-PSIF and IgG-NCS against MS1 cells. MS1 cells were incubated with serially diluted mAb-drug conjugates for 24 hours. Cell viability was then measured using a WST-8 assay. Closed square, internalizing mAbs; open circle, low-internalizing mAbs; open triangle, negative controls. (A) anti-Robo4[scFv]-PSIFs, (B) anti-Robo4[IgG]-NCSes, (C) anti-VEGFR2[scFv]-PSIFs, (D) anti-VEGFR2[IgG]-NCSes. Anti-His[scFv]-PSIF and anti-FLAG[IgG]-NCS were used as negative controls. Values are shown as means ± SD. (E-H) Antitumor effects of scFv-PSIFs or IgG-NCSes. B16BL6 cells were inoculated intracutaneously into C57BL6 mice on day 0. On days 3, 5, 7, 9, and 11, mAb-drug conjugates were intravenously administered *(arrow heads)*. Tumor volume was calculated using the following formula: tumor volume (mm^3) = {major axis of tumor (mm)} × {minor axis of tumor (mm)}^{2} × 0.4. Closed square, internalizing mAbs; open circle, low-internalizing mAbs; open triangle, negative controls (anti-His[scFv]-PSIF or anti-FLAG[IgG]-NCS); open diamond, PBS. (E) Anti-Robo4[scFv]-PSIFs, (F) anti-Robo4[IgG]-NCSes, (G) anti-VEGFR2[scFv]-PSIFs, (H) anti-VEGFR2[IgG]-NCSes. Values are shown as means ± SEM. $^{**}P < 0.01$; internalizing mAbs versus low-internalizing mAbs by Bonferroni post hoc analysis with two-way ANOVA (n = 6). (I-L) Change in body weight during therapy experiment. Closed square, internalizing mAbs; open circle, low-internalizing mAbs; open triangle, negative controls (anti-His[scFv]-PSIF or anti-FLAG[IgG]-NCS); open diamond, PBS. (I) anti-Robo4[scFv]-PSIFs, (J) anti-Robo4[IgG]-NCSes, (K) anti-VEGFR2[scFv]-PSIFs, (L) anti-VEGFR2[IgG]-NCSes. Values are shown as means ± SEM. $^{**}P < 0.01$; internalizing mAbs versus PBS by Bonferroni post hoc analysis with two-way ANOVA (n = 6).

human phage antibody libraries,[46,47] which have already been developed. This system can expand the versatility of phage display systems, which will thus contribute to the development of other cell-internalizing antibodies against various types of antigens for effective cancer therapy.

A comparison of cell-internalizing mAbs with low-internalizing mAbs revealed the strength of the cell-internalizing mAbs in terms of the biodistribution and therapeutic effects. Until now, how internalization contributes to the biodistribution of mAbs has been unclear. In this report, we could use a comparative study to clarify this question because we produced both cell-internalizing mAbs and low-internalizing mAbs with similar binding affinities. As a result, more cell-internalizing mAbs than low-internalizing mAbs were significantly accumulated in the tumor. This is the first evidence to support that mAbs with high internalization activity have greater tumor-targeting potency. This information is also useful for other applications that benefit from cell-internalizing mAbs, such as liposomal drugs, bioactive proteins/peptides, and viral vectors.[48,49]

Until now, the usefulness of Robo4-targeted therapy has not been established. Therapy to target VEGF-VEGFR signaling is already common, but the risk of side effects must be addressed.[31-33] Although VEGFR expression is upregulated on tumor vessels, it is also observed on the endothelium in healthy tissues. Previous reports also mentioned the toxicity associated with the anti-VEGFR therapies in mouse models[50] and the clinical trial.[51] Therefore, alternative therapies that target tumor angiogenesis are desired. In the present study, we revealed the possibility that anti-Robo4 ADCs were safer than anti-VEGFR2 ADCs, although they had similar antitumor effects. The findings from immunofluorescence and biodistribution studies also support the notion that anti-Robo4 mAbs could accumulate in the tumor without distributing to normal tissues. This is the first finding of Robo4-targeted therapy and suggests that Robo4 is a potential alternative target for tumor vascular targeting. Of course, additional experiments are needed to establish anti-Robo4 as a novel tool in tumor vascular targeting. For example, the pathological observations of normal blood vessels, in-depth toxicological analysis, or the efficacy against other clinical relevant tumor models, are important for the successful story. Such basic analyses regarding Robo4 might accelerate the development of novel medicines that target tumor angiogenesis, including anti-Robo4 ADCs.

Acknowledgments

This study was supported by Grant-in-Aid for Scientific research (B) and Grant-in-Aid for Scientific Research on Innovative Areas from the Ministry of Education, Culture, Sports, Science, and Technology of Japan and the Japan Society for the Promotion of Science; Strategic Japanese-Swiss Cooperative Program from Japan Science and Technology Agency (JST) and the Swiss Federal Institute of Technology Zurich.

Authorship

Contribution: Y.M. designed the study; M.Y. and Y. Tsumori performed the experiments; Y.M. and M.Y. analyzed the data; Y.M. and M.Y. wrote the initial manuscript; S.T. and Y. Tsutsumi contributed to the phage display; Y.Y. and N.O. contributed to animal experiments; Y.O., W.C.A., and T.D. contributed to Robo4 related analysis; Y.M. and S.N. were responsible for the overall project. All authors edited the manuscript.

Conflict-of-interest disclosure: The authors declare no competing financial interests.

Correspondence: Yohei Mukai and Shinsaku Nakagawa, Laboratory of Biotechnology and Therapeutics, Graduate School of Pharmaceutical Sciences, Osaka University, 1–6 Yamadaoka, Suita, Osaka 565–0871, Japan; e-mail: y-mukai@nibio.go.jp and nakagawa@phs.osaka-u.ac.jp.

References

1. Alley SC, Okeley NM, Senter PD. Antibody-drug conjugates: targeted drug delivery for cancer. *Curr Opin Chem Biol.* 2010;14(4):529-537.
2. Isakoff SJ, Baselga J. Trastuzumab-DM1: building a chemotherapy-free road in the treatment of human epidermal growth factor receptor 2-positive breast cancer. *J Clin Oncol.* 2011;29(4): 351-354.
3. Ansell SM. Brentuximab vedotin: delivering an antimitotic drug to activated lymphoma cells. *Expert Opin Investig Drugs.* 2011;20(1):99-105.
4. Reichert JM. Antibody-based therapeutics to watch in 2011. *MAbs.* 2011;3(1):76-99.
5. Gerber HP, Senter PD, Grewal IS. Antibody drug-conjugates targeting the tumor vasculature: Current and future developments. *MAbs.* 2009; 1(3):247-253.
6. Poul MA, Becerril B, Nielsen UB, et al. Selection of tumor-specific internalizing human antibodies from phage libraries. *J Mol Biol.* 2000;301(5): 1149-1161.
7. An F, Drummond DC, Wilson S, et al. Targeted drug delivery to mesothelioma cells using functionally selected internalizing human single-chain antibodies. *Mol Cancer Ther.* 2008;7(3): 569-578.
8. Mukai Y, Sugita T, Yamato T, et al. Creation of novel Protein Transduction Domain (PTD) mutants by a phage display-based high-throughput screening system. *Biol Pharm Bull.* 2006;29(8):1570-1574.
9. Chaudhary VK, FitzGerald DJ, Adhya S, et al. Activity of a recombinant fusion protein between transforming growth factor type alpha and Pseudomonas toxin. *Proc Natl Acad Sci USA.* 1987;84(13):4538-4542.
10. Kreitman RJ, Wilson WH, Bergeron K, et al. Efficacy of the anti-CD22 recombinant immunotoxin BL22 in chemotherapy-resistant hairy-cell leukemia. *N Engl J Med.* 2001;345(4): 241-247.
11. Pastan I, FitzGerald D. Pseudomonas exotoxin: chimeric toxins. *J Biol Chem.* 1989;264(26): 15157-15160.
12. Legg JA, Herbert JMJ, Clissold P, et al. Slits and Roundabouts in cancer, tumour angiogenesis and endothelial cell migration. *Angiogenesis.* 2008; 11(1):13-21.
13. Huminiecki L, Bicknell R. In silico cloning of novel endothelial-specific genes. *Genome Res.* 2000; 10(11):1796-1806.
14. Huminiecki L, Gorn M, Suchting S, et al. Magic roundabout is a new member of the roundabout receptor family that is endothelial specific and expressed at sites of active angiogenesis. *Genomics.* 2002;79(4):547-552.
15. Smith-Berdan S, Nguyen A, Hassanein D, et al. Robo4 cooperates with CXCR4 to specify hematopoietic stem cell localization to bone marrow niches. *Cell Stem Cell.* 2011;8(1):72-83.
16. Park KW, Morrison CM, Sorensen LK, et al. Robo4 is a vascular-specific receptor that inhibits endothelial migration. *Dev Biol.* 2003;261(1): 251-267.
17. Seth P, Lin Y, Hanai J, et al. Magic roundabout, a tumor endothelial marker: expression and signaling. *Biochem Biophys Res Commun.* 2005; 332(2):533-541.
18. Okada Y, Yano K, Jin E, et al. A three-kilobase fragment of the human Robo4 promoter directs cell type-specific expression in endothelium. *Circ Res.* 2007;100(12):1712-1722.
19. Okada Y, Jin E, Nikolova-Krstevski V, et al. A GABP-binding element in the Robo4 promoter is necessary for endothelial expression in vivo. *Blood.* 2008;112(6):2336-2339.
20. Jones CA, London NR, Chen H, et al. Robo4 stabilizes the vascular network by inhibiting pathologic angiogenesis and endothelial hyperpermeability. *Nat Med.* 2008;14(4):448-453.
21. Jones CA, Nishiya N, London NR, et al. Slit2-Robo4 signalling promotes vascular stability by blocking Arf6 activity. *Nat Cell Biol.* 2009; 11(11):1325-1331.
22. Marlow R, Binnewies M, Sorensen LK, et al. Vascular Robo4 restricts proangiogenic VEGF signaling in breast. *Proc Natl Acad Sci USA.* 2010;107(23):10520-10525.
23. Koch AW, Mathivet T, Larrivée B, et al. Robo4 maintains vessel integrity and inhibits angiogenesis by interacting with UNC5B. *Dev Cell.* 2011;20(1):33-46.
24. Kerbel RS. Tumor angiogenesis. *N Engl J Med.* 2008;358(19):2039-2049.
25. Paleolog EM. Angiogenesis in rheumatoid arthritis. *Arthritis Res.* 2002;4(Suppl 3):S81-S90.
26. Tonnesen MG, Feng X, Clark RA. Angiogenesis in wound healing. *J Investig Dermatol Symp Proc.* 2000;5(1):40-46.
27. Olsson AK, Dimberg A, Kreuger J, et al. VEGF receptor signalling - in control of vascular function. *Nat Rev Mol Cell Biol.* 2006;7(5):359-371.
28. Crawford Y, Ferrara N. VEGF inhibition: insights from preclinical and clinical studies. *Cell Tissue Res.* 2009;335(1):261-269.
29. Wicki A, Rochlitz C, Orleth A, et al. Targeting tumor-associated endothelial cells: anti-VEGFR2 immunoliposomes mediate tumor vessel disruption and inhibit tumor growth. *Clin Cancer Res.* 2012;18(2):454-464.
30. Witmer AN, Dai J, Weich HA, et al. Expression of vascular endothelial growth factor receptors 1, 2, and 3 in quiescent endothelia. *J Histochem Cytochem.* 2002;50(6):767-777.
31. Kamba T, McDonald DM. Mechanisms of adverse effects of anti-VEGF therapy for cancer. *Br J Cancer.* 2007;96(12):1788-1795.
32. Eremina V, Jefferson JA, Kowalewska J, et al. VEGF inhibition and renal thrombotic microangiopathy. *N Engl J Med.* 2008;358(11):1129-1136.
33. Choueiri TK, Mayer EL, Je Y, et al. Congestive heart failure risk in patients with breast cancer treated with bevacizumab. *J Clin Oncol.* 2011; 29(6):632-638.
34. Yoshikawa M, Mukai Y, Okada Y, et al. Ligand-independent assembly of purified soluble magic roundabout (Robo4), a tumor-specific endothelial marker. *Protein Expr Purif.* 2008;61(1):78-82.
35. Imai S, Mukai Y, Nagano K, et al. Quality enhancement of the non-immune phage scFv library to isolate effective antibodies. *Biol Pharm Bull.* 2006;29(7):1325-1330.
36. Yoshikawa M, Mukai Y, Tsunoda S, et al. Modifying the antigen-immunization schedule improves the variety of monoclonal antibodies obtained from immune-phage antibody libraries against HIV-1 Nef and Vif. *J Biosci Bioeng.* 2011; 111(5):597-599.
37. Yamamoto Y, Tsutsumi Y, Yoshioka Y, et al. Site-specific PEGylation of a lysine-deficient TNF-alpha with full bioactivity. *Nat Biotechnol.* 2003;21(5):546-552.
38. Hunter WM, Greenwood FC. Preparation of iodine-131 labelled human growth hormone of high specific activity. *Nature.* 1962;194:495-496.
39. Mellman I. Endocytosis and molecular sorting. *Annu Rev Cell Dev Biol.* 1996;12:575-625.
40. Holliger P, Hudson PJ. Engineered antibody fragments and the rise of single domains. *Nat Biotechnol.* 2005;23(9):1126-1136.
41. Pavlinkova G, Beresford GW, Booth BJ, et al. Pharmacokinetics and biodistribution of engineered single-chain antibody constructs of MAb CC49 in colon carcinoma xenografts. *J Nucl Med.* 1999;40(9):1536-1546.
42. Schneider DW, Heitner T, Alicke B, et al. In vivo biodistribution, PET imaging, and tumor accumulation of 86Y- and 111In-antimindir/RG-1,

engineered antibody fragments in LNCaP tumor-bearing nude mice. *J Nucl Med.* 2009; 50(3):435-443.

43. Maeda H. SMANCS and polymer-conjugated macromolecular drugs: advantages in cancer chemotherapy. *Adv Drug Deliv Rev.* 2001;46(1-3): 169-185.
44. Kappen LS, Goldberg IH. Activation and inactivation of neocarzinostatin-induced cleavage of DNA. *Nucleic Acids Res.* 1978; 5(8):2959-2967.
45. Okamoto T, Mukai Y, Yoshioka Y, et al. Optimal construction of non-immune scFv phage display libraries from mouse bone marrow and spleen established to select specific scFvs efficiently binding to antigen. *Biochem Biophys Res Commun.* 2004;323(2): 583-591.
46. Silacci M, Brack S, Schirru G, et al. Design, construction, and characterization of a large synthetic human antibody phage display library. *Proteomics.* 2005;5(9): 2340-2350.
47. Villa A, Lovato V, Bujak E, et al. A novel synthetic naïve human antibody library allows the isolation of antibodies against a new epitope of oncofetal fibronectin. *MAbs.* 2011; 3(3):264-272.
48. Sapra P, Allen TM. Internalizing antibodies are necessary for improved therapeutic efficacy of antibody-targeted liposomal drugs. *Cancer Res.* 2002;62(24):7190-7194.
49. Pastan I, Hassan R, Fitzgerald DJ, et al. Immunotoxin therapy of cancer. *Nat Rev Cancer.* 2006;6(7):559-565.
50. Chinnasamy D, Yu Z, Theoret MR, et al. Gene therapy using genetically modified lymphocytes targeting VEGFR-2 inhibits the growth of vascularized syngenic tumors in mice. *J Clin Invest.* 2010;120(11):3953-3968.
51. Nagayama H, Matsumoto K, Isoo N, et al. Gastrointestinal bleeding during anti-angiogenic peptide vaccination in combination with gemcitabine for advanced pancreatic cancer. *Clin J Gastroenterol.* 2010;3(6):307-317.

Cytokine 61 (2013) 578–584

Contents lists available at SciVerse ScienceDirect

Cytokine

journal homepage: www.journals.elsevier.com/cytokine

Mutants of lymphotoxin-α with augmented cytotoxic activity *via* TNFR1 for use in cancer therapy

Tomohiro Morishige [a,1], Yasuo Yoshioka [b,c,*,1], Shogo Narimatsu [a], Shinji Ikemizu [d], Shin-ichi Tsunoda [c,e], Yasuo Tsutsumi [b,c,e], Yohei Mukai [a], Naoki Okada [a], Shinsaku Nakagawa [a,c,*]

[a] *Laboratory of Biotechnology and Therapeutics, Graduate School of Pharmaceutical Sciences, Osaka University, 1-6 Yamadaoka, Suita, Osaka 565-0871, Japan*
[b] *Laboratory of Toxicology and Safety Science, Graduate School of Pharmaceutical Sciences, Osaka University, 1-6 Yamadaoka, Suita, Osaka 565-0871, Japan*
[c] *The Center for Advanced Medical Engineering and Informatics, Osaka University, 1-6 Yamadaoka, Suita, Osaka 565-0871, Japan*
[d] *Graduate School of Pharmaceutical Sciences, Kumamoto University, 5-1 Oe-honmachi, Kumamoto 862-0973, Japan*
[e] *Laboratory of Biopharmaceutical Research, National Institute of Biomedical Innovation, 7-6-8 Saito-Asagi, Ibaraki, Osaka 567-0085, Japan*

ARTICLE INFO

Article history:
Received 6 July 2012
Received in revised form 29 September 2012
Accepted 6 November 2012
Available online 11 December 2012

Keywords:
Affinity
Apoptosis
Bioactivity
Cytokine
Cytotoxicity

ABSTRACT

The cytokine lymphotoxin-α (LTα) is a promising candidate for use in cancer therapy. However, the instability of LTα *in vivo* and the insufficient levels of tumor necrosis factor receptor 1 (TNFR1)-mediated bioactivity of LTα limit its therapeutic potential. Here, we created LTα mutants with increased TNFR1-mediated bioactivity by using a phage display technique. We constructed a phage library displaying lysine-deficient structural variants of LTα with randomized amino acid residues. After affinity panning, we screened three clones of lysine-deficient LTα mutant, and identified a LTα mutant with TNFR1-mediated bioactivity that was 32 times that of the wild-type LTα (wtLTα). When compared with wtLTα, the selected clone showed augmented affinity to TNFR1 due to slow dissociation rather than rapid association. In contrast, the mutant showed only 4 times the TNFR2-mediated activity of wtLTα. In addition, the LTα mutant strongly and rapidly activated caspases that induce TNFR1-mediated cell death, whereas the mutant and wtLTα activated nuclear factor-kappa B to a similar extent. Our data suggest that the kinetics of LTα binding to TNFR1 play an important role in signal transduction patterns, and a TNFR1-selective LTα mutant with augmented bioactivity would be a superior candidate for cancer therapy.

1. Introduction

Lymphotoxin-alpha (LTα) is a tumor necrosis factor (TNF) superfamily cytokine with tumor-cell-specific cytotoxic activity and immune-activating activity. LTα induces the expression of chemokines and adhesion molecules in endothelial cells, and plays a key role in lymph node neogenesis [1–3]. Schrama et al. [4,5] showed that systemic administration of LTα to a tumor-bearing mouse leads to the construction of ectopic lymphoid tissue within the tumor and the strong induction of tumor immunity in that lymphoid tissue, suggesting that the underlying mechanism of this cytokine's anti-tumor activity may be effective. Therefore, LTα has long been considered to be a promising candidate for an anti-cancer agent. However, the clinical use of LTα has been limited because of the protein's *in vivo* instability and proinflammatory side effects.

One of the most common ways to improve the therapeutic effects of proteins is to conjugate them with polyethylene glycol (PEG) in a process called PEGylation, or to conjugate them with other water-soluble polymers [6]. Because of the steric hindrance caused by the PEG molecule, PEGylation can prolong the plasma half-life of molecules and alter the tissue distribution of the conjugates compared with those of the native form. PEGylation of proteins is mostly nonspecific because it targets all of the lysine residues in the protein, some of which may be in or near an active site. As a result, PEGylation significantly reduces the specific

Abbreviations: E. coli, Escherichia coli; ELISA, enzyme-linked immunosorbent assay; FADD, Fas-associated protein with death domain; FBS, fetal bovine serum; HVEM, herpes virus entry mediator; IFNγ, interferon γ; LTα, lymphotoxin-alpha; NFκB, nuclear factor-kappa B; PEG, polyethylene glycol; pI, isoelectric points; SDS-PAGE, sodium dodecyl sulfate–polyacrylamidegel electrophoresis; SPR, surface plasmon resonance; TNF, tumor necrosis factor; TNFR1, TNF receptor 1; TRADD, *TNF receptor-associated death domain*; TRAF, *TNF receptor-associated factor*; wtLTα, wild-type LTα.

* Corresponding authors. Addresses: Laboratory of Toxicology and Safety Science, Graduate School of Pharmaceutical Sciences, Osaka University, 1-6 Yamadaoka, Suita, Osaka 565-0871, Japan. Tel./fax: +81 6 6879 8233 (Y. Yoshioka), Laboratory of Biotechnology and Therapeutics, Graduate School of Pharmaceutical Sciences, Osaka University, 1-6 Yamadaoka, Suita, Osaka 565-0871, Japan. Tel.: +81 6 6879 8175; fax: +81 6 6879 8179 (S. Nakagawa).
E-mail addresses: yasuo@phs.osaka-u.ac.jp (Y. Yoshiokab), nakagawa@phs.osaka-u.ac.jp (S. Nakagawa).
[1] These authors contributed equally to the work.

1043-4666/$ - see front matter © 2012 Elsevier Ltd. All rights reserved.
http://dx.doi.org/10.1016/j.cyto.2012.11.005

activity of the proteins involved. Our group previously developed a novel strategy for site-specific mono-PEGylation of lysine-deficient mutants to overcome these limitations of PEGylation [7,8]. We demonstrated that site-specific PEGylation of a lysine-deficient mutant of LTα retained higher bioactivity compared with random PEGylation of wild-type LTα (wtLTα) [9]. This finding suggests that site-specific PEGylation of a lysine-deficient mutant of LTα might be a useful way to overcome the problems in the clinical use of LTα outlined above.

LTα binds to three receptor subtypes—TNF receptor 1 (TNFR1), TNFR2, and herpes virus entry mediator (HVEM)—to exert various biological functions. TNFR1 induces an anti-tumor effect and Peyer's patch development, whereas TNFR2 is essential for immune responses against bacteria and viruses [1]. Human LTα and TNF that bind to murine TNFR1, but not to murine TNFR2, are not lethal in healthy mice except at extremely high doses, suggesting that LTα and TNF α exhibit their lethal side effects *via* TNFR2 [10,11]. Therefore, LTα as a cancer immunotherapeutic agent, a LTα mutant with selectively increased TNFR1-mediated bioactivity is needed. Previously, we successfully created a TNFR1-selective LTα mutant whose bioactivity *via* TNFR1 was several times that of wtLTα, and whose bioactivity *via* TNFR2 was 2.5% that of wtLTα [12]. However, to enhance therapeutic efficacy and suppress the side effect of LTα, it is necessary to create a LTα mutant with greatly increased TNFR1-mediated bioactivity and TNFR1-selectivity.

In this study, we attempted to create LTα mutants with selectively increased TNFR1-mediated bioactivity by using a phage display technique. We succeeded in creating a LTα mutant that had a much higher bioactivity *via* TNFR1 and an augmented affinity to TNFR1 compared with that of wtLTα, and demonstrated that this was due to the slow dissociation rate of the LTα mutant-TNFR1 complex. In addition, we showed that the LTα mutant differed from wtLTα by its ability to strongly and rapidly activate caspases. In contrast, the LTα mutant and wtLTα were similar to each other in their degree of activation of nuclear factor-kappa B (NFκB). Our findings suggest that this LTα mutant would be a superior candidate for a cancer immunotherapeutic agent.

2. Materials and methods

2.1. Cells

HEp-2 cells, a human carcinoma cell line derived via HeLa contamination, were purchased from the American Type Culture Collection (Manassas, VA), and cultured in RPMI 1640 medium (Wako Pure Chemical Industries, Osaka, Japan) supplemented with 10% fetal bovine serum (FBS), 1 mM sodium pyruvate, 50 μM 2-mercaptoethanol, and antibiotics. HT29.14S cells, a TNF/LT-sensitive subclone of HT29 human colon adenocarcinoma, were kindly provided by Dr. Carl Ware (La Jolla Institute for Allergy and Immunology, CA) [13]. HT29.14S cells were cultured in Dulbecco's Modified Eagle's Medium (Wako Pure Chemical Industries) supplemented with 10% FBS, 10 mM HEPES, and antibiotics. hTNFR2/mFas-PA cells are preadipocytes derived from TNFR1$^{-/-}$ TNFR2$^{-/-}$ mice expressing a chimeric receptor composed of the extracellular and transmembrane domain of human TNFR2 and the intracellular domain of mouse Fas, which is a member of the TNF receptor superfamily [14]; these cells were cultured in RPMI 1640 medium supplemented with 10% FBS, 5 μg/mL Blasticidin S HCl (Invitrogen, Carlsbad, CA), and antibiotics. MCF-7 cells were provided from the Institute of Development, Aging and Cancer, Tohoku University, and were cultured in Eagle's Minimum Essential Medium (Wako Pure Chemical Industries) supplemented with 10% FBS, 0.01 mg/mL bovine insulin, and antibiotics.

2.2. Construction of a library of lysine-deficient mutants of LTα

The phagemid vector pY03′, which encodes human wtLTα with the C-terminus of wtLTα fused to the N-terminus of the M13 phage g3p, was used as a PCR template for constructing a DNA library of lysine-deficient mutants of LTα. We performed a two-step PCR amplification using oligonucleotides containing the sequence NNS (where N represents A, C, G, or T; and S represents C or G) at Lys19, Lys28, Lys39, Lys84, Lys89, and Lys119 of wtLTα; the sequence NNS encodes all 20 standard amino acids. The products from the second PCR were digested with *Nco*I and *Pst*I and then ligated into pY03′. The phagemid was electroporated into *Escherichia coli* (*E. coli*) TG1 cells (Stratagene, Cedar Creek, TX), yielding 2×10^6 independent clones. The phage library displaying lysine-deficient LTα molecules was prepared as described previously [12]. Briefly, pY03′-transformed TG1 cells were infected with M13KO7 helper phage (Invitrogen) and cultured for 6 h at 25 °C. The resultant phage particles were precipitated from the culture supernatant by using PEG (MP Biomedicals, Solon, OH) and suspended in NTE (100 mM NaCl, 10 mM Tris, 1 mM EDTA).

2.3. Selection of bioactive LTα mutants

Screening for bioactive LTα mutants was performed as described previously [12]. Briefly, an immunoplate was coated with soluble human TNFR1 (R&D Systems, Minneapolis, MN), and the prepared phage library was allowed to bind to the immobilized TNFR1. After a second round of panning, single colonies were picked and cultured. The resulting phage-containing culture supernatant was used for screening by enzyme-linked immunosorbent assay (ELISA) against human TNFR1.

2.4. Expression and purification of recombinant LTαs

pET15b plasmids (Novagen, Darmstadt, Germany) encoding LTαs were prepared and used to transform *E. coli* BL21(DE3) cells (Stratagene) for the expression of recombinant protein, as described previously [12]. Expression was induced by adding 1 mM isopropyl β-D-1-thiogalactopyranoside and incubating the cells at 37 °C for 6 h in Terrific Broth (Invitrogen Corporation, Carlsbad, CA) containing 0.4% glucose, 1.68 mM $MgSO_4$, and 100 μg/mL of ampicillin; all products were accumulated as inclusion bodies. The resultant inclusion bodies were washed, solubilized, reduced, and refolded by the methods previously described [12]. After dialysis against a buffer containing 20 mM Tris–HCl (pH 7.4) and 100 mM urea, active trimeric LTα proteins were purified by using a HiLoad Superdex 200PG column (GE Healthcare, UK) equilibrated with phosphate-buffered saline (pH 7.4) followed by ion-exchange chromatography (SP Sepharose Fast Flow for wtLTα; Q Sepharose Fast Flow for mutants of LTα); both columns were obtained from GE Healthcare. To create point mutants, we used pET15b-human wtLTα as a template with a KOD-plus mutagenesis kit (Toyobo, Osaka, Japan) according to the manufacturer's instructions. Recombinant point mutants were produced and purified as described earlier; SP Sepharose Fast Flow was used as the ion-exchange column. Protein concentration was measured by using Coomassie Protein Assay Reagent (Thermo Fisher Scientific, Rockford, IL). Sodium dodecyl sulfate–polyacrylamidegel electrophoresis (SDS–PAGE) analysis of LTαs was conducted under reducing conditions, and the proteins in the gels were stained with Coomassie brilliant blue. The electrostatic potential surface was generated by using GRASP software [15]. The electrostatic potential ranged from −7.5 kT to 7.5 kT. The relative accessible surface areas were calculated by using JOY software [16].

2.5. Cytotoxicity assays

HEp-2 cells were seeded at 4×10^4 cells per well in 96-well plates and incubated for 18 h with serially-diluted LTαs in the presence of 50 μg/mL cycloheximide. For the functional blocking assay, HEp-2 cells were treated with serially-diluted MAB225 (R&D Systems), an anti-TNFR1 antibody, for 30 min. The cells were then incubated with 100 ng/mL wtLTα and LTα mutants for 18 h in the presence of 50 μg/mL cycloheximide. For the caspase inhibition assay, HEp-2 cells were incubated with serially-diluted wtLTα or LTα mutants in the presence of 50 μg/mL cycloheximide and 50 mM zVAD-fmk (Calbiochem, Darmstadt, Germany) for 18 h. R2/Fas preadipocyte cells were seeded at 1.5×10^4 cells per well in 96-well plates and incubated for 48 h with serially-diluted LTαs in the presence of 50 μg/mL cycloheximide. The cytotoxicities of LTαs against HEp-2 cells and R2/Fas preadipocyte cells were assessed by using the standard methylene blue assay method as previously described [12]. HT29.14S and MCF-7 cells were seeded at 5×10^3 cells per well and incubated with LTαs in the presence of 80 U/mL human Interferon γ (IFNγ) (R&D Systems) for 72 h. After incubation, cell viability was measured by using a WST-8 assay kit (Nacalai Tesque, Kyoto, Japan) according to the manufacturer's instructions. The ratio of TNFR1-/TNFR2-mediated bioactivity was calculated as follows: activity of LTαs in HEp-2 cells/activity of LTαs in R2/Fas preadipocyte cells. The TNFR1/TNFR2 ratio for wtLTα was set equal to 1.

2.6. Analysis of binding kinetics by surface plasmon resonance

The binding kinetics of LTαs were analyzed and compared by using a surface plasmon resonance (SPR) method (BIAcore 2000, GE Healthcare, UK). Human TNFR1, TNFR2, or HVEM Fc chimera (R&D Systems, Inc.) was diluted to 50 μg/mL in 10 mM sodium acetate (pH 4.5) and immobilized onto a CM5 sensor chip by using an amine coupling kit (GE Healthcare, UK) as described previously [12]. During the association phase, wtLTα or LTα mutants diluted in HBS-EP running buffer (GE, Healthcare UK) to 37, 18.5, 9.3, 4.6, or 2.3 nM were passed over the immobilized TNFRs for 2 min at a flow rate 20 μL/min. During the dissociation phase, HBS-EP was run over the sensor chip for 1 min at a flow rate 20 μ L/min. Complexes were eluted by using 20 μL of 10 mM glycine–HCl (pH 2.0). Data were evaluated by using BIAevaluation 4.1 software (GE Healthcare UK) to apply a 1:1 Langmuir binding model. The obtained sensorgrams were fitted globally over the range of injected concentrations and simultaneously over the association and dissociation phases.

2.7. Evaluation of caspase-3/7 and -8 activities

HEp-2 cells were seeded at 4×10^4 cells per well in 96-well plates and then incubated for 6, 12, or 18 h with 10 ng/mL of the relevant LTα in the presence of 50 μg/mL cycloheximide. Activities of intracellular caspase-8 and caspase-3/7 were measured by using Caspase-Glo assays (Promega, Madison, WI) according to the manufacturer's instructions.

2.8. Evaluation of NFκB activities

HEp-2 cells were co-transfected with pGL4.32, a NFκB-responsive firefly luciferase expression vector, and pRL-TK, a thymidine kinase–regulated renilla luciferase expression vector (Promega) at a ratio of 90:1 for 18 h. The cells were then treated with 10 ng/mL of wtLTα or LTα mutants for 1, 2, 4, 6, 12, and 24 h. Expression levels of intracellular firefly luciferase and renilla luciferase were then measured by using the Dual-Luciferase Reporter Assay System (Promega). The expression level of firefly luciferase was normalized against that of renilla luciferase.

3. Results

3.1. Production of a highly bioactive LTα mutant

Our recent study showed that site-specific PEGylation of a lysine-deficient mutant of LTα might be useful for cancer therapy, because the mutant retained bioactivity after PEGylation [9]. Here, we attempted to create a lysine-deficient mutant of LTα with augmented bioactivity *via* TNFR1 and TNFR1-selective bioactivity that could be used for site-specific PEGylation in the future. A phage library displaying LTα mutants with randomized sequences in place of all lysine codons was prepared. For the construction of the phage library, two-step PCR was used to replace the lysine codons randomly with an NNS sequence. As a result, we successfully constructed a library with 2×10^6 independent clones, and performed two rounds of panning against immobilized human TNFR1; phage clones were screened for binding affinity to TNFR1 by conducting an ELISA (data not shown). We obtained three LTα mutants (mutLT1, mutLT2, and mutLT3), which were putative lysine-deficient mutants of LTα. DNA sequencing analysis of the LTα mutants confirmed that all 6 lysine residues present in wtLTα were mutated to other amino acids (Table 1). To investigate the properties of the LTα mutants in detail, we prepared recombinant LTα mutant proteins by using an *E. coli* expression system, as previously described [12]. LTα mutants and wtLTα were expressed in *E. coli* and obtained through refolding of inclusion bodies. Purified LTα mutants displayed a molecular mass of 18 kDa by SDS–PAGE analysis (Fig. 1A), and a molecular mass of approximately 60 kDa by size exclusion chromatography (Fig. 1B), indicating that LTα mutants form homotrimeric complexes, as does wtLTα. The isoelectric points (pI) of mutLT1, mutLT2, and mutLT3 were 6.16, 6.16, and 6.00, respectively whereas that of wtLTα was 8.94 (Table 1). We also visually assessed the changes in the surface electrostatic potential values by using GRASP software (Fig. 1C). Because of their lack of lysine residues, LTα mutants had more negative areas on their surface than did wtLTα.

3.2. Bioactivities of LTα mutants

To assess the TNFR1-mediated bioactivity of LTα mutants, cytotoxicity assays using HEp-2 cells were performed (Fig. 2A). wtLTα and LTα mutants showed dose-dependent cytotoxicity, and the bioactivity of each LTα mutant was higher than that of wtLTα in the HEp-2 cells (Fig. 2A). The bioactivity of mutLT1 was especially high (31.8 times that of wtLTα; Table 2). Furthermore, we confirmed that the LTα-induced cytotoxicity was blocked by the anti-TNFR1 antibody in all cases (Fig. 2B). These results indicate that the LTα mutants possess higher TNFR1-mediated bioactivity than that displayed by wtLTα. To confirm that the higher bioactivity of the LTα mutants was not specific to HEp-2 cells, we examined the bio-

Table 1
Amino acid sequences and the isoelectric points of LTα mutants. The pI values of LTαs were calculated by using a program in the Expert Protein Analysis System proteomics server of the Swiss Institute of Bioinformatics (Basel, Switzerland).

	Residue position						pI
	19	28	39	84	89	119	
wtLTα	Lys	Lys	Lys	Lys	Lys	Lys	8.94
mutLT1	Asn	Gln	Asn	Ser	Leu	Gly	6.16
mutLT2	Asn	Gln	Ser	Thr	Val	Val	6.16
mutLT3	Asp	Gln	Ala	Thr	Thr	Ala	6.00

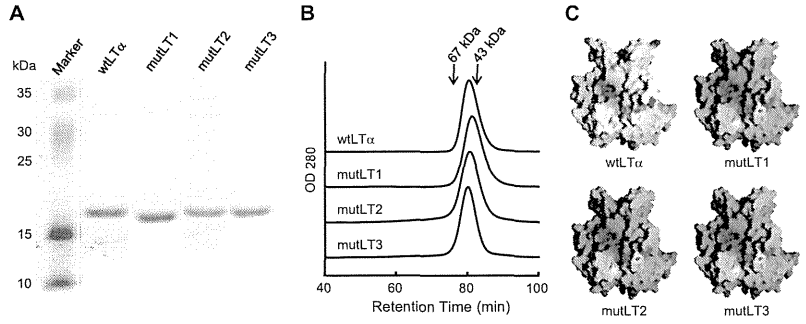

Fig. 1. Properties of recombinant LTα mutants. (A) SDS–PAGE analysis of wtLTα and LTα mutants. All products were separated on an SDS–PAGE gel and visualized by means of Coomassie Brilliant Blue staining. Marker indicates molecular weight standards. (B) Chromatograms of purified wtLTα and LTα mutants. wtLTα or LTα mutants were loaded onto a size-exclusion column and eluted at 1.0 mL/min. (C) The electrostatic potential surface was generated by using GRASP software. Red and blue indicate negative and positive electrostatic potentials, respectively. The electrostatic potential ranged from −7.5 kT (bright blue) to 7.5 kT (bright red). The relative accessible surface areas were calculated by using JOY software.

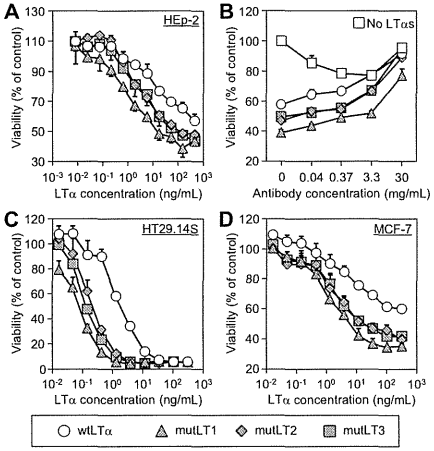

Fig. 2. TNFR1-mediated cytotoxic activity of wtLTα and LTα mutants. (A) HEp-2 cells were incubated with wtLTα or LTα mutants in the presence of cycloheximide. After 18 h incubation, cell viability was assessed by methylene blue assay. (B) HEp-2 cells were treated with serially-diluted MAB225, an anti-TNFR1 neutralizing antibody, for 30 min. The cells were then incubated with 100 ng/mL wtLTα or LTα mutants in the presence of cycloheximide. After 18 h incubation, the cell viability was assessed by methylene blue assay. (C) HT29.14S cells and (D) MCF-7 cells were incubated with wtLTα or LTα mutants in the presence of IFNγ. After 72 h incubation, the cell viability was assessed by WST-8 assay. EC30 and EC50 are the concentrations of LTα required for 30% and 50% inhibition of cell viability, respectively. Each value represents the mean ± SD ($n \approx 4$).

activities of mutLTαs in two other cell types (Fig. 2C and D, Table 2). When compared with wtLTα, the LTα mutants exhibited 8–24 times the cytotoxicity in HT29.14S cells, and 16–34 times the cytotoxicity in MCF-7 cells (Fig. 2C and D, Table 2). To specifically evaluate the TNFR2-mediated bioactivity of the LTα mutants, we examined the levels of cytotoxicity induced by LTα mutants in hTNFR2/mFas-PA cells. These cells have been engineered to exhibit hTNFR2- but not hTNFR1-mediated activities [14]. The human TNFR2-mediated bioactivities of LTα mutants were 2.2–4.1 times those of wtLTα in hTNFR2/mFas-PA cells (Fig. 3). The calculated ratios of TNFR1-mediated bioactivity by using HEp-2 cells/TNFR2-mediated bioactivity induced by mutLT1, mutLT2, and mutLT3 were 7.8, 3.2, and 1.9 times that of wtLTα, respectively. This result suggests that LTα mutants, especially mutLT1, have selectivity for TNFR1 in addition to their augmented bioactivity.

Next, to measure the binding affinity of LTα mutants to TNFRs, we performed an SPR analysis by using a BIAcore 2000 biosensor (Table 3). The binding affinities of mutLT1, mutLT2 and mutLT3 to TNFR1 were 2.7, 2.0, and 1.4 times those of wtLTα, respectively. We considered that the increased affinity of LTα mutant for TNFR1 might be related to the enhanced bioactivity through this receptor. In particular, k_{off} values for LTα mutants binding to TNFR1 were 39–57% of the value for wtLTα, whereas the k_{on} values for LTα mutants binding to TNFR1 were almost the same as that for wtLTα. These results suggest that TNFR1 interacts more strongly with the LTα mutants than wtLTα due to slow dissociation kinetics, and that this binding mode between LTα mutant and TNFR1 induces a potent signaling pathway. We then evaluated the affinity of the LTα mutants for TNFR2 by using SPR methodology (Table 4). The affinity of TNFR2 for LTα mutants was 1.5–2.1 times that for wtLTα due to fast association kinetics. Taken together, these results indicate that the binding modes of LTα mutants to TNFR1 and TNFR2 might dictate their bioactivity.

We previously demonstrated that Lys84 in LTα plays a crucial role in the protein's interaction with the main chain of TNFR1 [12]. Therefore, to investigate the importance of the amino acid sequence at position 84, we created LTα mutants with Lys84 replaced by Ser84 (K84S), Thr84 (K84T), or Ala84 (K84A), and evaluated their binding kinetics and bioactivities *via* TNFR1. We found that these point mutants exhibited a slower dissociation rate and increased bioactivity *via* TNFR1 when compared with wtLTα. K84S showed especially high bioactivity even though its affinity for TNFR1 was lower than that of wtLTα (Table 5).

3.3. Activation of caspases by LTα mutant

It is known that TNFR1-mediated cell death is regulated by the activities of caspases including caspase-3, -7, and -8 [17].

Table 2
The TNFR1-mediated bioactivities of wtLTα and LTα mutants. EC30 and EC50 were calculated from the cytotoxic activity of wtLTα and LTα mutants against HEp-2, HT29.14S and MCF-7 cells. Relative activity values were calculated as EC30 (wtLTα)/EC30 (LTα mutant) or EC50 (wtLTα)/EC50 (LTα mutant).

	HEp-2 cells		HT29.14S cells		MCF-7 cells	
	EC30 (ng/mL)	Relative activity	EC50 (ng/mL)	Relative activity	EC50 (ng/mL)	Relative activity
wtLTα	47.7	1.0	1.80	1.0	36.7	1.0
mutLT1	1.5	31.8	0.08	23.6	1.1	33.7
mutLT2	6.8	7.0	0.21	8.5	2.3	16.0
mutLT3	7.8	6.1	0.13	14.2	2.3	16.0

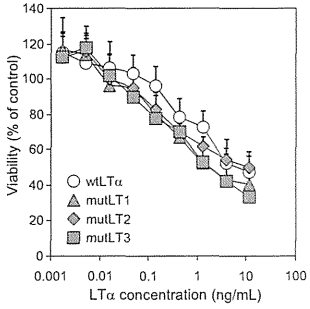

	EC30 (ng/mL)	Relative activity (% vs wtLTα)
wtLTα	1.39	100
mutLT1	0.34	409
mutLT2	0.64	217
mutLT3	0.43	323

Fig. 3. TNFR2-mediated cytotoxic activities of wtLTα and LTα mutants. hTNFR2/mFas-PA cells were incubated with serial dilutions of wtLTα or LTα mutants in the presence of cycloheximide. After 48 h incubation, cell viability was assessed by methylene blue assay. EC30 is the concentration of LTα required for 30% inhibition of cell viability. Each value represents the mean ± SD ($n = 4$).

Table 3
The binding kinetics of interactions between LTα mutants and hTNFR1 analyzed by using an SPR biosensor. k_{on} is the association kinetic constant; k_{off} is the dissociation kinetic constant; and K_D is the equilibrium dissociation constant. Relative affinity values were calculated as 100 × K_D (wtLTα)/K_D (LTα mutant).

	k_{on} (10^6/M s)	k_{off} (10^{-4}/s)	K_D (10^{-10}/M)	Relative affinity (% vs wtLTα)
wtLTα	1.2	6.1	4.9	100
mutLT1	1.3	2.4	1.8	269
mutLT2	1.4	3.5	2.5	195
mutLT3	0.97	3.4	3.4	143

Therefore, to examine the mechanism behind the augmentation of TNFR1-mediated bioactivity, we investigated the association between caspase activity and LTα mutant-induced cell death. First, we treated cells with LTα mutants in the presence of a broad caspase inhibitor, zVAD-fmk, and analyzed the cell viability (Fig. 4A). The results showed that zVAD-fmk almost completely abrogated the cytotoxicity induced by wtLTα and LTα mutants. These results indicate that both wild-type and LTα mutant-induced cell death were dependent on the activation of caspase. We then examined the activity of caspase-3/7 (Fig. 4B) and -8 (Fig. 4C) induced by LTα mutants in HEp-2 cells. LTα mutants, especially

Table 4
Binding kinetics of interactions between LTα mutants and hTNFR2 were analyzed by using an SPR biosensor. k_{on} is the association kinetic constant; k_{off} is the dissociation kinetic constant; and K_D is the equilibrium dissociation constant. Relative affinity values were calculated as 100 × K_D (wtLTα)/K_D (LTα mutant).

	k_{on} (10^6/M s)	k_{off} (10^{-4}/s)	K_D (10^{-10}/M)	Relative affinity (% vs wtLTα)
wtLTα	2.8	23.5	8.3	100
mutLT1	4.7	25.0	5.4	154
mutLT2	6.2	24.0	3.9	213
mutLT3	4.5	25.3	5.6	148

mutLT1, which has the highest bioactivity, quickly and strongly induced the activation of caspases. These results suggest that stabilization of the LTα -TNFR1 complex by the presence of LTα mutant contributed to increased caspase activity, which in turn induced cytotoxic effects.

3.4. Activation of NFκB by LTα mutants

It is well known that TNFR1 activates NFκB signaling pathway in addition to the caspase cascade [18,19]. Therefore, to investigate whether the LTα mutants activate NFκB, we assessed the association between NFκB activity and LTα mutant-induced cell death. First, we prepared cells transfected with luciferase expressing vector activated by NFκB. Then, we treated cells with LTα mutants and analyzed the NFκB activity by measuring the expression level of luciferase (Fig. 5). Despite the higher TNFR1-mediated bioactivity of LTα mutants, we found that NFκB activity was induced to a similar extent by LTα mutants and wtLTα. This finding indicates that the LTα mutants selectively activate the caspase cascade but not NFκB activation *via* TNFR1.

4. Discussion

When constructing a LTα mutant as an anti-cancer agent, it is important that the mutant exhibits TNFR1 selectivity because of the lethal side-effects of TNFR2-mediated bioactivity. We previously created a LTα mutant (R1selLT), which had only 2.5% of the TNFR2-mediated bioactivity of wtLTα and 3.5 times of the TNFR1-mediated bioactivity of wtLTα [12]. The ratio of TNFR1/TNFR2 bioactivity of R1selLT was 145.8 times that of wtLTα. In addition to TNFR1 selectivity, augmentation of TNFR1-mediated bioactivity is also highly desirable in a therapeutic agent for cancer. Here, we created three lysine-deficient LTα mutants with greatly increased levels of TNFR1-mediated bioactivity through an altered binding mode. These mutants showed preferentially augmented bioactivity *via* TNFR1 compared with TNFR2. The TNFR1 selectivity of mutLT1, 2, and 3 was 7.8, 3.2, and 1.9 times that of wtLTα, respectively. Although the TNFR1 selectivity was lower for mutLT1 than for R1selLT, the TNFR1-mediated bioactivity of mutLT1 was 31.8 times that of wtLTα compared to 3.5 times of R1selLT. Such extreme augmentation of bioactivity is rarely reported. As

Table 5
Binding kinetics of interactions between point-mutated LTαs and hTNFR1 were analyzed by using an SPR biosensor. k_{on} is the association kinetic constant; k_{off} is the dissociation kinetic constant; and K_D is the equilibrium dissociation constant. Relative affinity values were calculated as 100 × K_D (wtLTα)/K_D (point mutated LTα). TNFR1-mediated relative activities of LTα mutants were calculated from the concentration of LTα required for 30% inhibition of HEp-2 cell viability.

	k_{on} (10^6/M s)	k_{off} (10^{-4}/s)	K_D (10^{-10}/M)	Relative affinity (% vs wtLTα)	Relative activity(% vs wtLTα)
wtLTα	1.2	6.1	4.9	100	100
K84S	*0.28*	2.2	*8.0*	*62*	*4810*
K84T	1.0	4.3	118	195	1100
K84A	1.5	5.3	3.5	143	910

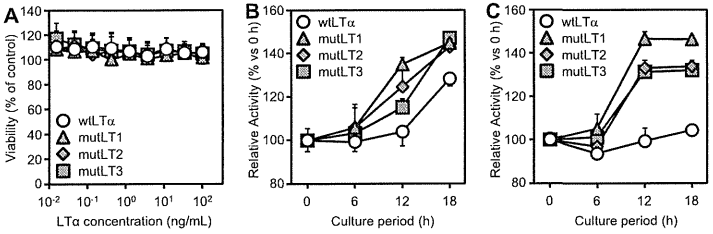

Fig. 4. Caspase activities in HEp-2 cells treated with wtLTα or LTα mutants. (A) Cycloheximide treated HEp-2 cells were incubated with wtLTα or LTα mutants in the presence of zVAD-fmk. After 18 h incubation, cell viability was assessed by methylene blue assay. (B and C) Cycloheximide treated HEp-2 cells were incubated for 6, 12, or 18 h with 10 ng/mL LTαs, and the activities of intracellular caspase-3/7 (B) and intracellular caspase-8 (C) were measured by using Caspase-Glo assays. Each value represents the mean ± SD (n = 4).

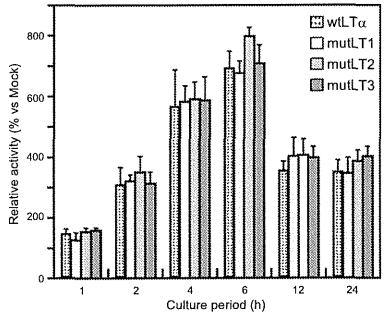

Fig. 5. NFκB activities in HEp-2 cells treated with wtLTα or LTα mutants. HEp-2 cells were co-transfected with pGL4.32 and pRL-TK (Promega). Eighteen hours after transfection, the cells were treated with 10 ng/mL LTαs for the indicated period. The intracellular luciferase activity was then quantified. Data are shown as the relative NFκB activity compared with the mock-transfected group. Each bar represents the mean ± SD (n = 4).

described above, high TNFR1 selectivity of R1selLT was mainly resulted from the significant decreased TNFR2-mediated bioactivity. On the other hand, the TNFR1 selectivity of mutLT1 was obtained from the augmented TNFR1-mediated bioactivity, while TNFR2-mediated bioactivity was maintained. On this point, TNFR2 is known to play essential role for the induction of immune responses. Therefore, we consider that a TNFR1-selective LTα mutants with high TNFR1-mediated and equivalent TNFR2-mediated bioactivity compared to wtLTα, such as mutLT1, would be a superior candidate for cancer therapy by combination of direct pro-apoptotic effects of LTα on tumor cells and an enhancement of local/systemic immunity.

Many cellular signaling processes are hypothesized to depend not only on the equilibrium strength of the ligand–receptor interactions but also on the average durations or kinetic dissociation rates of these interactions [20–23]. In some cases, the intensity of distal signaling depends on the off-rate rather than on the on-rate of the ligand–receptor complex [20,22]. For interactions with TNFR1, the LTα mutants exhibited higher k_{off} values compared with the value for wtLTα, whereas the k_{on} values for the LTα mutants were almost same as that for wtLTα. In addition, the bioactivity of wtLTα and LTα mutants was related to k_{off} but not to k_{on}. These data suggest that the LTα mutants interact with TNFR1 by slow dissociation and induce robust signal transduction. In contrast, for interactions with TNFR2, the LTα mutants showed a higher k_{on} than that for wtLTα, whereas the k_{off} values for the LTα mutants was almost same as that for wtLTα. These data indicate that the detailed molecular dissection of ligand-receptor binding kinetics is important for the construction of functional LTα mutants with desired TNFR-mediated bioactivity.

We previously demonstrated that Lys84 of LTα plays a crucial role in the protein's interaction with the main chain of TNFR1 [12]. Here, to explore the role of Lys84 further, we created LTα mutants with Lys84 replaced by Ser84 or Thr84, and found that the mutant with Ser84 showed slower dissociation kinetics and increased bioactivity when compared with wtLTα or the other mutants (Table 5). These results suggest that Lys84 contributes to the TNFR1-mediated bioactivity and the binding kinetics of the TNFR1–LTα interaction. In all three mutants analyzed here, the amino acid Lys at position 28 was changed to Gln (Table 1). Whereas these mutants exhibited increased TNFR1-mediated bioactivity, our previous data showed that a mutant with a K28Q substitution had decreased TNFR1-mediated bioactivity compared with that of wtLTα. Furthermore, mutLT2, which has the Lys at position 39 replaced by Ser, showed slightly increased TNFR2-mediated bioactivity, but a mutant containing the equivalent substitution at the same position showed decreased TNFR2-mediated bioactivity in our previous study [12]. These results suggest

that the sum of the mutations, including those at positions 28 and 39, were responsible for the augmented binding affinities to TNFR1 and TNFR2.

TNFR1 triggers apoptotic caspase signaling following activation of Fas-associated protein with death domain (FADD) [17]. At the same time, triggering of TNFR1 signals induces the anti-apoptotic NFκB cascade following the activation of TNF receptor-associated death domain (TRADD) and TNF receptor-associated factor (TRAF) adaptors [18,19,24]. Active NFκB induces transcription of a set of genes encoding anti-apoptotic proteins [25,26]. Therefore, in many cell types, TNF α has no apoptotic effects due to the parallel triggering by TNF α of a signaling pathway that activates NFκB *via* the TRADD and TRAF adaptors. Here, however, we found that the LTα mutants, which showed augmented bioactivity *via* TNFR1, efficiently induced caspase activation but induced NFκB to the same level as that induced by wtLTα (Figs. 4 and 5). We consider that the slower rate of dissociation of the LTα mutants from TNFR1 was important to the activation of FADD signaling cascade, but not to the activation of TRADD and TRAF adaptors. We speculate that the alteration of the binding mode of LTα mutant to TNFR1 increased the caspase signaling pathway, but not TRADD- and TRAF-mediated NFκB signaling. These findings will facilitate the construction of functional LTα mutants with even higher receptor selectivity and bioactivity in the future.

5. Conclusions

Here, we created highly bioactive LTα mutants with TNFR1-selectivity by using a phage display technique, and we clarified the molecular basis of their augmented TNFR1-mediated bioactivity. A better understanding of the correlation between structure, kinetic behavior, and activity will likely accelerate drug discovery because it will increase awareness of the properties of therapeutic proteins. We suggest that LTα mutants have the potential to be a powerful tool for cancer therapy by combination of direct pro-apoptotic effects of LTα on tumor cells and an enhancement of local/systemic immunity, and that our findings provide valuable information for the construction of even more functional LTα mutants.

Acknowledgements

The authors declare that they have no conflict of interests. This study was supported in part by grants from the Ministry of Health, Labor, and Welfare in Japan; by the Research on Health Sciences focusing on Drug Innovation from the Japan Health Sciences Foundation; and by the Takeda Science Foundation.

References

[1] Neumann B, Luz A, Pfeffer K, Holzmann B. Defective Peyer's patch organogenesis in mice lacking the 55-kD receptor for tumor necrosis factor. J Exp Med 1996;184:259–64.
[2] Kratz A, Campos-Neto A, Hanson MS, Ruddle NH. Chronic inflammation caused by lymphotoxin is lymphoid neogenesis. J Exp Med 1996;183:1461–72.
[3] Koni PA, Sacca R, Lawton P, Browning JL, Ruddle NH, Flavell RA. Distinct roles in lymphoid organogenesis for lymphotoxins alpha and beta revealed in lymphotoxin beta-deficient mice. Immunity 1997;6:491–500.
[4] Schrama D, thor Straten P, Fischer WH, McLellan AD, Brocker EB, Reisfeld RA, et al. Targeting of lymphotoxin-alpha to the tumor elicits an efficient immune response associated with induction of peripheral lymphoid-like tissue. Immunity 2001;14:111–21.
[5] Schrama D, Voigt H, Eggert AO, Xiang R, Zhou H, Schumacher TN, et al. Immunological tumor destruction in a murine melanoma model by targeted LTalpha independent of secondary lymphoid tissue. Cancer Immunol Immunother 2008;57:85–95.
[6] Ryan SM, Mantovani G, Wang X, Haddleton DM, Brayden DJ. Advances in PEGylation of important biotech molecules: delivery aspects. Expert Opin Drug Deliv 2008;5:371–83.
[7] Yamamoto Y, Tsutsumi Y, Yoshioka Y, Nishibata T, Kobayashi K, Okamoto T, et al. Site-specific PEGylation of a lysine-deficient TNF-alpha with full bioactivity. Nat Biotechnol 2003;21:546–52.
[8] Shibata H, Yoshioka Y, Ikemizu S, Kobayashi K, Yamamoto Y, Mukai Y, et al. Functionalization of tumor necrosis factor-alpha using phage display technique and PEGylation improves its antitumor therapeutic window. Clin Cancer Res 2004;10:8293–300.
[9] Narimatsu S, Yoshioka Y, Watanabe H, Masano T, Morishige T, Yao X, et al. Lysine-deficient lymphotoxin-alpha mutant for site-specific PEGylation. Cytokine 2011;56:489–93.
[10] Everaerdt B, Brouckaert P, Shaw A, Fiers W. Four different interleukin-1 species sensitize to the lethal action of tumour necrosis factor. Biochem Biophys Res Commun 1989;163:378–85.
[11] Brouckaert P, Libert C, Everaerdt B, Fiers W. Selective species specificity of tumor necrosis factor for toxicity in the mouse. Lymphokine Cytokine Res 1992;11:193–6.
[12] Yoshioka Y, Watanabe H, Morishige T, Yao X, Ikemizu S, Nagao C, et al. Creation of lysine-deficient mutant lymphotoxin-alpha with receptor selectivity by using a phage display system. Biomaterials 2010;31:1935–43.
[13] Browning JL, Miatkowski K, Sizing I, Griffiths D, Zafari M, Benjamin CD, et al. Signaling through the lymphotoxin beta receptor induces the death of some adenocarcinoma tumor lines. J Exp Med 1996;183:867–78.
[14] Abe Y, Yoshikawa T, Kamada H, Shibata H, Nomura T, Minowa K, et al. Simple and highly sensitive assay system for TNFR2-mediated soluble- and transmembrane-TNF activity. J Immunol Methods 2008;335:71–8.
[15] Nicholls A, Sharp KA, Honig B. Protein folding and association: insights from the interfacial and thermodynamic properties of hydrocarbons. Proteins 1991;11:281–96.
[16] Mizuguchi K, Deane CM, Blundell TL, Johnson MS, Overington JP. JOY: protein sequence-structure representation and analysis. Bioinformatics 1998;14:617–23.
[17] Sheikh MS, Huang Y. Death receptor activation complexes: it takes two to activate TNF receptor 1. Cell Cycle 2003;2:550–2.
[18] Chen G, Goeddel DV. TNF-R1 signaling: a beautiful pathway. Science 2002;296:1634–5.
[19] Magne N, Toillon RA, Bottero V, Didelot C, Houtte PV, Gerard JP, et al. NF-kappaB modulation and ionizing radiation: mechanisms and future directions for cancer treatment. Cancer Lett 2006;231:158–68.
[20] Hlavacek WS, Redondo A, Metzger H, Wofsy C, Goldstein B. Kinetic proofreading models for cell signaling predict ways to escape kinetic proofreading. Proc Nat Acad Sci USA 2001;98:7295–300.
[21] Liu ZJ, Haleem-Smith H, Chen H, Metzger H. Unexpected signals in a system subject to kinetic proofreading. Proc Nat Acad Sci USA 2001;98:7289–94.
[22] Krippner-Heidenreich A, Tubing F, Bryde S, Willi S, Zimmermann G, Scheurich P. Control of receptor-induced signaling complex formation by the kinetics of ligand/receptor interaction. J Biol Chem 2002;277:44155–63.
[23] Torigoe C, Faeder JR, Oliver JM, Goldstein B. Kinetic proofreading of ligand–FcepsilonRI interactions may persist beyond LAT phosphorylation. J Immunol 2007;178:3530–5.
[24] Kim JY, Lee JY, Kim DG, Koo GB, Yu JW, Kim YS. TRADD is critical for resistance to TRAIL-induced cell death through NF-kappaB activation. FEBS Lett 2011;585:2144–50.
[25] Arch RH, Gedrich RW, Thompson CB. Tumor necrosis factor receptor-associated factors (TRAFs) – a family of adapter proteins that regulates life and death. Genes Dev 1998;12:2821–30.
[26] Deveraux QL, Reed JC. IAP family proteins–suppressors of apoptosis. Genes Dev 1999;13:239–52.

Contents lists available at SciVerse ScienceDirect

Biochemical and Biophysical Research Communications

journal homepage: www.elsevier.com/locate/ybbrc

Annexin A4 is a possible biomarker for cisplatin susceptibility of malignant mesothelioma cells

Takuya Yamashita [a,b,1], Kazuya Nagano [a,1], So-ichiro Kanasaki [a,b], Yuka Maeda [a,b], Takeshi Furuya [a,b], Masaki Inoue [a], Hiromi Nabeshi [b], Tomoaki Yoshikawa [a,b], Yasuo Yoshioka [a,b,c], Norio Itoh [b], Yasuhiro Abe [a], Haruhiko Kamada [a,c], Yasuo Tsutsumi [a,b,c], Shin-ichi Tsunoda [a,c,d,*]

[a] Laboratory of Biopharmaceutical Research, National Institute of Biomedical Innovation, 7-6-8 Saito-Asagi, Ibaraki, Osaka 567-0085, Japan
[b] Laboratory of Toxicology and Safety Science, Graduate School of Pharmaceutical Sciences, Osaka University, 1-6 Yamadaoka, Suita, Osaka 565-0871, Japan
[c] The Center for Advanced Medical Engineering and Informatics, Osaka University, 1-6 Yamadaoka, Suita, Osaka 565-0871, Japan
[d] Laboratory of Biomedical Innovation, Graduate School of Pharmaceutical Sciences, Osaka University, 1-6 Yamadaoka, Suita, Osaka 565-0871, Japan

ARTICLE INFO

Article history:
Received 27 March 2012
Available online 4 April 2012

Keywords:
Malignant mesothelioma
Cisplatin susceptibility
Annexin A4
Biomarker
Proteomics

ABSTRACT

Mesothelioma is a highly malignant tumor with a poor prognosis and limited treatment options. Although cisplatin (CDDP) is an effective anticancer drug, its response rate is only 20%. Therefore, discovery of biomarkers is desirable to distinguish the CDDP-susceptible versus resistant cases. To this end, differential proteome analysis was performed to distinguish between mesothelioma cells of different CDDP susceptibilities, and this revealed that expression of annexin A4 (ANXA4) protein was higher in CDDP-resistant cells than in CDDP-susceptible cells. Furthermore, ANXA4 expression levels were higher in human clinical malignant mesothelioma tissues than in benign mesothelioma and normal mesothelial tissues. Finally, increased susceptibility was observed following gene knockdown of ANXA4 in mesothelioma cells, whereas the opposite effect was observed following transfection of an ANXA4 plasmid. These results suggest that ANXA4 has a regulatory function related to the cisplatin susceptibility of mesothelioma cells and that it could be a biomarker for CDDP susceptibility in pathological diagnoses.

1. Introduction

Malignant mesothelioma is an aggressive neoplasm located on serosal membrane surfaces such as the pleura, and less frequently the peritoneum, and it has a poor outcome. The five-year survival rate is only about 5%. On the other hand, it is well known that asbestos is the major causative agent in the development of this disease [1–3]. Moreover, malignant mesothelioma takes 40–50 years to develop following exposure to asbestos. Because of its adiabatic potential, asbestos was commonly used as a building material in the 1960–1970s. Thus, an increase in mesothelioma patients is expected in the future. Patients with pleural malignant mesothelioma commonly present with an effusion associated with breathlessness that is often accompanied by chest-wall pain and a cough. After confirming the diagnosis, many patients are treated by intensive multidirectional approaches that combine cytoreductive surgery with intrapleural or intraperitoneal chemotherapy [4–8]. However, cytoreductive surgery is not always possible for patients with extensive intraperitoneal disease. Thus, the role of chemotherapy in malignant mesothelioma is critically important.

CDDP is an extensively used anticancer drug for the treatment of malignant mesothelioma, although the response rate is only about 20% [9–12]. A major problem with CDDP treatment of malignant mesothelioma patients is the development of CDDP insusceptibility. Thus, there is an urgent need to further our understanding of the pathogenesis of malignant mesothelioma, particularly with respect to the expression of proteins that confer drug susceptibility, in order to develop novel therapeutic strategies. In this study, a proteomic analysis was performed using high- and low-CDDP-susceptible malignant mesothelioma cells to identify candidate proteins associated with CDDP susceptibility.

2. Materials and methods

2.1. Cells

H28, H2052, H2452, H226 and MSTO-221H were purchased from American Type Culture Collection and maintained in RPMI1640 medium (Wako) containing 10% fetal calf serum (Biowest). Human mesothelial cells (HMC) were purchased from Sciencell and cultured in Mesothelial Cell Growth Medium (ZenBio) under a 5% CO_2 atmosphere at 37 °C.

* Corresponding author at: Laboratory of Biopharmaceutical Research, National Institute of Biomedical Innovation, 7-6-8 Saito-Asagi, Ibaraki, Osaka 567-0085, Japan. Fax: +81 72 641 9817.
E-mail address: tsunoda@nibio.go.jp (S.-i. Tsunoda).
[1] These authors contributed equally to this work.

0006-291X/$ - see front matter © 2012 Elsevier Inc. All rights reserved.
http://dx.doi.org/10.1016/j.bbrc.2012.03.144

2.2. Measurement of cisplatin susceptibility in malignant mesothelioma cells

Malignant mesothelioma cells were seeded into 96-well microplates and cultured overnight. Various concentrations of CDDP were added to each well, the plates were incubated for 24 h, and cell viability was measured using Cell count reagent SF (Nacalai tesque). Absorbance was measured using a microplate reader (Bio-Rad) at test and reference wavelengths of 450 and 650 nm, respectively.

2.3. Proteomic analysis using two dimensional differential in-gel electrophoresis

For proteomic analysis, quantitative analysis was performed using two dimensional differential in-gel electrophoresis (2D-DIGE). Cell lysates were prepared from H28 and H2052 and then solubilized with 7 M urea, 2 M thiourea, 4% CHAPS and 10 mM Tris–HCl (pH 8.5). The lysates were labeled at the ratio of 50 μg proteins: 400 pmol Cy3 or Cy5 protein-labeling dye (GE Healthcare Biosciences) in dimethylformamide according to the manufacturer's protocol. The labelled samples were mixed with rehydration buffer (7 M urea, 2 M thiourea, 4% CHAPS, 2% DTT, 2% Pharmalyte (GE Healthcare Biosciences)) and applied to a 24-cm immobilized pH gradient gel strip (IPG-strip pH 4–7) for separation in the first dimension. For the second dimension separation, the IPG-strips were treated with iodoacetamide and applied to SDS–PAGE gels (10% polyacrylamide and 2.7% *N,N'*-diallyltartardiamide gels). After electrophoresis, the gels were scanned with a laser fluoroimager (Typhoon Trio, GE Healthcare Biosciences). The spot-picking gel was scanned after staining with Deep purple total protein stain (GE Healthcare Biosciences). Quantitative analysis of protein spots was carried out with Decyder-DIA software (GE Healthcare Biosciences). For the antigen spots of interest, spots of 1 mm × 1 mm in size were picked using Ettan Spot Picker (GE Healthcare Biosciences).

2.4. In-gel tryptic digestion

Picked gel pieces were destained with 50% acetonitrile/50 mM NH_4HCO_3 for 20 min twice, dehydrated with 75% acetonitrile for 20 min, and then dried using a centrifugal concentrator. Five microliter of 20 μg/ml trypsin (Promega) solution was added to each gel piece and the pieces were incubated for 16 h at 37 °C. The digested peptides were extracted sequentially using 50%, 80%, and 100% acetonitrile and then dried before being suspended in 10 μl of 0.1% formic acid.

2.5. Mass spectrometry and database search

Extracted peptides were analyzed by liquid chromatography ultra high resolution time-of-flight mass spectrometry (LC-UHR TOF-MS/MS; maXis, Bruker Daltonics). The Mascot search engine (http://www.matrixscience.com) was initially used to query the entire theoretical tryptic peptide database as well as SwissProt (http://www.expasy.org/, a public domain database provided by the Swiss Institute of Bioinformatics). The search query assumed the following: (i) the peptides were mono-, di- or tri-isotopic, (ii) methionine residues may be oxidized, (iii) all cysteines were modified with carbamidomethyl.

2.6. Western blot

The cell lysates were separated in 10% SDS–polyacrylamide gels and transferred to Immobilon membranes (Millipore). After blocking by 4% block ace (DS Pharma Biomedical) for 1 h at room temperature, the blots were reacted with primary antibodies in a buffer containing 0.4% block ace, and then with the appropriate peroxidase-conjugated secondary antibodies in the same buffer. Expression of ANXA4 in malignant mesothelioma cells was detected by mouse anti-human ANXA4 (Abnova: 1D3) followed by an HRP-conjugated anti-mouse IgG antibody (Sigma–Aldrich) using the ECL-plus system (GE Healthcare Biosciences). Equal amounts of protein loading were confirmed by parallel β-actin immunoblotting, and signal quantification was performed by densitometric scanning.

2.7. Immunohistochemistry staining

Human mesothelioma and normal tissue sections were deparaffinated in xylene and rehydrated in a graded series of ethanol dilutions. Heat-induced epitope retrieval was performed by incubating at different temperatures following the manufacturer's instructions using Target Retrieval Solution pH 9 (Dako). After heat-induced epitope retrieval treatment, endogenous peroxidase was blocked with a peroxidase blocking reagent (Dako). Following peroxidase blocking, the slides were incubated with 10% bovine serum albumin (BSA) solution for 30 min at room temperature. The slides were then incubated for 60 min with anti-human ANXA4 monoclonal antibody (9 μg/ml) in 3% BSA at room temperature. After washing 3 times with wash buffer (Dako), the slides were incubated for 30 min with ENVISION + Dual Link (Dako) at room temperature. They were then washed final 3 times and stained with 3,3'-diaminobenzidine. After development, the slides were lightly counterstained with Mayer's hematoxylin and mounted with resinous mounting medium.

2.8. Cisplatin susceptibility in cells transfected with ANXA4-siRNA and ANXA4-plasmid

H28 was transfected with ANXA4-siRNA (target sequence: AAGGATATCACAGAAGGATAT, Qiagen) using Hyperfect reagent (Qiagen) according to the manufacturer's instructions. In contrast, H2052 was transfected with ANXA4-pcDNA 3.1 (a gift from Naka T: Laboratory for Immune Signal, National Institute of Biomedical Innovation) using FuGENE HD transfection reagent (Roche). After transfection, the cells were treated with various concentrations of CDDP for 36 h (ANXA4-siRNA) or 24 h (ANXA4-pcDNA 3.1). Cell viability was measured as described above.

2.9. Statistical analysis

Differences in tumor volumes between the control and target groups were compared using the unpaired Student's *t*-test.

3. Results

3.1. CDDP susceptibility in malignant mesothelioma cells

Cell viability following CDDP treatment was examined to determine which cell lines had higher or lower susceptibility to CDDP. Among five tested mesothelioma cell lines, H2052 was the most and H28 the least susceptible cell line (Fig. 1). The IC_{50} values of H28, H2052, H2452, H226 and MSTO-221H were 154.5, 27.8, 66.0, 87.5 and 49.5 μM, respectively.

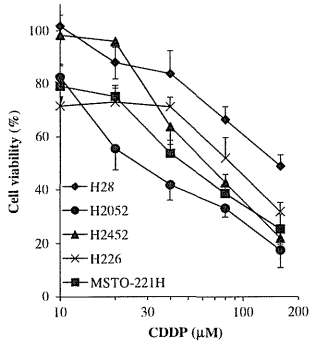

Fig. 1. Susceptibility of malignant mesothelioma cells to CDDP. Mesothelioma cells, H28, H2052, H2452, H226 and MSTO-221H were cultured with various concentrations of CDDP for 24 h 37 °C under 5% CO_2. Cell viability was assayed using the WST-8 assay. Maximal cell viability (100%) was obtained by incubating cells without CDDP. Data are shown as means and standard deviations ($n = 4$).

3.2. Identification of differentially expressed proteins by 2D-DIGE and MS

In order to search for CDDP susceptibility-related proteins, differential proteome analysis between H2052 and H28 cell lines was performed to search for CDDP susceptibility-related proteins (Fig. 2). Quantitative image analysis indicated that a total of eight protein spots representing > 2.0-fold alteration in expression were found and then identified by MS analysis (Table 1). Among those eight proteins, we focused on ANXA4 because this protein plays an important role in membrane stability. Previous reports have indicated that ANXA4 is associated with chemoresistance against platinum-based anticancer drugs in human lung, colon [13] and ovarian cancer [14].

3.3. ANXA4 expression analysis in human malignant mesothelioma cells and mesothelial tissues

Correlations between the expression levels in five malignant mesothelioma cell lines with CDDP-susceptibility were examined using western blot analysis to validate the identified proteins as CDDP susceptibility-related proteins. ANXA4 was expressed at a higher level in H28 cells relative to the other four CDDP-susceptible malignant mesothelioma cell lines (Fig. 3A and B). Expression of ANXA4 in human mesothelial tissue was analyzed by immunohistochemistry staining with an anti-human ANXA4 monoclonal antibody. Fig. 3C indicates that ANXA4 was expressed at higher levels in human malignant mesothelioma tissues than in benign mesothelioma tissues and normal mesothelial tissues.

3.4. Gene regulation of ANXA4 in malignant mesothelioma cells by knockdown and overexpression

ANXA4-siRNA and ANXA4-pcDNA 3.1 were next transfected to H28 and H2052 before CDDP treatment to evaluate correlations between ANXA4 expression levels and CDDP susceptibility. The IC_{50} values of [H28/non treat: H28/control-siRNA: H28/ANXA4-siRNA] were [80.0 μM: 71.8 μM: 15.5 μM] and [H2052/control-pcDNA 3.1: [H2052/ANXA4-pcDNA 3.1] were [55.2 μM: 89.7 μM], respectively (Fig. 4A–D). These results suggested that the CDDP susceptibility of H28 cells was increased by ANXA4-siRNA transfection and that of H2052 cells was decreased by ANXA4-pcDNA 3.1 transfection.

4. Discussion

In this study, a proteomic analysis was performed based on 2D-DIGE using malignant mesothelioma cell lines to identify candidate proteins associated with CDDP susceptibility (Figs. 1 and 2). Eight proteins that were differentially expressed in H28 cells compared with H2052 cells were identified (Table 1). ANXA4 was found to be expressed at a higher level in H28 cells relative to levels in CDDP-susceptible malignant mesothelioma cells by western blot analysis (Fig. 3A and B). Furthermore, ANXA4 was expressed in malignant mesothelioma tissue but not in benign mesothelial tumor and normal mesothelial tissues (Fig. 3C). Thus, ANXA4 was expressed in CDDP-susceptible malignant mesothelioma cells and specifically in malignant mesothelioma tissues. These results indicate that ANXA4 expression in malignant mesothelioma cells may be correlated with CDDP susceptibility, although this relationship must be validated in future studies of human clinical malignant mesothelial cases. The CDDP susceptibility of H28 cells was actually increased by ANXA4 knockdown, and that of H2052 cells was decreased by ANXA4 overexpression (Fig. 4). Thus, these results suggest that ANXA4 plays an important role in chemoresistance against CDDP.

ANXA4 has already been characterized as a regulator of cell membranes with calcium dependency [15–17]. Recently, some studies have reported the protein is associated with membrane permeability [18], ion channels [19] and exocytosis [20,21]. These observations may explain in part the correlation of ANXA4 with modulation of drug susceptibility in cancer cells.

This study demonstrates for the first time elevated ANXA4 protein expression in malignant mesothelioma cells that have less susceptibility to CDDP. *In vitro* evaluation of drug susceptibility against CDDP in malignant mesothelioma cells derived from cancer patients would be important in clinical conditions because doctors as well as patients wish to avoid treatment with inefficacious drugs. Consequently, the susceptibility of a given patient against CDDP could be confirmed by analyzing the expression level of ANXA4 in malignant mesothelioma patients at the time of diagnosis. Furthermore, if ANXA4 expression could be blocked specifically in malignant mesothelioma cells by nucleic acid drugs such as siRNA, this procedure would prove useful in clinical situations involving CDDP treatment. The present study may contribute to

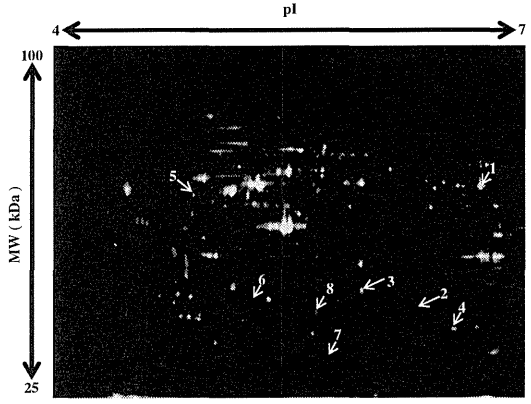

Fig. 2. 2D-DIGE image of fluorescently labeled proteins from human mesothelioma cell lines H28 and H2052. Proteins from high- and low-susceptible mesothelioma cells (H2052, H28) were labeled with cy3 and cy5, respectively, and 2D electrophoresis was performed. The differentially expressed spots in H28 indicated by white arrows were then identified by LC-TOF-MS/MS. Table 1 contains additional information about the identified proteins.

Table 1
Proteins expressed at higher or lower levels in H28 compared to H2052.

No.	Accession number	Protein name	pI	MW (kDa)	Expression ratio (H28/H2052)
1	P11413	Glucose-6-phosphate 1-dehydrogenase	6.4	59.3	21.0
2	P78417	Glutathione *S*-transferase omega-1	6.2	27.6	7.4
3	P09525	Annexin A4	5.6	35.9	3.6
4	P30041	Peroxiredoxin-6	6.0	25.0	3.5
5	Q09028	Histone-binding protein RBBP4	4.7	47.7	3.0
6	P07195	L-lactate dehydrogenase B chain	5.7	36.6	2.9
7	P32119	Peroxiredoxin-2	5.7	21.9	0.03
8	Q9Y696	Chloride intracellular channel protein 4	5.5	28.8	0.13

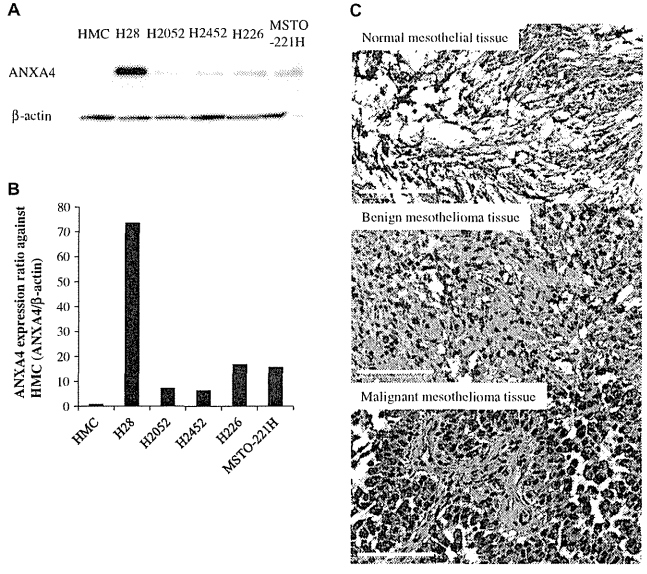

Fig. 3. ANXA4 expression analysis in human malignant mesothelioma cells and mesothelial tissues. ANXA4 expression levels in human primary mesothelial cells, HMC, and mesothelioma cell lines (H28, H2052, H2452, H226, MSTO-221H) were analyzed by western blotting (A). Intensity of the western blotting images was quantified by densitometry (B). Expression of ANXA4 in human mesothelial tissues was analyzed by immunostaining using an anti-human ANXA4 antibody (C). Top, middle and bottom panels are normal mesothelial, benign and malignant mesothelioma tissues, respectively. The tissue sections were counterstained using hematoxylin. Representative 400 × photomicrographs presented (bar: 100 μm).

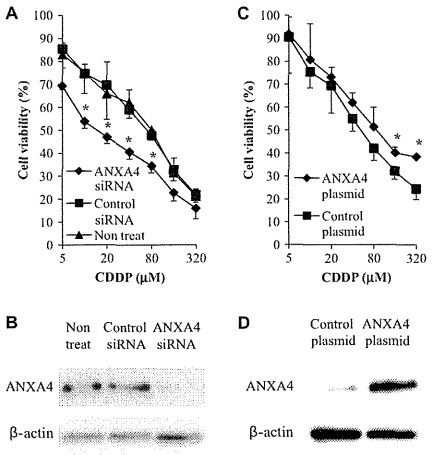

Fig. 4. The effect of ANXA4 gene knockdown and overexpression on CDDP susceptibility in malignant mesothelioma cells. Transfection of ANXA4 siRNA or plasmid into malignant mesothelioma cells confers resistance to CDDP. Cell survival after 24 h treatment of H28/ANXA4 siRNA or H2052/ANXA4 plasmid with different concentrations of CDDP (A and C). Expression of ANXA4 was analyzed by western blot analysis (B and D). Data are shown as means and standard deviations ($n = 4$). *$P < 0.05$ (Control siRNA or plasmid vs. ANXA4 siRNA or plasmid).

establishment of a new therapeutic strategy for malignant mesothelioma patients by suggesting a novel diagnostic and therapeutic target.

Acknowledgments

This study was supported in part by Grants-in-Aid for Scientific Research from the Ministry of Education, Culture, Sports, Science and Technology of Japan, and from the Japan Society for the Promotion of Science (JSPS). This study was also supported in part by Health Labor Sciences Research Grants from the Ministry of Health, Labor and Welfare of Japan and by Health Sciences Research Grants for Research on Publicly Essential Drugs and Medical Devices from the Japan Health Sciences Foundation.

References

[1] W.N. Rom, W.D. Travis, A.R. Brody, Cellular and molecular basis of the asbestos-related diseases, Am. Rev. Respir. Dis. 143 (1991) 408–422.

[2] N.H. Heintz, Y.M. Janssen-Heininger, B.T. Mossman, Asbestos, lung cancers, and mesotheliomas: from molecular approaches to targeting tumor survival pathways, Am. J. Respir. Cell Mol. Biol. 42 (2010) 133–139.

[3] Consensus Report: Asbestos, asbestosis, and cancer: the Helsinki criteria for diagnosis and attribution. Scand. J. Work Environ. Health 23 (1997) 311–316.

[4] T.D. Yan, L. Welch, D. Black, P.H. Sugarbaker, A systematic review on the efficacy of cytoreductive surgery combined with perioperative intraperitoneal chemotherapy for diffuse malignancy peritoneal mesothelioma, Ann. Oncol. 18 (2007) 827–834.

[5] E. Chailleux, D. Pioche, S. Chopra, G. Dabouis, P. Germaud, A.Y. De Lajartre, M. De Lajartre, Prognostic factors in diffuse malignant pleural mesothelioma: a study of 167 patients, Chest 93 (1988) 159–162.

[6] K.S. Sridhar, R. Doria, W.A. Raub Jr., R.J. Thurer, M. Saldana, New strategies are needed in diffuse malignant mesothelioma, Cancer 70 (1992) 2969–2979.

[7] M. Markman, D. Kelsen, Efficacy of cisplatin-based intraperitoneal chemotherapy as treatment of malignant peritoneal mesothelioma, J. Cancer Res. Clin. Oncol. 118 (1992) 547–550.

[8] G.H. Eltabbakh, M.S. Piver, R.E. Hempling, F.O. Recio, M.E. Intengen, Clinical picture, response to therapy, and survival of women with diffuse malignant peritoneal mesothelioma, J. Surg. Oncol. 70 (1999) 6–12.

[9] T. Berghmans, M. Paesmans, Y. Lalami, I. Louviaux, S. Luce, C. Mascaux, A.P. Meert, J.P. Sculier, Activity of chemotherapy and immunotherapy on malignant mesothelioma: a systematic review of the literature with meta-analysis, Lung. Cancer 38 (2002) 111–121.

[10] H.J. Lerner, D.A. Schoenfeld, A. Martin, G. Falkson, E. Borden, Malignant mesothelioma: The Eastern Cooperative Oncology Group (ECOG) experience, Cancer 52 (1983) 1981–1985.

[11] D.M. Mintzer, D. Kelsen, D. Frimmer, R. Heelan, R. Gralla, Phase II trial of high-dose cisplatin in patients with malignant mesothelioma, Cancer Treat Rep. 69 (1985) 711–712.

[12] B.L. Zidar, S. Green, H.I. Pierce, R.W. Roach, S.P. Balcerzak, L. Militello, A phase II evaluation of cisplatin in unresectable diffuse malignant mesothelioma: a Southwest Oncology Group Study, Invest New Drugs 6 (1988) 223–226.

[13] E.K. Han, S.K. Tahir, S.P. Cherian, N. Collins, S.C. Ng, Modulation of paclitaxel resistance by annexin IV in human cancer cell lines, Br. J. Cancer 83 (2000) 83–88.

[14] A. Kim, T. Enomoto, S. Serada, Y. Ueda, T. Takahashi, B. Ripley, T. Miyatake, M. Fujita, C.M. Lee, K. Morimoto, M. Fujimoto, T. Kimura, T. Naka, Enhanced expression of Annexin A4 in clear cell carcinoma of the ovary and its association with chemoresistance to carboplatin, Int. J. Cancer 125 (2009) 2316–2322.

[15] M.A. Kaetzel, P. Hazarika, J.R. Dedman, Differential tissue expression of three 35-kDa annexin calcium-dependent phospholipid-binding proteins, J. Biol. Chem. 264 (1989) 14463–14470.

[16] G. Zanotti, G. Malpeli, F. Gliubich, C. Folli, M. Stoppini, L. Olivi, A. Savoia, R. Berni, Structure of the trigonal crystal form of bovine annexin IV, Biochem. J. 329 (1998) 101–106.

[17] M.A. Kaetzel, Y.D. Mo, T.R. Mealy, B. Campos, W. Bergsma-Schutter, A. Brisson, J.R. Dedman, B.A. Seaton, Phosphorylation mutants elucidate the mechanism of annexin IV-mediated membrane aggregation, Biochemistry 40 (2001) 4192–4199.

[18] W.G. Hill, M.A. Kaetzel, B.K. Kishore, J.R. Dedman, M.L. Zeidel, Annexin A4 reduces water and proton permeability of model membranes but does not alter aquaporin 2-mediated water transport in isolated endosomes, J. Gen. Physiol. 121 (2003) 413–425.

[19] M.A. Kaetzel, H.C. Chan, W.P. Dubinsky, J.R. Dedman, D.J. Nelson, A role for annexin IV in epithelial cell function. Inhibition of calcium-activated chloride conductance, J. Biol. Chem. 269 (1994) 5297–5302.

[20] H. Sohma, C.E. Creutz, S. Gasa, H. Ohkawa, T. Akino, Y. Kuroki, Differential lipid specificities of the repeated domains of annexin IV, Biochim. Biophys. Acta 1546 (2001) 205–215.

[21] A. Piljic, C. Schultz, Annexin A4 self-association modulates general membrane protein mobility in living cells, Mol. Biol. Cell 17 (2006) 3318–3328.

Laboratory of Biopharmaceutical Research[1], National Institute of Biomedical Innovation; Laboratory of Toxicology and Safety Science[2], Graduate School of Pharmaceutical Sciences; The Center for Advanced Medical Engineering and Informatics[3]; Laboratory of Biomedical Innovation[4], Graduate School of Pharmaceutical Sciences, Osaka University, Osaka, Japan

Rho GDP-dissociation inhibitor alpha is associated with cancer metastasis in colon and prostate cancer

T. YAMASHITA[1,2,*], T. OKAMURA[1,*], K. NAGANO[1,*], S. IMAI[1], Y. ABE[1], H. NABESHI[1,2], T. YOSHIKAWA[1,2], Y. YOSHIOKA[1,2,3], H. KAMADA[1,3], Y. TSUTSUMI[1,2,3], S. TSUNODA[1,3,4]

Received July 7, 2011, accepted August 5, 2011

Shin-ichi Tsunoda, Ph.D, Laboratory of Biopharmaceutical Research, National Institute of Biomedical Innovation, 7-6-8 Saito-Asagi, Ibaraki, Osaka 567-0085, Japan.
tsunoda@nibio.go.jp
**These authors contributed equally to the work.*

Pharmazie 67: 253–255 (2012) *doi: 10.1691/ph.2012.1630*

Since metastasis is one of the most important prognostic factors in colorectal cancer, development of new methods to diagnose and prevent metastasis is highly desirable. However, the molecular mechanisms leading to the metastatic phenotype have not been well elucidated. In this study, a proteomics-based search was carried out for metastasis-related proteins in colorectal cancer by analyzing the differential expression of proteins in primary versus metastasis focus-derived colorectal tumor cells. Protein expression profiles were determined using a tissue microarray (TMA), and the results identified Rho GDP-dissociation inhibitor alpha (Rho GDI) as a metastasis-related protein in colon and prostate cancer patients. Consequently, Rho GDI may be useful as a diagnostic biomarker and/or a therapeutic to prevent colon and prostate cancer metastasis.

1. Introduction

Colorectal cancer is known as a major metastatic cancer, and 40–50% of patients already have a metastatic focus at presentation. Moreover, the 5-year survival of these patients is under 10% (Davies et al. 2005). Thus, metastasis is one of the most important prognostic factors in colorectal cancer. In order to improve rates of cancer remission, it will be necessary to clarify the detailed molecular mechanisms of cancer metastasis and to utilize this information to establish new diagnostic and therapeutic techniques. Many researchers have searched for metastasis-related molecules (Liu et al. 2010; Shuehara et al. 2011) using proteomics techniques (Hanash 2003). Comprehensive mapping of the molecular changes during metastasis would greatly improve our understanding of the recurrence and management of cancer. However, the knowledge gained so far in these studies has not been sufficient to improve cancer remission rates.

Here we show the potential of Rho GDI as a metastasis-related protein in colon and prostate cancer patients. In order to identify metastasis-related proteins, the protein expression patterns of human colorectal cancer cells with different metastatic characters were compared. Because these cells were derived from the same patient (SW480: a surgical specimen of a primary colon adenocarcinoma, SW620: a lymph node metastatic focus), cancer metastasis-related protein candidates could be effectively sought without background variations due to differences between individuals. Furthermore, by analyzing the expression of candidate proteins in many clinical samples using a TMA, we attempted to validate the association of these candidates with metastasis. TMA is a slide glass containing many clinical tissues, and it enables one to carry out a high-throughput analysis by evaluating the relationship between expression profiles of each candidate molecule and clinical information such as metastasis. (Imai et al. 2011; Yoshida et al. 2011).

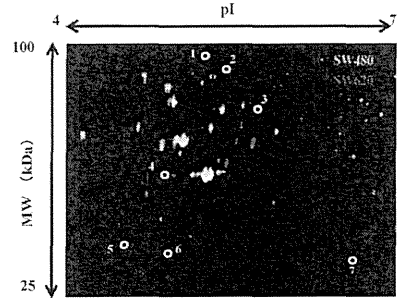

Fig. 1: 2D-DIGE image of fluorescently-labeled proteins from different metastatic human colorectal cancer cells. SW480 is human colorectal cancer cell line derived from a primary tumor and SW620 is derived from a metastatic focus from the same patient. Proteins from the colon cancer cells (SW480, SW620) were labeled with Cy3 and Cy5 respectively, and analyzed by 2D electrophoresis. The differentially-expressed spots (white circles) were then identified by LC-UHR TOF/MS

Table 1: High expression proteins in SW620 compared to SW480

	Accession	Protein name	MW (kDa)	pI	Ratio (SW620 / SW480)
1	P12109	collagen alpha-1(VI) chain	108.6	5.3	1.53
2	Q15459	splicing factor 3A subunit 1	88.9	5.2	1.61
3	P13797	T-plastin	70.9	5.5	1.59
4	P60709	actin cytoplasmic 1	42.1	5.3	1.50
5	P63104	14-3-3 zeta/delta	27.9	4.7	1.63
6	P52565	Rho GDP-dissociation inhibitor 1 (Rho GDI)	23.3	5.0	1.90
7	P30041	Peroxiredoxin-6 (PRDX6)	25.1	6.0	1.86

2. Investigations, results and discussion

In order to search for metastasis-related proteins, we analyzed differentially-expressed proteins between SW480 and SW620 by two-dimensional differential in-gel electrophoresis (2D-DIGE) (Fig. 1). As a result, 7 spots with at least a 1.5-fold-altered expression level were found by quantitative analysis, and these spots were identified by mass spectrometry (Table 1). Three molecules having a high SW620/SW480 expression ratio indicating a strong association with cancer metastasis were identified: Rho GDP-dissociation inhibitor alpha (Rho GDI), peroxiredoxin-6 (PRDX6) and 14-3-3 zeta/delta.

The expression profiles of these proteins were analyzed by immunohistochemistry using the TMA with colon cancer and multiple cancer tissues. Results of this analysis indicated that expression of PRDX6 and 14–3-3 zeta/delta had no relationship to the clinical status of cancer metastasis (data not shown). On the other hand, in positive cases of lymph node metastasis, the expression ratio of Rho GDI was significantly higher than in the negative cases. Furthermore, the same trend was seen when tissues from prostate cancer patients were analyzed (Table 2).

To confirm these results, the expression levels of Rho GDI protein in colon cancer cell lines with different metastatic potential (SW480 < SW620 < SW620-OK1 < SW620-OK2: Characteristics of SW620-OK1 and SW620-OK2 are described in *Experimental*) were investigated by western blot analysis (Fig. 2). The expression of Rho GDI was found to be up-regulated with the development of metastatic characteristics. These results suggested that Rho GDI is correlated with cancer metastasis.

Rho GDI has been identified as key regulator of Rho family GTPases. Activation of growth factor receptors and integrins can promote the exchange of GDP for GTP on Rho proteins (Bishop et al. 2000). Furthermore, GTP-bound Rho proteins interact with a range of effector molecules to modulate their activity or localization, and this leads to changes in cell behavior. It is clear that Rho family GTPases are involved in the control of cell morphology and motility (Etienne-Manneville et al. 2002; Hall et al. 1997; Van Aelst et al. 1997). The importance of Rho protein and Rho GDI in cancer progression, particularly in the area of metastasis, is becoming increasingly evident. Recently, some reports have indicated that the expression of Rho GDI was correlated with colorectal and breast cancer metastasis (Zhao et al. 2008; Kang et al. 2010). Thus, our findings are consistent with these reports and further suggest that the expression of Rho GDI is also correlated with prostate cancer metastasis. Consequently, Rho GDI should be considered as a diagnostic marker or new therapeutic target for cancer metastasis.

3. Experimental

3.1. Cell lines

SW480 is a human colorectal cancer cell line derived from a primary focus and SW620 is derived from a metastatic focus of the same patient. These cells were purchased from American Type Culture Collection and maintained at 37 °C using Leibovitz's L-15 medium (Wako) supplemented with 10% FCS. SW620-OK1 and -OK2 were established by the following procedure: 1×10^6 SW620 cells were injected into the spleens of nu/nu mice. After 8 weeks, SW620-OK1 was established from a liver metastatic focus. Furthermore, SW620-OK2 was established from SW620-OK1 using the same procedures.

3.2. 2D-DIGE analysis

Cell lysates were prepared from SW480 and SW620 and then solubilized with 7 M urea, 2 M thiourea, 4% CHAPS and 10 mM Tris-HCl (pH 8.5). The lysates were labeled at the ratio of 50 µg proteins: 400 pmol Cy3 or Cy5 protein-labeling dye (GE Healthcare Biosciences) in dimethylformamide according to the manufacturer's protocol. Briefly, the labelled samples were mixed with rehydration buffer (7 M urea, 2 M thiourea, 4% CHAPS, 2% DTT, 2% Pharmalyte (GE Healthcare Biosciences)) and applied to a 24-cm immobilized pH gradient gel strip (IPG-strip pH 4–7 NL) for separation in the first dimension. Samples for the spot-picking gel were prepared without labelling by Cy-dyes. For the second dimension separation, the IPG-strips were applied to SDS-PAGE gels (10% polyacrylamide and 2.7% N,N'-diallyltartardiamide gels). After electrophoresis, the gels were scanned with a laser fluoroimager (Typhoon Trio, GE Healthcare Biosciences). The spot-picking gel was scanned after staining with Deep Purple Total Protein Stain (GE Healthcare Biosciences). Quantitative analysis of protein spots was carried out with Decyder-DIA software (GE Healthcare Biosciences). For the antigen spots of interest, spots of 1 mm × 1 mm in size were picked using Ettan Spot Picker (GE Healthcare Biosciences).

3.3. In-gel tryptic digestion

Picked gel pieces were digested with trypsin as described below. The gel pieces were destained with 50% acetonitrile/50 mM NH_4HCO_3 for 20 min twice, dehydrated with 75% acetonitrile for 20 min, and then dried using a centrifugal concentrator. Next, 5 µl of 20 µl/ml trypsin (Promega) solution was added to each gel piece and incubated for 16 h at 37 °C. Three solutions were used to extract the resulting peptide mixtures from the gel pieces. First, 50 µl of 50% (v/v) acetonitrile in 0.1% (v/v) formic acid (FA) was added to the gel pieces, which were then sonicated for 5 min. Next, we collected the solution and added 80% (v/v) acetonitrile in 0.1% FA. Finally, 100% acetonitrile was added for the last extraction. The peptides were dried and then re-suspended in 10 µl of 0.1% FA.

3.4. Mass spectrometry and database search

Extracted peptides were analyzed by liquid chromatography Ultra High Resolution time-of-flight mass spectrometry (LC-UHR TOF/MS; maXis, Bruker Daltonics). The Mascot search engine (http://www.matrixscience.com) was initially used to query the entire theoretical tryptic peptide database as well as SwissProt (http://www.expasy.org/, a public domain database provided by the Swiss Institute of Bioinformatics). The search query assumed the following: (i) the peptides were monoisotopic (ii) methionine residues may be oxidized (iii) all cysteines are modified with iodoacetamide.

Table 2: Expression profile of Rho GDI in primary cancers with or without lymph node metastasis

	Number of Rho GDI positive cases (positive ratio)	
	in metastasis negative cases	in metastasis positive cases
Colon cancer*	11/14 (79%)	19/19 (100%)
Prostate cancer*	18/23 (78%)	11/11 (100%)

* $p < 0.05$: Mann Whitney U test

3.5. TMA Immunochemical staining

TMA slides with human colon cancer samples or multiple cancer samples (Biomax) were de-paraffinated in xylene and rehydrated in a graded series of ethanol washes. Heat-induced epitope retrieval was performed while maintaining the Target Retrieval Solution pH 9 (Dako) at the desired temperature according to manufacturer's instructions. After the treatment, endogenous peroxidase was blocked with 0.3% H_2O_2 in Tris-buffer saline (TBS) for 5 min. After washing twice with TBS, TMA slides were incubated with 10% BSA blocking solution for 30 min. The slides were then incubated with the anti-Rho GDI (Santa Cruz Biotechnology) for 60 min. After washing three times with wash buffer (Dako), each series of sections was incubated for 30 min with Envision + Dual Link (Dako). The reaction products were rinsed twice with wash buffer and then developed in liquid 3, 3'-diaminobenzidine (Dako) for 3 min. After the development, sections were counterstained with Mayer's hematoxylin. All procedures were performed using AutoStainer (Dako).

3.6. TMA Immunohistochemistry scoring

The optimized staining conditions for TMAs corresponding to human colon as well as multiple cancers were determined based on the co-existence of both positive and negative cells in the same tissue sample. Signals were considered positive when reaction products were localized in the expected cellular component. The criteria for scoring of stained tissues were as follows: the distribution score was 0 (0%), 1 (1–50%) or 2 (51–100%), indicating the percentage of positive cells among all tumor cells present in one tissue. The intensity of the signal (intensity score) was scored as 0 (no signal), 1 (weak), 2 (moderate) or 3 (marked). The distribution and intensity scores were then summed into a total score (TS) of TS0 (sum = 0), TS1 (sum = 2), TS2 (sum = 3), and TS3 (sum = 4–5). Throughout this study, TS0 or TS1 was regarded as negative, whereas TS2 or TS3 were regarded as positive.

3.7. Western Blot

Expression of Rho GDI in colon cancer cells was detected by anti-Rho GDI (Santa Cruz Biotechnology) and HRP conjugated anti-mouse IgG antibody (Sigma) using the ECL-plus system. Equal amounts of protein loading were confirmed by parallel β-actin immunoblotting, and signal quantification was performed by densitometric scanning.

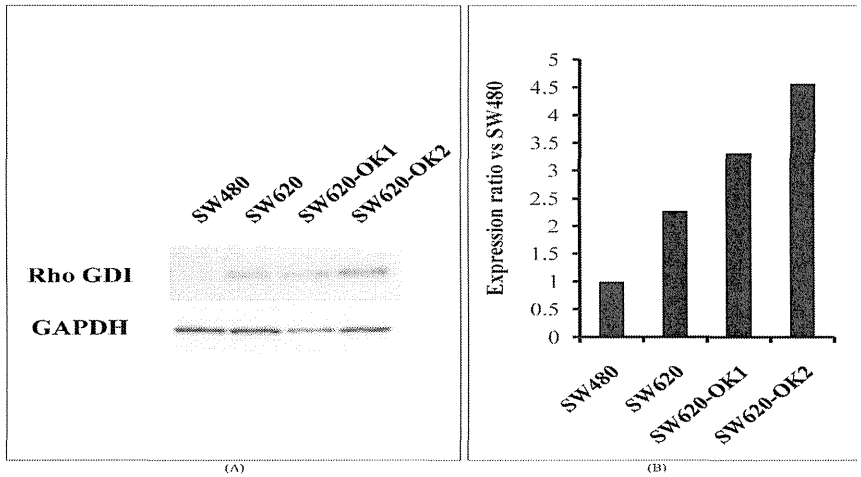

Fig. 2: Rho GDI expression levels in colon cancer cell lines with different metastatic abilities. Rho GDI expression levels in colon cancer cell lines (SW480, SW620, SW620-OK1, SW620-OK2) analyzed by western blotting (A). SW620-OK1, SW620-OK2 have been established as high metastatic sub-lines of SW620 using a mouse metastasis model. Intensity of the western blotting images was quantified by densitometry (B)

Acknowledgements: This study was supported in part by Grants-in-Aid for Scientific Research from the Ministry of Education, Culture, Sports, Science and Technology of Japan, and from the Japan Society for the Promotion of Science (JSPS). This study was also supported in part by Health Labor Sciences Research Grants from the Ministry of Health, Labor and Welfare of Japan.

References

Bishop AL, Hall A (2000) Rho GTPases and their effector proteins. Biochem J 348: 241–255.

Davies RJ, Miller R, Coleman N (2005) Colorectal cancer screening: prospects for molecular stool analysis. Nat Rev Cancer 5: 199–209.

Etienne-Manneville S, Hall A (2002) Rho GTPases in cell biology. Nature 420: 629–635.

Hall A (1997). Rho GTPases and the Actin cytoskeleton. Science 279: 509–514.

Hanash S (2003) Disease proteomics. Nature 422: 226–232.

Imai S, Nagano K, Yoshida Y, Okamura T, Yamashita T, Abe Y, Yoshikawa T, Yoshioka Y, Kamada H, Mukai Y, Nakagawa S, Tsutsumi Y, Tsunoda S (2011). Development of an antibody proteomics system using a phage antibody library for efficient screening of biomarker proteins. Biomaterials 32: 162–169.

Kang S, Kim MJ, An H, Kim BG, Choi YP, Kang KS, Gao MQ, Park H, Na HJ, Kim HK, Yun HR, Kim DS, Cho NH (2010) Proteomic molecular portrait of interface zone in breast cancer. J Proteome Res 9: 5638–5645.

Liu R, Wang K, Yuan K, Wei Y, Huang C (2010) Integrative oncoproteomics strategies for anticancer drug discovery. Expert Rev Proteomics 7: 411–429.

Sahai E (2007). Illuminating the metastatic process. Nat Rev Cancer 7: 737–749.

Suehara Y, Tochigi N, Kubota D, Kikuta K, Nakayama R, Seki K, Yoshida A, Ichikawa H, Hasegawa T, Kaneko K, Chuman H, Beppu Y, Kawai A, Kondo T (2011) Secernin-1 as a novel prognostic biomarker candidate of synovial sarcoma revealed by proteomics. J Proteomics 74: 829–842.

Van Aelst L, D'Souza-Schorey C (1997) Rho GTPases and signaling networks. Genes Dev 11: 2295–2322.

Yoshida Y, Yamashita T, Nagano K, Imai S, Nabeshi H, Yoshikawa T, Yoshioka Y, Abe Y, Kamada H, Tsutsumi Y, Tsunoda S (2011) Limited expression of reticulocalbin-1 in lymphatic endothelial cells in lung tumor but not in normal lung. Biochem Biophys Res Commun 405: 610–614.

Zhao L, Wang H, Li J, Liu Y, Ding Y (2008) Overexpression of Rho GDP-dissociation inhibitor alpha is associated with tumor progression and poor prognosis of colorectal cancer. J Proteome Res 7: 3994–4003.

Nanoscale Research Letters
a SpringerOpen Journal

NANO EXPRESS Open Access

Hemopexin as biomarkers for analyzing the biological responses associated with exposure to silica nanoparticles

Kazuma Higashisaka[1†], Yasuo Yoshioka[1*†], Kohei Yamashita[1], Yuki Morishita[1], Huiyan Pan[1], Toshinobu Ogura[1], Takashi Nagano[1], Akiyoshi Kunieda[1], Kazuya Nagano[2], Yasuhiro Abe[3], Haruhiko Kamada[2,4], Shin-ichi Tsunoda[2,4], Hiromi Nabeshi[5], Tomoaki Yoshikawa[1] and Yasuo Tsutsumi[1,2,4*]

Abstract

Practical uses of nanomaterials are rapidly spreading to a wide variety of fields. However, potential harmful effects of nanomaterials are raising concerns about their safety. Therefore, it is important that a risk assessment system is developed so that the safety of nanomaterials can be evaluated or predicted. Here, we attempted to identify novel biomarkers of nanomaterial-induced health effects by a comprehensive screen of plasma proteins using two-dimensional differential in gel electrophoresis (2D-DIGE) analysis. Initially, we used 2D-DIGE to analyze changes in the level of plasma proteins in mice after intravenous injection via tail veins of 0.8 mg/mouse silica nanoparticles with diameters of 70 nm (nSP70) or saline as controls. By quantitative image analysis, protein spots representing >2.0-fold alteration in expression were found and identified by mass spectrometry. Among these proteins, we focused on hemopexin as a potential biomarker. The levels of hemopexin in the plasma increased as the silica particle size decreased. In addition, the production of hemopexin depended on the characteristics of the nanomaterials. These results suggested that hemopexin could be an additional biomarker for analyzing the biological responses associated with exposure to silica nanoparticles. We believe that this study will contribute to the development of biomarkers to ensure the safety of silica nanoparticles.

Keywords: Silica nanoparticle, Plasma proteins, Hemolysis, Biomarker

Background

Nanomaterials with particle sizes below 100 nm display unique properties compared to conventional materials with a submicron size. Various types of nanomaterials have been designed and produced for consumer and industrial applications such as medicine, cosmetics, and food [1,2]. As the use of nanomaterials increases, there is a growing need to ensure their safety because their unique properties might be associated with undesirable biological interactions [3,4]. However, current knowledge of the potential risk of nanomaterials is considered insufficient. Therefore, to facilitate the development of nanomaterials as a safe and usable product, it is important to develop guidelines for evaluation of their safety and efficacy.

Silica nanoparticles have been widely used in many consumer products such as cosmetics, food, and medicine because of their useful properties, including straightforward synthesis, relatively low cost, easy separation, and easy surface modification [5,6]. However, recent studies have found that silica nanoparticles induce substantial lung inflammation and are cytotoxic to various cell types [7,8]. Furthermore, our group showed that silica nanoparticles penetrate the skin and produce systemic exposure after topical application [9]. These findings underscore the need to examine biological effects after systemic exposure to silica nanoparticles. Our group also demonstrated that intravenous injection of silica nanoparticles with a diameter of 70 nm into mice might induce severe liver damage [9-12] and pregnancy complications such as resorption and fetal growth restriction [13]. We also showed that these pregnancy complications can be suppressed by amino or carboxyl group surface modification [11,13].

The development of safe nanomaterials requires not only an evaluation of safety, but also the ability to predict their biological effects. Molecular biomarkers constitute an objective indicator for correlating against various physiological conditions or variation of disease state [14,15]. Biomarker studies have the potential to provide valuable information to identify early biological events associated with the adverse health effects of engineered nanomaterials in a development stage more easily and rapidly [16]. Studies of biomarkers for nanomaterials have barely advanced, but it is envisaged that a biomarker profile for exposure to nanomaterials would represent the unity of local and systemic physiological responses induced as a result of exposure. Therefore, there is a need to identify and evaluate biomarkers for nanomaterials that would be suitable for predicting the potential toxicity of nanomaterials as well as to facilitate the development of nanomaterials that are safe. In this regard, our previous study used sodium dodecyl sulfate-polyacrylamide gel electrophoresis (SDS-PAGE) analysis to show that the acute-phase proteins, haptoglobin, C-reactive protein, and serum amyloid A (SAA), can act as useful biomarkers for analyzing the risk of exposure to nanomaterials and their associated toxicity [17]. However, SDS-PAGE analysis has limited capacity for a comprehensive screen for biomarkers because it is based only on differences in molecular weight of proteins. Proteomics-based analyses such as two-dimensional (2D) gel separation and mass spectrometry are more suitable approaches for such a comprehensive study. Here, we performed a screen for biomarkers of nanomaterials using two-dimensional differential in gel electrophoresis (2D-DIGE), which is a gel-based approach like SDS-PAGE but separates proteins on the basis of their molecular weight and isoelectric point. We used this approach to identify hemopexin as a potential biomarker for predicting the biological effects induced by silica nanoparticles.

Methods

Materials

Silica particles were purchased from Micromod Partikeltechnologie (Rostock/Warnemünde, Germany). Silica particles with diameters of 70, 300, and 1,000 nm (nSP70, nSP300, and mSP1000, respectively) and nSP70 with surface carboxyl and amino groups (nSP70-C and nSP70-N, respectively), were used in this study. The silica particles were suspended in saline, sonicated for 5 min, and vortexed for 1 min prior to use.

Animals

Female BALB/c mice were purchased from Nippon SLC, Inc. (Shizuoka, Japan) and were used at 6 to 8 weeks of age. The mice were housed in a ventilated animal room maintained at 20 ± 2°C with a 12-h light/12-h dark cycle. The mice had free access to water and forage (FR-2, Funabashi farm, Chiba, Japan). All of the animal experimental procedures used in this study were performed in accordance with the Osaka University and National Institute of Biomedical Innovation guidelines for the welfare of animals.

2D-DIGE analysis

The BALB/c mice were treated intravenously with 0.8 mg/mouse nSP70 or saline. After 24 h, blood samples were collected, and plasma was harvested by centrifuging blood at 13,800×*g* for 15 min. ProteoPrep (Sigma-Aldrich, Saint Louis, MO, USA) was used to remove albumin and immunoglobulin from the plasma according to the manufacturer's instructions. Plasma proteins were purified from the plasma of the nSP70- or saline-treated mice using a 2D-Clean up Kit (GE Healthcare Biosciences, Piscataway, NJ, USA) and were labeled at the ratio of 50 μg proteins:400 pmol Cy3 or Cy5 protein-labeling dye (GE Healthcare Biosciences) in dimethylformamide according to the manufacturer's protocol. Briefly, 50 μg of each labeled sample was mixed with rehydration buffer (7 M urea, 2 M thiourea, 4% 3-(3-cholamidepropyl) dimethylammonio-1-propanesulphonate, 2% dithiothreitol, 2% Pharmalyte; GE Healthcare Biosciences) and applied to a 24-cm immobilized pH gradient gel strip (immobilized pH gradient (IPG) strip pH 4 to 7 NL) for separation in the first dimension. Samples for the spot picking gel were prepared without labeling by Cy dyes. For the second-dimension separation, the IPG strips were applied to SDS-PAGE gels (10% polyacrylamide and 2.7% *N,N'*-diallyltartardiamide gels). After electrophoresis, the gels were scanned with a laser fluoroimager (Typhoon Trio, GE Healthcare Biosciences). The spot picking gel was scanned after staining with Deep Purple Total Protein Stain (GE Healthcare Biosciences). Quantitative analysis of protein spots was carried out with Decyder-DIA software (GE Healthcare Biosciences). Protein spots representing greater than twofold alteration in expression were picked using an Ettan Spot Picker (GE Healthcare Biosciences).

In-gel tryptic digestion

The gel pieces were destained with 50% acetonitrile (ACN)/25 mM NH_4HCO_3 for 10 min, dehydrated with 100% ACN for 10 min, and then dried using a centrifugal concentrator (TOMY SEIKO, Tokyo, Japan). Next, 8 μl of 20 μl/ml trypsin solution (Promega, Madison, WI, USA) diluted fivefold in 50 mM NH_4HCO_3 was

* Correspondence: yasuo@phs.osaka-u.ac.jp; ytsutsumi@phs.osaka-u.ac.jp
†Equal contributors
[1]Laboratory of Toxicology and Safety Science, Graduate School of Pharmaceutical Sciences, Osaka University, 1-6 Yamadaoka, Suita, Osaka 565-0871, Japan
[2]Laboratory of Biopharmaceutical Research, National Institute of Biomedical Innovation, 7-6-8, Saito-Asagi, Ibaraki, Osaka 567-0085, Japan
Full list of author information is available at the end of the article

added to each gel piece, which was then incubated overnight at 37°C. We used three solutions to extract the resulting peptide mixtures from the gel pieces. First, 50 μl of 50% (*v*/*v*) ACN in 0.1% aqueous trifluoroacetic acid (TFA) was added to the gel pieces, which were then sonicated for 30 min. Next, we collected the solution and added 80% (*v*/*v*) ACN in 0.1% TFA. Finally, 100% ACN was added for the last extraction. The peptide solutions were dried and resuspended in 10 μl of 0.1% formic acid. The resulting peptide mixture was then analyzed by nano-flow liquid chromatography/tandem mass spectrometry (maXis, Bruker Daltonik GmbH, Bremen, Germany). The Mascot search engine (Matrix Science Inc., Boston, MA, USA) was initially used to query the entire theoretical tryptic peptide as well as the Swiss-Prot protein sequence database.

Measurement of hemopexin

The BALB/c mice were treated intravenously with 0.8 mg/mouse of the silica particles nSP70, nSP300, mSP1000, nSP70-C, and nSP70-N or with saline. Blood samples were collected at 2, 6, 24, 48, and 72 h after treatment. For assessment of the sensitivity of hemopexin levels to the concentration of silica particles, the BALB/c mice were treated intravenously with 0.05, 0.2, or 0.8 mg/mouse nSP70. After 24 h, blood samples were collected, and plasma was harvested by centrifuging blood at 13,800×*g* for 15 min. Plasma levels of hemopexin were measured using a commercial enzyme-linked immunosorbent assay (ELISA) kit (*Life Diagnostics*, West Chester, PA, USA), according to the manufacturer's instructions.

Plasma biochemistry

The BALB/c mice were treated intravenously with 0.8 mg/mouse nSP70 or saline. After 2, 6, 24, and 48 h, blood samples were collected, and plasma was harvested by centrifuging blood at 13,800×*g* for 15 min. Total hemoglobin and heme in the blood of the nSP70-treated mice were determined by BioAssay Systems Quanti-Chrom™ Assay Kits (BioAssay Systems, Hayward, CA, USA). Also, plasma levels of total bilirubin (TBIL) and direct bilirubin (DBIL) were measured by a biochemical auto analyzer, FUJI DRI-CHEM 7000 (Fujifilm, Tokyo, Japan), and the level of indirect bilirubin was calculated from these values.

Statistical analysis

All results are expressed as means ± standard error of the mean (SEM). Statistical comparisons between groups were performed by one-way analysis of variance (ANOVA) with the Bonferroni test.

Results

Characteristics of silica particles

Silica particles are well suited for studying the influence of nanomaterial size on biodistribution and various biological effects because they show much better dispersibility in aqueous solutions than most other nanomaterials [18]. We used three different-sized silica particles with diameters between 70 and 1,000 nm (nSP70, nSP300, and mSP1000) and nSP70 with carboxyl (nSP70-C) and amino (nSP70-N) surface functional groups. As we have described previously [9,10,13], all silica nanoparticles were confirmed by transmission electron microscopy to be smooth-surfaced spheres. The hydrodynamic diameters of nSP70, nSP300, and mSP1000 were 65, 322, and 1,140 nm, respectively, and their zeta potentials or overall surface potentials were −53, −62, and −67 mV, respectively. For nSP70-C and nSP70-N, the hydrodynamic diameters were 70 and 72 nm, respectively, and their zeta potentials were −76 and −29 mV, respectively. These results indicate that the carboxyl and amino surface modifications altered the surface charge of the particles. The size distribution spectrum of each set of silica particles showed a single peak, and the measured hydrodynamic diameter corresponded almost precisely to the primary particle size of each set of silica particles. These results indicate that the silica particles used in this study were well dispersed in solution.

2D-DIGE analysis and identification of differentially expressed proteins

To identify protein biomarkers of nanomaterials in mice, we analyzed changes in the levels of plasma proteins following treatment with nSP70 by using 2D-DIGE. Plasma proteins isolated after treatment with saline or 0.8 mg/mouse nSP70 were labeled with Cy3 and Cy5, respectively, and were used for 2D-DIGE analysis. The reason why we chose the dose of silica particles for treatment is that none of the silica particles induced any significant changes in the levels of aspartate aminotransferase (AST), alanine aminotransferase (ALT), and blood urea nitrogen and that all parameters remained within the physiological range, as we have previously reported [17]. Quantitative image analysis revealed 59 spots showing increased protein levels and 23 spots showing decreased protein levels in the plasma of nSP70-treated mice compared with controls. We selected a total of eight candidate spots showing the highest increases and decreases in protein expression levels. Then, liquid chromatography/time-of-flight/mass spectrometry (LC/TOF/MS) analysis of the spots subsequently identified seven different proteins (Figure 1). Among these proteins, haptoglobin, hemopexin, and alpha-1-acid glycoprotein 1, which are acute-phase proteins, displayed increased expression in the plasma of nSP70-treated mice. Four proteins, including inter-alpha-trypsin inhibitor, complement C4-B,

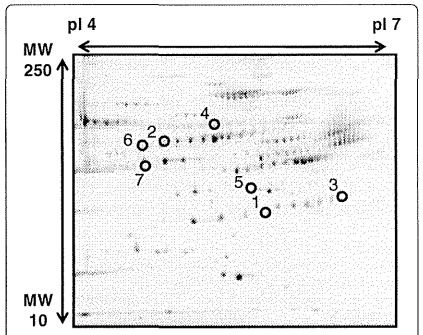

Figure 1 2D-DIGE image of fluorescent-labeled proteins. Proteins from the plasma after treatment with saline or nSP70 were labeled with Cy3 and Cy5, respectively, and used for performing 2D electrophoresis.

Cullin-4A, and serotransferrin, displayed decreased expression in the plasma of nSP70-treated mice (Table 1). These findings are consistent with the results of our previous study identifying haptoglobin, showing the highest level in this study, as a candidate biomarker using SDS-PAGE analysis. We selected a candidate biomarker from among the proteins which displayed increased expression at first. However, in the future, there is a need to identify various biomarkers by evaluating candidate proteins which displayed not only increased expression but also decreased expression to improve the accuracy for predicting the biological effects induced by nanomaterials. Here, we focused on hemopexin, which showed the second highest expression level among the identified candidate biomarkers after haptoglobin.

Plasma hemopexin levels after treatment with silica particles

Hemopexin is known as an acute-phase protein, mainly synthesized in the liver [19]. To assess the potential of hemopexin as a biomarker, we examined whether there were time-dependent changes in the plasma levels of hemopexin levels after treatment with different-sized silica particles. The BALB/c mice were treated intravenously with 0.8 mg/mouse nSP70, nSP300, or mSP1000. After 6, 24, or 72 h, we examined the plasma levels of hemopexin by ELISA. We observed no changes in the plasma levels of hemopexin in mice treated with nSP300 or mSP1000 over the time course of the experiment. However, mice treated with nSP70 showed an increase in plasma levels of hemopexin at 24 h after treatment, and the plasma level of hemopexin in nSP70-treated mice remained significantly higher than that of controls at 72 h after treatment (Figure 2A). These results indicate that the smaller the particle size, the greater the increase in plasma levels of hemopexin induced by silica particles. We then assessed the sensitivity of hemopexin induction to lower concentrations of silica particles. The BALB/c mice were treated intravenously with 0.05, 0.2, or 0.8 mg/mouse nSP70. After 24 h, we examined the plasma levels of hemopexin by ELISA and found that the plasma level of hemopexin increased in a dose-dependent manner (Figure 2B). These results indicate that the level of induction of hemopexin is dependent on the concentration of silica particles. Taken together, these findings highlight the potential of hemopexin as a valuable biomarker for analyzing the risk and toxicity of exposure to silica nanoparticles. Now, to evaluate the sensitivity of hemopexin to serve as a biomarker of a more realistic exposure, we have assessed the response of hemopexin to silica nanoparticles introduced via different routes.

Table 1 Identification of candidate proteins as biomarkers

Spot	Protein name	Accession number	MW (kD)	pI	Expression ratio (nSP70/saline) (fold)
1	Haptoglobin	[Swiss-Prot:Q61646]	38.75	5.88	375.44
2	Hemopexin	[Swiss-Prot:Q91X72]	51.34	7.92	3.25
3	Alpha-1-acid glycoprotein 1	[Swiss-Prot:Q60590]	23.89	5.58	3.05
4	Inter-alpha-trypsin inhibitor	[Swiss-Prot:Q61703]	105.93	6.82	0.40
5	Complement C4-B	[Swiss-Prot:P01029]	192.89	7.38	0.39
6	Cullin-4A	[Swiss-Prot:Q3TCH7]	87.75	8.53	0.37
7	Serotransferrin	[Swiss-Prot:Q92111]	76.72	6.94	0.30

The differentially expressed spots were identified by LC/TOF/MS. pI, isoelectric point.

Hemolytic activity of silica nanoparticles

Hemopexin is a heme-binding plasma glycoprotein that forms the second line of defense against hemoglobin-mediated oxidative damage during intravascular hemolysis [20]. Intravascular hemolysis causes the release of massive amounts of hemoglobin and heme into the plasma, where they are rapidly bound by haptoglobin and hemopexin, respectively [21]. Because nSP70 induced an increase in the plasma levels of haptoglobin and hemopexin in mice, we investigated the possibility

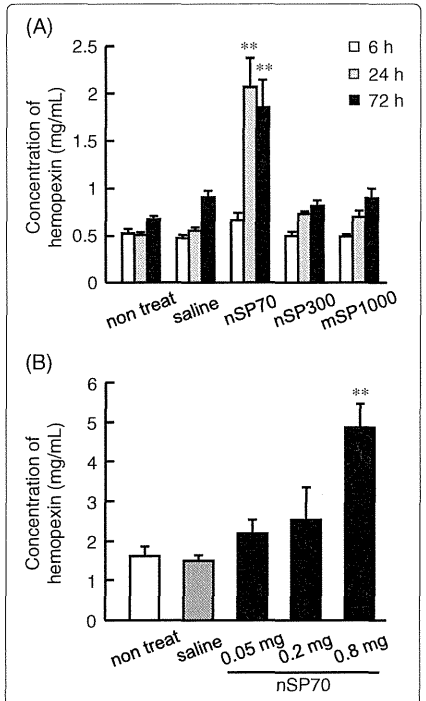

Figure 2 Plasma levels of hemopexin after treatment with silica particles. BALB/c mice were treated intravenously with 0.8 mg/mouse nSP70, nSP300, or mSP1000. (**A**) After 6, 24, and 72 h, the plasma levels of hemopexin in the mice were determined by ELISA. (**B**) BALB/c mice were treated intravenously with 0.05, 0.2, or 0.8 mg/mouse nSP70. After 24 h, blood samples were collected. The plasma levels of hemopexin in treated mice were determined by ELISA. Data are presented as mean ± SEM ($n = 5$; Double asterisks denote $P < 0.01$ versus the value for saline-treated group by ANOVA).

that silica nanoparticles could induce hemolytic activity. We assessed plasma levels of heme and hemoglobin 2, 6, 24, or 48 h after treatment of the BALB/c mice intravenously with 0.8 mg/mouse of nSP70. At this dose, nSP70 did not induce any significant increases in the plasma levels of heme (Figure 3A) or hemoglobin (Figure 3B) at all time points.

During hemolysis, hemoglobin is released into the plasma from damaged red blood cells and leads to an increase in plasma levels of indirect bilirubin [22-24]. Thus, although nSP70 did not induce a significant increase in the plasma levels of heme or hemoglobin, we investigated whether nSP70 induced hemolytic activity that resulted in an increased plasma level of indirect bilirubin. Following treatment of mice with nSP70, we measured plasma levels of TBIL and DBIL and calculated the level of indirect bilirubin from these values. We found no changes in the plasma levels of TBIL (Figure 3C), DBIL (Figure 3D), or indirect bilirubin (Figure 3E) over the time course of the experiment. Taken together, these results clearly show that nSP70 does not induce hemolytic activity in mice under these conditions.

Surface modification of nSP70

Previously, we demonstrated that surface properties of silica nanoparticles play an important role in determining their safety [11,13]. For instance, our group showed that surface modification of nSP70 with amine or carboxyl groups altered the intracellular distribution of the nanoparticles, had an effect on cell proliferation [11], and suppressed toxic biological effects of silica particles such as inflammatory responses. To assess whether hemopexin could predict the strength of toxicity induced by silica nanoparticles, we examined the plasma levels of hemopexin in the mice after administration of nSP70 with amino or carboxyl group surface modifications. The BALB/c mice were treated intravenously with 0.8 mg/mouse of nSP70, nSP70-C, or nSP70-N. After 2, 6, 24, or 48 h, we examined the plasma levels of hemopexin by ELISA. The mice treated with nSP70, nSP70-C, and nSP70-N did not show any elevated level of hemopexin at 2 or 6 h. At 24 h, the plasma level of hemopexin in mice treated with nSP70-N was significantly lower than that in mice treated with unmodified nSP70. On the other hand, the plasma level of hemopexin in mice treated with nSP70-C was similar to that in nSP70-treated mice and significantly higher than that in saline-treated mice (Figure 4A). At the same time, the plasma levels of haptoglobin (Figure 4B) and SAA (Figure 4C) in mice treated with nSP70-C were significantly lower than those in nSP70-treated mice, which is consistent with our previously reported results [17]. These results indicate that there are differences in the mechanisms underlying the production of hemopexin and other acute-phase proteins induced by nSP70-C.

Discussion

By using biomarkers, we are able to predict not only the present disease and clinical condition, but also the risk of acquiring disease in the future. Therefore, it is necessary to progress studies of biomarkers for nanomaterials because very little information is available on the biological effects of nanomaterials. Here, we used 2D-DIGE analysis to perform a comprehensive screen of plasma proteins to identify protein biomarkers of nanomaterials. We identified hemopexin (Table 1) as a useful biomarker for analyzing the biological responses associated with exposure to silica nanoparticles. Because 2D-DIGE is a proteomic method, this approach has potential to uncover the as yet unknown biological effects of nanomaterials.

On the other hand, an inherent disadvantage of 2D electrophoresis is the poor resolution of hydrophobic proteins [25,26]. Hence, it is likely that integral membrane proteins are strongly underrepresented. Isobaric tags for relative and absolute quantification or iTRAQ is a comprehensive gel-free quantitative proteomic method based on mass spectrometry [27,28]. This approach can be used to generate proteomic profiles that reflect the pathological state of organs and aid in the early detection of diseases [29,30]. We envisage that a combination of comprehensive proteomic methods would help to identify potential toxicities of nanomaterials during their development and contribute to the establishment of strategies to ensure their safety.

Silica materials with amorphous particle morphology are known to cause the hemolysis of mammalian red blood cells [31,32]. For this reason, we investigated the possibility that silica nanoparticles could induce hemolytic activity. While the exact mechanism is still

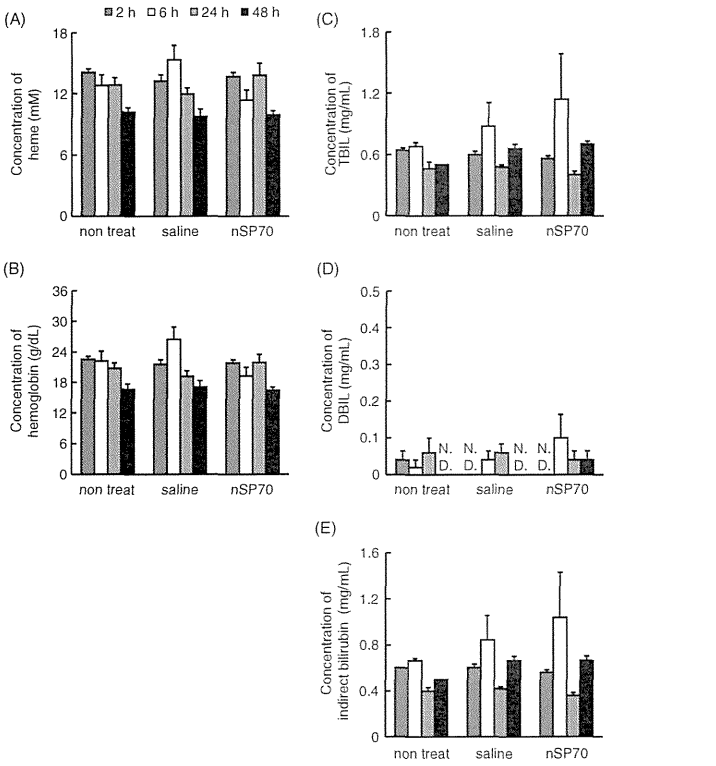

Figure 3 Hemolytic activity of silica nanoparticles. BALB/c mice were treated intravenously with 0.8 mg/mouse nSP70. After 2, 6, 24, and 48 h, we examined the level of (**A**) total heme and (**B**) hemoglobin in the blood of treated mice. The levels of (**C**) TBIL and (**D**) DBIL were measured, and (**E**) the level of indirect bilirubin was calculated from these values.

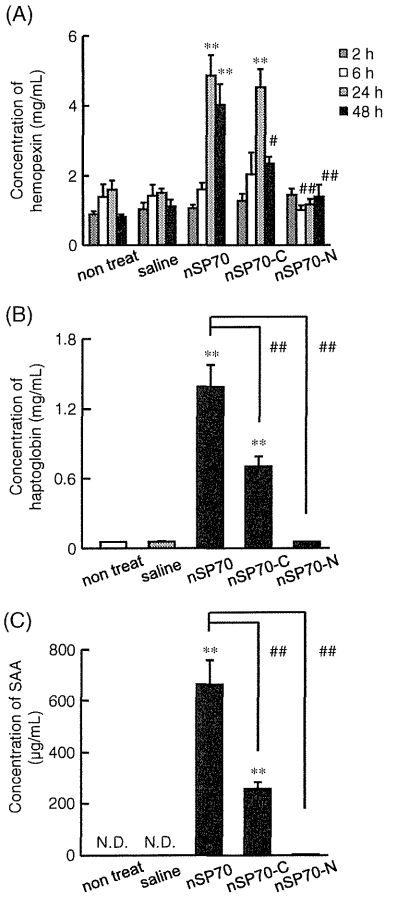

Figure 4 Responses of hemopexin by the exposure to surface modified nSP70. BALB/c mice were treated intravenously with nSP70 modified with amino (nSP70-N) or carboxyl (nSP70-C) groups at 0.8 mg/mouse. (**A**) After 2, 6, 24, and 48 h, the levels of hemopexin in the plasma of treated mice were examined by ELISA. The plasma levels of (**B**) haptoglobin and (**C**) SAA were determined by ELISA after 24 h. Data are presented as mean ± SEM. ($n = 5$; Double asterisks denote $P < 0.01$ versus the value for the saline-treated group by ANOVA, single hash denotes $P < 0.05$, and double hash denote $P < 0.01$ versus the value for the nSP70-treated group by ANOVA).

under investigation, most reports agree that the hemolytic activity of silica particles is related to surface characteristics such as area and curvature [33-35]. However, we found that nSP70 at 0.8 mg/mouse does not induce hemolytic activity through elevation of haptoglobin and hemopexin (Figure 3). We are continuing investigations to understand the biological mechanisms associated with the elevation of hemopexin after exposure to silica nanoparticles.

We then examined the effects of surface modification of silica nanoparticles on the production of hemopexin. Compared to controls, hemopexin was not induced by nSP70-N but was induced to a significantly higher level by nSP70-C, which was a similar level to that induced by unmodified nSP70 (Figure 4A). On the other hand, the plasma levels of haptoglobin (Figure 4B) and SAA (Figure 4C) in mice treated with nSP70-C were significantly lower than those in mice treated with nSP70, as reported previously [17]. These results suggest that the production of acute-phase proteins depends on the characteristics of the nanomaterials and that nSP70-C induces some biological effects associated with the elevation of hemopexin. Increased hemopexin levels have been found in patients with diabetes mellitus and are associated with some malignancies, such as malignant melanoma and breast cancer [20,36,37]. Elevated hemopexin levels have also been found in inflammatory psychiatric disorders, such as major depression, schizophrenia, and mania [38]. Taken together, these findings suggest that hemopexin might be associated with these diseases so it is possible that the induced elevation of hemopexin by both nSP70 and nSP70-C is related to the induction of inflammatory responses. Therefore, we are currently analyzing not only the mechanisms underlying the differences in production of hemopexin, haptoglobin, and SAA induced by nSP70-C and nSP70, but also the relationship. It could be speculated that there are differences between the fates of the injected nSP70 and nSP70-C. Therefore, there is a need to evaluate the distribution or accumulation of the injected nanoparticles in the liver where acute-phase proteins are known to be produced. An understanding of these mechanisms will advance the use of biomarkers for different purposes and improve the predictive value of these biomarkers.

Hemopexin is one of the acute-phase proteins released from the liver, and its production is known to be regulated by cytokines. For instance, interleukin (IL)-6 and IL-22 induce the hepatic production of circulating SAA [39,40]. Furthermore, it is conceivable that instead of inflammatory cytokines, small silica particles act directly on the liver to induce the release of acute-phase proteins. However, nSP70, at this dose, did not induce any significant elevation of liver injury or dysfunction

markers, such as ALT or AST. Therefore, it is unclear why nanomaterials induce the production of acute-phase proteins. We are currently analyzing the detailed mechanism by which silica particles induce acute-phase proteins.

Conclusions

We demonstrated that 2D-DIGE analysis is a useful approach for identifying novel biomarkers of nanomaterials. Using this approach, we identified hemopexin as a useful biomarker and showed here that hemopexin can act as a useful biomarker for analyzing the biological responses associated with exposure to silica nanoparticles. We believe that this study will contribute to the development of biomarkers for ensuring the safety of silica nanoparticles.

Abbreviations

2D: Two-dimensional; 2D-DIGE: Two-dimensional differential in gel electrophoresis; ACN: Acetonitrile; ALT: Alanine amino transferase; AST: Aspartate amino transferase; DBIL: Direct bilirubin; ELISA: Enzyme-linked immunosorbent assay; IL: Interleukin; IPG: Immobilized pH gradient; iTRAQ: Isobaric tags for relative and absolute quantification; LC/TOF/MS: Liquid chromatography/time-of-flight/mass spectrometry; SAA: Serum amyloid A; SDS-PAGE: Sodium dodecyl sulfate-polyacrylamide gel electrophoresis; TBIL: Total bilirubin; TFA: Trifluoroacetic acid.

Competing interests

The authors declare that they have no competing interests.

Authors' contributions

KH and YY designed the study. KH, KY, YM, HP, TO, TN, and AK performed the experiments. KH and YY collected and analyzed the data. KH and YY wrote the manuscript. KN, YA, HK, ST, HN, and TY gave technical support and conceptual advice. YT supervised all of the projects. All authors discussed the results and commented on the manuscript. All authors read and approved the final manuscript.

Acknowledgments

This study was supported in part by Grants-in-Aid for Scientific Research from the Ministry of Education, Culture, Sports, Science and Technology of Japan and from the Japan Society for the Promotion of Science (JSPS). This study was also supported in part by the following: Health Labour Sciences Research Grants from the Ministry of Health, Labor and Welfare of Japan; Health Sciences Research Grants for Research on Publicly Essential Drugs and Medical Devices from the Japan Health Sciences Foundation; the Global Environment Research Fund from the Minister of the Environment; the Knowledge Cluster Initiative; The Nagai Foundation Tokyo; the Cosmetology Research Foundation; the Smoking Research Foundation; the Research Foundation for Pharmaceutical Sciences; and The Japan Food Chemical Research Foundation.

Author details

[1]Laboratory of Toxicology and Safety Science, Graduate School of Pharmaceutical Sciences, Osaka University, 1-6 Yamadaoka, Suita, Osaka 565-0871, Japan. [2]Laboratory of Biopharmaceutical Research, National Institute of Biomedical Innovation, 7-6-8, Saito-Asagi, Ibaraki, Osaka 567-0085, Japan. [3]Cancer Biology Research Center, Sanford Research/USD, 2301 E. 60th Street N, Sioux Falls, SD 57104, USA. [4]The Center for Advanced Medical Engineering and Informatics, Osaka University, 1-6, Yamadaoka, Suita, Osaka 565-0871, Japan. [5]Division of Foods, National Institute of Health Sciences, 1-18-1 Kamiyoga, Setagaya-ku, Tokyo 158-8501, Japan.

Received: 16 July 2012 Accepted: 21 September 2012
Published: 8 October 2012

References

1. Augustin MA, Sanguansri P: **Nanostructured materials in the food industry.** *Adv Food Nutr Res* 2009, **58**:183-213.
2. Bowman DM, van Calster G, Friedrichs S: **Nanomaterials and regulation of cosmetics.** *Nat Nanotechnol* 2010, **5**:92.
3. Kagan VE, Bayir H, Shvedova AA: **Nanomedicine and nanotoxicology: two sides of the same coin.** *Nanomedicine* 2005, **1**:313-316.
4. Nel A, Xia T, Madler L, Li N: **Toxic potential of materials at the nanolevel.** *Science* 2006, **311**:622-627.
5. Merget R, Bauer T, Kupper HU, Philippou S, Bauer HD, Breitstadt R, Bruening T: **Health hazards due to the inhalation of amorphous silica.** *Arch Toxicol* 2002, **75**:625-634.
6. Knopp D, Tang D, Niessner R: **Review: bioanalytical applications of biomolecule-functionalized nanometer-sized doped silica particles.** *Anal Chim Acta* 2009, **647**:14-30.
7. Napierska D, Thomassen LC, Lison D, Martens JA, Hoet PH: **The nanosilica hazard: another variable entity.** *Part Fibre Toxicol* 2010, **7**:39.
8. Lankoff A, Arabski M, Wegierek Ciuk A, Kruszewski M, Lisowska H, Banasik-Nowak A, Rozga-Wijas K, Wojewodzka M, Slomkowski S: **Effect of surface modification of silica nanoparticles on toxicity and cellular uptake by human peripheral blood lymphocytes in vitro.** *Nanotoxicology* 2012. doi:10.3109/17435390.2011.649796.
9. Nabeshi H, Yoshikawa T, Matsuyama K, Nakazato Y, Matsuo K, Arimori A, Isobe M, Tochigi S, Kondoh S, Hirai T, Akase T, Yamashita T, Yamashita K, Yoshida T, Nagano K, Abe Y, Yoshioka Y, Kamada H, Imazawa T, Itoh N, Nakagawa S, Mayumi T, Tsunoda S, Tsutsumi Y: **Systemic distribution, nuclear entry and cytotoxicity of amorphous nanosilica following topical application.** *Biomaterials* 2011, **32**:2713-2724.
10. Nabeshi H, Yoshikawa T, Matsuyama K, Nakazato Y, Tochigi S, Kondoh S, Hirai T, Akase T, Nagano K, Abe Y, Yoshioka Y, Kamada H, Itoh N, Tsunoda S, Tsutsumi Y: **Amorphous nanosilica induce endocytosis-dependent ROS generation and DNA damage in human keratinocytes.** *Part Fibre Toxicol* 2011, **8**:1.
11. Nabeshi H, Yoshikawa T, Arimori A, Yoshida T, Tochigi S, Hirai T, Akase T, Nagano K, Abe Y, Kamada H, Tsunoda S, Itoh N, Yoshioka Y, Tsutsumi Y: **Effect of surface properties of silica nanoparticles on their cytotoxicity and cellular distribution in murine macrophages.** *Nanoscale Res Lett* 2011, **6**:93.
12. Nabeshi H, Yoshikawa T, Matsuyama K, Nakazato Y, Arimori A, Isobe M, Tochigi S, Kondoh S, Hirai T, Akase T, Yamashita T, Yamashita K, Yoshida T, Nagano K, Abe Y, Yoshioka Y, Kamada H, Imazawa T, Itoh N, Kondoh M, Yagi K, Mayumi T, Tsunoda S, Tsutsumi Y: **Amorphous nanosilicas induce consumptive coagulopathy after systemic exposure.** *Nanotechnology* 2012, **23**:045101.
13. Yamashita K, Yoshioka Y, Higashisaka K, Mimura K, Morishita Y, Nozaki M, Yoshida T, Ogura T, Nabeshi H, Nagano K, Abe Y, Kamada H, Monobe Y, Imazawa T, Aoshima H, Shishido K, Kawai Y, Mayumi T, Tsunoda S, Itoh N, Yoshikawa T, Yanagihara I, Saito S, Tsutsumi Y: **Silica and titanium dioxide nanoparticles cause pregnancy complications in mice.** *Nat Nanotechnol* 2011, **6**:321-328.
14. Casado B, Iadarola P, Luisetti M, Kussmann M: **Proteomics-based diagnosis of chronic obstructive pulmonary disease: the hunt for new markers.** *Expert Rev Proteomics* 2008, **5**:693-704.
15. Ferte C, Andre F, Soria JC: **Molecular circuits of solid tumors: prognostic and predictive tools for bedside use.** *Nat Rev Clin Oncol* 2010, **7**:367-380.
16. Li N, Nel AE: **Feasibility of biomarker studies for engineered nanoparticles: what can be learned from air pollution research.** *J Occup Environ Med* 2011, **53**:S74-79.
17. Higashisaka K, Yoshioka Y, Yamashita K, Morishita Y, Fujimura M, Nabeshi H, Nagano K, Abe Y, Kamada H, Tsunoda S, Yoshikawa T, Itoh N, Tsutsumi Y: **Acute phase proteins as biomarkers for predicting the exposure and toxicity of nanomaterials.** *Biomaterials* 2011, **32**:3-9.
18. He X, Nie H, Wang K, Tan W, Wu X, Zhang P: **In vivo study of biodistribution and urinary excretion of surface-modified silica nanoparticles.** *Anal Chem* 2008, **80**:9597-9603.
19. Tolosano E, Altruda F: **Hemopexin: structure, function, and regulation.** *DNA Cell Biol* 2002, **21**:297-306.
20. Delanghe JR, Langlois MR: **Hemopexin: a review of biological aspects and the role in laboratory medicine.** *Clin Chim Acta* 2001, **312**:13-23.